Development of an Advanced Radioxenon Detector for Nuclear Explosion Monitoring

by

Ciara B. Sivels

A dissertation submitted in partial fulfillment
of the requirements for the degree of
Doctor of Philosophy
(Nuclear Engineering and Radiological Sciences)
in the University of Michigan
2018

Doctoral Committee:

Dr. Justin McIntyre, Co-Chair
Professor Sara Pozzi, Co-Chair
Dr. Shaun Clarke
Professor John Lee
Professor James Morrow

Ciara B. Sivels

csivels@umich.edu

ORCID iD: 0000-0002-2250-8898

Dedication

For my family

"Let your light so shine before men, that they may see your good works, and glorify your Father which is in heaven."
- Matthew 5:16

Acknowledgements

I would like to thank Prof. Sara Pozzi and Dr. Shaun Clarke for welcoming me into the group and allowing me to work on radioxenon projects while supporting me throughout my graduate career and for giving me an opportunity to grow and contribute to DNNG. I would like to thank Dr. Justin McIntyre for supporting me throughout my graduate career through the ups and downs, for being an amazing mentor, for joining me in the lab often, and for helping me grow my technical capabilities while keeping it real and entertaining. I would like to thank Prof. Lee and Prof. Morrow for their dialogue and help with the thesis. I would like to thank Dr. Amanda Prinke for her support throughout my graduate career, for also being a mentor and an ear to vent and learn from, and for helping wrap up my final experiments. Thank you to the members of DNNG that helped me throughout the years and helped me pass the time, especially Cameron, Tony, and Charlie. I would especially like to thank Prof. John Foster for all his support throughout my time at Michigan, it was invaluable. I would also like to thank Prof. Gilgenbach for his support and flexibility with NERS GSC and the Women in NERS group, as well as the many outreach efforts.

I would like to thank all of my family, especially my mom, Sandra, dad, Modestine I, brother, Modestine II, and sister, Neferteria, for supporting me throughout this journey. To my friends and family back home, especially Kornisha, Carrie, Chelsey, Ciara, Foreman, Rumeal, Terrance, Kelsey, Shanta, Jeffery, Alexis, and Jasmin, thank you for always being there for me and bringing me back to earth. To Nanny, Dante, and Aunt Peaches, I wish that you were here with me, but I know you are smiling down from above. I would also like to thank Second Baptist Church of Ann Arbor and Mr. and Mrs. Byron and Marnise Roberts for allowing me to be a part of their family.

Thank you to my friends: Autumn and Aeriel, for being true friends and always being there for me, I can't imagine this journey without you two, Oleta for your friendship, realness, and carefree spirit, Lauren for your friendship, honesty, laughter, and being an amazing roommate, Yasmine for your friendship, kindness, help with integrating to UM and being my longest roommate ever, Kendra for your friendship, laughter, and great stories, Kyle and Sammy for your friendship, laughter, and fun throughout this journey, Crystal for your friendship, laughter, craziness, and being along with me on this journey in NERS and Val and Sam, we have shared a lot of experiences and I am grateful to have had you along for the ride, and Corine for your friendship and openness. To my MIT friends, B Jones now Matthews I am so thankful for your friendship and showing me what inspiration looks like, Merricka for your friendship and continued support over the years, and Mareena for your friendship and being a fireball of support.

This work was funded in-part by the Consortium for Verification Technology under Department 305

of Energy National Nuclear Security Administration award number DE-NA0002534.

This work was funded in-part by PNNL contract number 315246, along with numerous internships and experimental campaigns.

Finally, I can't name everyone so thank you to any and everyone I've had contact with over these last five and a half years for your words of encouragement, love, and support and I hope you enjoy this thesis.

Table of Contents

List of Figures

List of Tables

List of Appendices

List of Abbreviations

ACM Anticoincidence Method

CE Conversion Electron

CTBT Comprehensive Nuclear-Test-Ban Treaty

CTBTO Preparatory Commission for the Comprehensive Nuclear-Test-Ban Treaty Organization

DPRK Democratic People's Republic of Korea

HPGe High-Purity Germanium

IAEA International Atomic Energy Agency

IDC International Data Center

IMS International Monitoring System

LTBT Limited Test Ban Treaty

MDC Minimum detectable concentration

MIPF Medical Isotope Production Facility

MIRC Multi-Isotopic Ratio Correlation

NNWS Non-Nuclear Weapons States

NPT Treaty on the Non-Proliferation of Nuclear Weapons

NWS Nuclear Weapons States

OSI On-Site Inspection

PMT Photomultiplier Tube

PNET Peaceful Nuclear Explosions Treaty

PNNL Pacific Northwest National Laboratory

PSD Pulse Shape Discrimination

PTBT Partial Test Ban Treaty

ROI Region of Interest

TTBT Threshold Test Ban Treaty

Abstract

The Comprehensive Nuclear-Test-Ban Treaty was opened for signature in 1996 and seeks to ban nuclear weapons testing worldwide. The International Monitoring System (IMS) was established to verify treaty compliance, and consists of four technologies: seismic, infrasound, hydroacoustic, and radionuclide. The radionuclide component of the IMS conducts atmospheric monitoring to identify radioactive particles and gases associated with nuclear testing, such as radioxenon. As a noble gas, the radioxenon produced in an underground nuclear explosion can be released into the atmosphere, for subsequent detection by the IMS. Radioxenon is also produced by fission-based civilian processes, such as nuclear reactors and medical isotope production facilities, requiring discrimination between these sources. The focus of this work is to improve the resolution and sensitivity of radioxenon monitoring systems.

Radioxenon is measured using beta-gamma coincidence techniques, typically with scintillating plastic and NaI(Tl) detectors; however, the poor energy resolution of the plastic results in isotopic interference, complicating the analysis. Additionally, radon emits decay energies that interfere with those from radioxenon, requiring complex gas-processing systems to filter it from the sample. Furthermore, radioxenon diffuses into the plastic detectors, which increases the background of subsequent measurements; this phenomenon is known as the memory effect. To mitigate these issues, this thesis demonstrated 1) an anticoincidence analysis method to better identify metastable isotopes, 2) a validated MCNPX-PoliMi simulation tool to analyze new detector systems and produce training spectra for analysis testing, and 3) a prototype radioxenon detector system based on stilbene.

Stilbene cell prototypes have been developed, tested, and compared with a traditional plastic scintillator cell. The results show that the stilbene cell has similar response to the plastic cell with an improved energy resolution, full-width at half-maximum decreased by 2.2 keV at 129 keV. The stilbene cell is capable of pulse shape discrimination allowing for radon mitigation through alpha identification. The analysis presented reduced the minimum detectable concentration of Xe-135 by 1% and could be used for environmental monitoring. The stilbene cell was shown to have 0.043% residual activity compared to 4.5% residual activity for the plastic cell, demonstrating significantly improved memory effect. The results presented in the thesis allow for better identification of metastable isotopes, improved simulation techniques, and improved detection sensitivity which could lead to improved source discrimination strengthening the Comprehensive Nuclear-Test-Ban Treaty verification regime.

Chapter 1

Introduction

Radioxenon monitoring is essential in the detection of nuclear explosions. Since the Cold War, various forms of nuclear explosion monitoring have been developed. In recent years, focus has been placed on improving detection sensitivities for low-yield nuclear explosions. In particular, distinguishing background sources from nuclear explosion signatures in the atmosphere has become more challenging due to increased interference and better containment. As a result, the detection and identification of the metastable isotopes is vital to source characterization. This push for lower detection sensitivities has resulted in numerous detector developments, along with alternative analysis techniques and simulation tools.

1.1 Early History of Nuclear Explosion Monitoring

Over 2,000 nuclear tests were carried out all over the world between 1945-2015 [1]. Early testing in the 1940s led to the use of nuclear weapons by the United States on Japan during World War II, and resulted in decades of nuclear weapons development and testing during the Cold War. As nuclear weapons programs were developing, nations needed ways to monitor and verify nuclear weapons programs.

The first known instances of nuclear explosion monitoring occurred in the mid-1940s. One example is the US reconnaissance flights that were occurring over German nuclear sites [2]. These airplanes used air sampling equipment developed to detect xenon, a signature of nuclear activity and possibly

weapons development [2]. The samples were measured in ground-based laboratories and analyzed for nuclear weapons signatures. In addition to reconnaissance flights, other methods of identifying nuclear testing became apparent with the first nuclear weapons test, Trinity, conducted by the US in 1945. The nuclear test was detected at long ranges by GM-tubes [3] and seismic signatures [2]. As a result of these detections, a project was developed to test radioactivity in the air after US nuclear weapons tests. From June 24 to August 21, 1946, 357 flights occurred around nuclear explosion test sites to sample radioactivity in the air. The results showed that radionuclides can be detected from the fallout of these explosions, sometimes at long-ranges [2]. However, the difficulty of distinguishing radionuclides from explosions versus civilian sources, such as reactors, was a limitation of these techniques. .

The period of nuclear weapons testing in the 1940s and 50s, sparked the need for international agreements to prevent the spread of nuclear weapons and their effects on the environment. The public outcry from the US Castle test series, which contaminated the Marshall Islands and the Japanese fishing vessel, Lucky Dragon, led to the first suggestion of a nuclear testing ban by India in 1954 [4, 5]. In 1957, German scientists led by Otto Han pledged to not participate in nuclear weapons development and thousands of scientists signed a petition calling for a ban on testing led by Linus Pauling [4]. These activist movements led to a moratorium on nuclear testing between the Soviet Union and the United States that lasted from 1958 to 1961 [6]. During this period, the United States, Great Britain, and the Soviet Union negotiated test bans, but no agreement was reached due to disagreements on verification measures, specifically on-site inspection [7]. Parallel to the test ban negotiations, a conference of experts, proposed by President Eisenhower, met from April to August in 1958, and released a report suggesting that a comprehensive nuclear test ban could be verified through a network of 160 monitoring stations [5].

In 1961, the Soviet Union resumed atmospheric testing in response to France's nuclear weapons program development [5]. As a result, the US and Great Britain proposed a ban on atmospheric testing, which the Soviet Union rejected, prompting the US to resume atmospheric testing in April

1962 [5]. However, the Cuban Missile Crisis in October 1962, seen as running an unacceptably high risk of nuclear war, sparked new discussions on a test ban [7]. Because verification measures were still an issue, the new discussions focused on a limited scope test ban. After only 12 days of negotiations, the Limited Test Ban Treaty (LTBT), also known as the Partial Test Ban Treaty (PTBT) [8], entered into force in 1963, banning tests in the atmosphere, outer space, and underwater. This resulted in the development of the Air Force Technical Applications Center (AFTAC) by the US Air Force to monitor treaty compliance and advance long-range detection capabilities [9]. The treaty did not directly ban underground nuclear testing, but prohibited tests in environments that would allow for fallout to spread beyond the borders of the country conducting the test [10]. A major limitation of the LTBT was the lack of shared international verification measures; however, it was a major step towards nuclear disarmament.

The growth of nuclear weapons stockpiles and the risk of proliferation eventually led to the Non-Proliferation of Nuclear Weapons Treaty (NPT), which entered into force in 1970 and was extended indefinitely in 1995 [11]. The NPT seeks to prevent the spread of nuclear weapons with the goal of complete disarmament while promoting the peaceful uses of nuclear energy [11]. To this end, the treaty established the designation of nuclear weapon states (NWS) as the countries that have tested nuclear weapons before 1967 (China, France, Russia, the United Kingdom, and the United States, also known as the P5) and prohibited them from transferring technology or weapons to non-nuclear weapon states (NNWS). The International Atomic Energy Agency (IAEA) was tasked with establishing and maintaining safeguard measures; however, the treaty lacked any ban on nuclear testing. The treaty did call for the conclusion of a comprehensive ban on nuclear testing by 1996 in its preamble [5]. Even with the treaties indefinite extension, many NNWS felt that the NPT was inadequate because it had no definite timeline for NWS to get rid of their stockpiles [12]. These grievances were met with promises to discuss a comprehensive test ban treaty and fissile material cut-off treaty.

Between the 1970s and 90s, many clandestine nuclear programs were developed by parties to

the NPT, most notably Iraq and Iran, resulting in advanced verification methods known as the Model Additional Protocol [12]. Other countries developed nuclear programs such as Libya, South Africa, Pakistan, and North Korea, and many of these programs were developed using the peaceful technology acquired through the NPT. Additionally, India conducted its first nuclear weapons test in 1974, using technology received for peaceful purposes through a US-Canada agreement [1]. The nuclear testing by India, in addition to the other illicit programs, prompted the development of the Nuclear Suppliers Group (NSG) to further restrict trade of nuclear technology and materials to only countries with IAEA safeguards in place [13]. Thus, the NPT has done a good job of limiting the proliferation of nuclear weapons, but it has not completely eliminated the development of nuclear weapons programs. Additionally, during this time many protests around the country pushed test ban discussions. Greenpeace activists traveled to nuclear test sites preventing testing from occurring and protests in the US forced politicians to discuss ending the nuclear arms race and testing [4].

Because the NPT lacked no bans on nuclear testing, and the PTBT contained no verification measures, negotiations in the following years focused on these tasks. In 1974, the United States and the Soviet Union signed the Treaty on the Limitation of Underground Nuclear Weapon Tests also known as the Threshold Test Ban Treaty (TTBT). This treaty established a nuclear threshold of 150 kiloton yields for underground nuclear explosions at test sites specified in the treaty [14]. The treaty also obligated the parties to make progress towards a comprehensive test ban and established a verification method [14]. To this end, the countries agreed to exchange geographic and geological information for the nuclear test sites along with data from two nuclear weapons tests for calibration purposes [14]. Additionally, the Treaty on the Underground Nuclear Explosions for Peaceful Purposes, also known as the Peaceful Nuclear Explosions Treaty (PNET), was negotiated to ensure that nuclear testing at sites outside of those specified in the TTBT were under verification measures [15]. In 1988, the Soviet Union and the United States conducted the Joint Verification Experiment to build confidence in the verification measures of the TTBT and PNET [1]. With the success of this experiment, the treaties went into force in 1990 when the two countries exchanged ratification

instruments [15]. The TTBT and PNET were the first steps to establish a comprehensive nuclear test ban. Figure 1.1 shows a timeline of nuclear tests by country from 1945-2017 [1]. The previously mentioned nuclear testing moratorium is shown by the lack of testing between 1959-1960. The effect of the LTBT is shown with the shift of nuclear testing to underground testing in 1964. The lack of testing after 1996 is due to the opening of the CTBT, discussed in the following section.

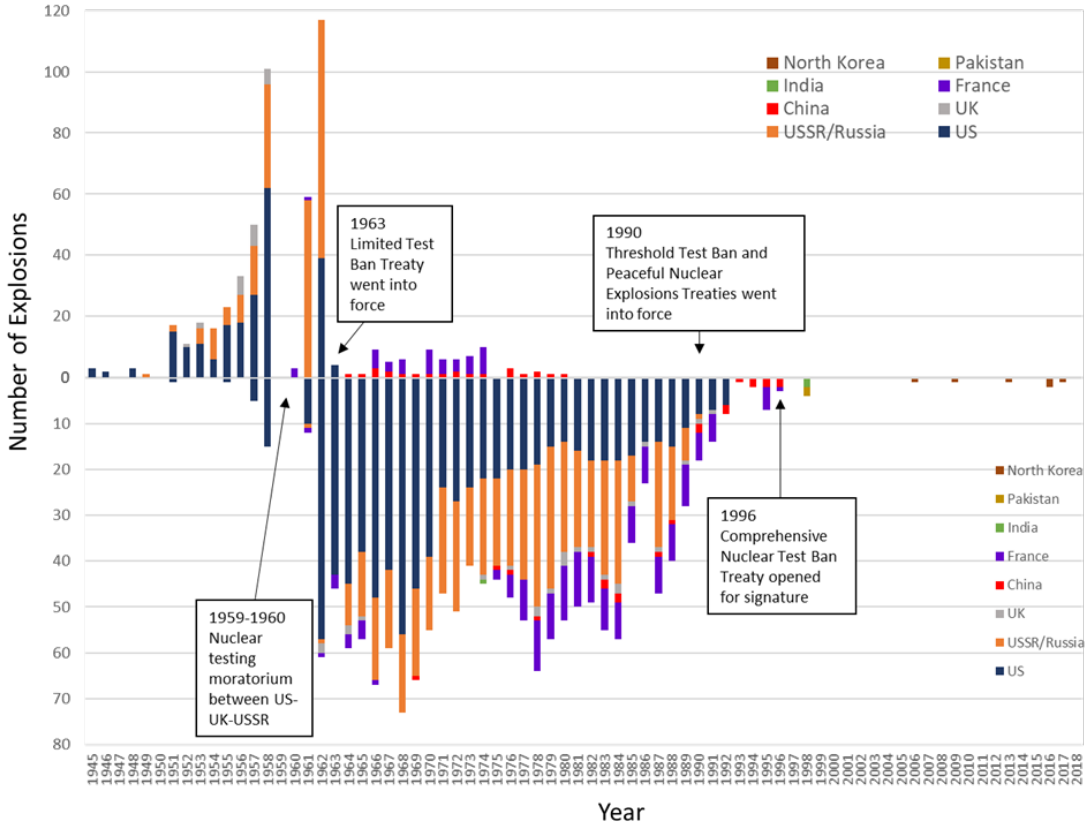

Figure 1.1: Timeline of worldwide nuclear testing [1].

1.2 The Comprehensive Nuclear-Test-Ban Treaty

1.2.1 Origins

In 1991, the Soviet Union declared a moratorium on nuclear testing, causing other countries to follow suit opening the door for negotiations on a comprehensive test ban treaty. Discussion on the yield limits were met with public protests calling for a zero-yield ban [5]. The Group of Scientific Experts (GSE) played a major role in the formal negotiations at the Conference on Disarmament,

since research into the verification methods had been ongoing since the 1970s [1]. A technical report was released by former weapons scientists stating that there was no need for low-yield nuclear tests [5]. In 1996, Nuclear-Weapon-Free-Zones were also established in Africa and the South Pacific to help with the nuclear nonproliferation and disarmament efforts [5, 16]. In 1996, after a series of negotiations [17], the Comprehensive Nuclear-Test-Ban Treaty (CTBT) was opened for signature. As stated in the treaty, to move toward nuclear disarmament, the testing and development of nuclear weapons must end [18]. Therefore, the CTBT bans all nuclear testing and explosions on Earth [1].

The treaty was voted against by India because it did not contain disarmament provisions [4]. This led to nuclear weapons testing by India in May 1998, followed by Pakistan nuclear weapons testing two weeks later. The protests that followed these demonstrations increased support for the CTBT. In the following years, North Korea also conducted nuclear weapons tests. Therefore, in addition to the five NWS, four countries emerged as nuclear weapons possessors during this time: India, Pakistan, North Korea, and Israel (not declared). The development of these programs illustrated the need for a global monitoring mechanism to help stop the development of new weapons programs.

1.2.2 The Preparatory Commission for the Comprehensive Nuclear-Test-Ban Treaty Organization

The Preparatory Commission for the Comprehensive Nuclear-Test-Ban Treaty Organization (CTBTO) was established as the verification regime and consists of an International Monitoring System (IMS), consultation and clarification, On-Site Inspection (OSI), and confidence-building measures.

The IMS is a network of over 300 monitoring stations and laboratories established all over the world to monitor the atmosphere, underground, and underwater for any signs of nuclear explosions of at least 1 kiloton yield. The monitoring stations are automated, and operate constantly. The four main technologies employed by the IMS are: seismic, hydroacoustic, infrasound, and radionuclide. Figure 1.2 shows the locations of the monitoring stations.

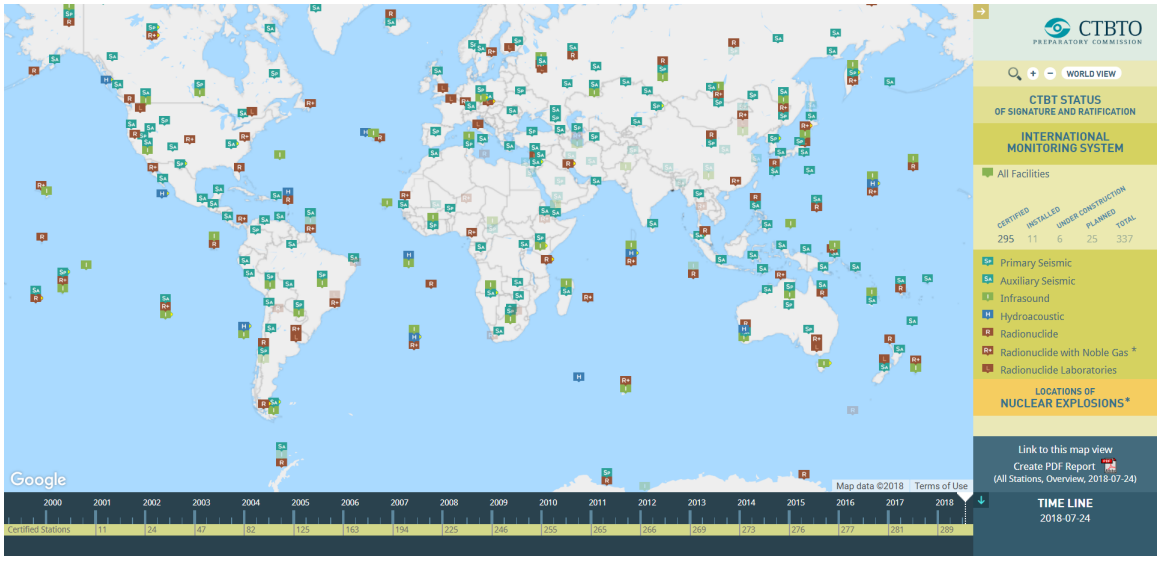

Figure 1.2: International Monitoring System station locations [1].

Of the 300+ stations in the IMS, there are 170 seismic stations [1]. The purpose of these stations is to detect and locate nuclear explosions. The major task for seismic monitoring is to distinguish earthquakes and other man-made seismic events from nuclear explosions. Seismic monitoring is done by measuring the waves generated by these events with seismometers, which convert ground motion into electrical voltage [1]. A benefit of this technology is that it produces rapid results, because seismic waves can be registered on stations within minutes of the event.

There are 11 hydroacoustic stations in the IMS [1]. The purpose of these stations is to detect and locate underwater nuclear explosions. As with seismic monitoring, the major task for hydroacoustic monitoring is to distinguish human activities from nuclear explosions. Hydroacoustic monitoring is done by measuring sound waves that can change the water pressure [1]. Because this technique can detect small signals at long distances, the number of stations required to monitor the world are low compared to the number of seismic stations.

There are 60 infrasound stations in the IMS [1]. The purpose of these stations is to detect infrasonic waves due to atmospheric nuclear explosions. As with the previously mentioned monitoring stations, the major task for infrasound monitoring is to distinguish natural sources such as exploding

volcanoes and storms and man-made sources such as mining from nuclear explosions [1]. Infrasound monitoring is done by measuring low frequency acoustic waves that cause changes in the atmospheric pressure [1].

The three previously mentioned technologies are waveform technologies. The key technology for positively identifying the nuclear nature of explosions is radionuclide, because it is the only technology capable of identifying the radioactive fission signatures that are generated in a nuclear explosion. There are 80 radionuclide stations in the IMS. As discussed in Section 1.1, the development of radioactive fallout monitoring has been ongoing since the 1940s. Radionuclide monitoring is primarily done through two methods: measuring the radioactivity of dust samples and sampling air for radioactive noble gas signatures [2].

Building off of this knowledge, particulate sampling stations in the IMS use filters to collect dust that could be due to above ground tests or released particulates from nuclear explosions. These filters are then measured by radiation detectors to identify fission-product isotopes. Noble gas detection is especially important in the case of well contained low-yield underground nuclear explosions, because noble gases are able to seep out through cracks in the rock. Within the 80 radionuclide stations in the IMS, 40 of the stations are equipped with noble gas detection systems [1]. Of the noble gases produced in nuclear explosions, radioxenon has the highest cumulative fission yield, has detectable emission energies, and reasonable half-lives for detection. A complement to radionuclide monitoring is atmospheric transport modeling (ATM), which uses the measured radionuclide data along with metrological information to localize the source of radioxenon [19–29]. Therefore, waveform technologies give information about the location and time of the event, radionuclide measurements have the ability to characterize an event as a nuclear, and ATM further helps identify the location of the source.

The International Data Center (IDC) serves as the consultation and clarification branch of the verification regime. The IDC processes and analyzes data from the IMS and sends it to Member

States for review and judgment [1]. Therefore, the IDC has the important task of maintaining the global monitoring data set and ensuring that the stations are operating as appropriate. OSI is the final verification measure of the CTBTO and requires 30 of the 51 Member States votes to concur [18]. To this end, inspectors travel directly to the site of the suspected nuclear explosion and collect information. Confidence building measures for the CTBT include notification of chemical explosions and collaboration between parties for calibration of IMS stations with chemical explosions [18].

1.2.3 Motivation for Detection Improvements

One argument against ratifying the CTBT is that without nuclear testing, current weapons arsenals run the risk of being defective, therefore limiting the effectiveness of mutually assured destruction. Additionally, limiting nuclear testing, forces modernization of current arsenals to be done through simulations. Lack of testing to verify weapons capabilities makes states that are party to the treaty vulnerable to nuclear attack if their arsenal is defective and is a big point of contention for NWS. As a result, the US and China are the only P5 countries that have not ratified the CTBT [1], whereas Russia, France, and the UK have both signed and ratified the treaty. Israel has signed, but not ratified, the treaty and has not acknowledged its weapons program; Israel is not party to the NPT and no nuclear testing has been declared.

Additionally, India, Pakistan, and North Korea have neither signed nor ratified the treaty, which is a requirement for the treaty to go into force. As mentioned previously, India has been pushing for the elimination of nuclear weapons on an agreed timeline, and wanted this included in the CTBT [30]. Also, because of the perceived collusion between Pakistan and China, India pursued nuclear weapons for security purposes [30]. As a result, it is assumed that Pakistan has not signed so that progress can continue on its nuclear weapons program. Pakistan has however, proposed a bilateral non-testing arrangement to India, but there has been no response [31]. North Korea has been reluctant to join treaties with intrusive verification measures [32], although all declared nuclear

weapons tests have been measured by the IMS [1].

If the IMS has the capability to detect any clandestine nuclear weapons test, then the proliferation of nuclear weapons would be minimized, and eventually complete nuclear disarmament could occur. An advanced radioxenon detector would improve the sensitivity of the IMS particularly to low-yield nuclear explosions. As a result, it would make hiding nuclear explosions even more difficult strengthening the argument for ratification of the CTBT.

To improve upon the current detector limitations, detector development is focused on:

1. Improved energy resolution
2. Maximized detection efficiency
3. Minimized memory effect.

The improved resolution of the system minimizes isotopic interference increasing the accuracy of the measurement. Maximizing the detection efficiency of the system increases the sensitivity of the system. Minimizing the memory effect further increases the sensitivity of the system and allows for a higher frequency of measurements to be taken, improving the capabilities of the IMS. These improvements all drive the sensitivity of the system down, resulting in a lower minimal detectable concentration (MDC). The lower MDC leads to fewer false negatives because isotopes can be better discriminated from background and interferences. The improved sensitivity, from a lower MDC, also allows for more precise and accurate measurements, which improves the enforceability of the CTBT. As a result, many detectors have been built and tested with emphasis on improving sensitivity to better detect and identify sources of radioxenon. Furthermore, simulations play a large role in nuclear explosion monitoring. From atmospheric transport modeling, to analysis training spectra, simulations are needed to better understand radioxenon detection and analysis.

1.3 Thesis Contribution and Overview

The detection and identification of the metastable xenon isotopes (^{131m}Xe and ^{133m}Xe) is vital to the characterization of the sources of radioxenon, particularly when attempting to discriminate nuclear explosions from civilian sources of radioxenon. To better detect and identify these isotopes, especially in the presence of interference, advanced radioxenon detection systems and techniques are needed. This thesis approaches the issue from three angles: 1) the development of an alternative analysis method to better identify metastable isotopes, 2) the development and validation of an MCNPX-PoliMi simulation tool to analyze alternative detector systems and produce training spectra for analysis testing, and 3) the development of an advanced radioxenon detector system using a stilbene beta cell. The methodology of the alternative analysis technique was established. The technique was then applied to experimental data and simulations and compared to the traditional analysis technique. The alternative analysis method has proven to be more sensitive than the traditional method at specific interference levels. The original correlated decay model for MCNPX-PoliMi was updated in stages to better simulate radioxenon decay and detector response. The MCNPX-PoliMi code has been validated and agrees well with experimental data. Preliminary experiments and simulations were conducted to analyze the benefits of using stilbene as the beta detector in place of plastic. Stilbene beta cell prototypes were manufactured and tested alongside plastic beta cell detectors. The stilbene cell has shown improvements over the plastic cell, most notably the significant decrease in memory effect.

The following is a summary of the remaining chapters:

Chapter 2: Background on nuclear fission and radioxenon decay is discussed. A summary of the methods for radiation detection is presented. A literature review of radioxenon detector development is presented. Sources of radioxenon and limitations of the current detector systems are discussed.

Chapter 3: Radioxenon detector calibration techniques are discussed. Traditional radioxenon

analysis methods are discussed. An alternative analysis method, anticoincidence, is presented and compared to the traditional method.

Chapter 4: The development of MCNPX-PoliMi for radioxenon detection is presented. A summary of updates to the codes is presented with progression of the tool discussed. Results from the validation measurements are presented.

Chapter 5: Radioxenon detector development of a stilbene beta cell is presented. Experimental methods are discussed and results from three prototypes are presented. A full calibration of the final prototype has been conducted and the results are compared to a plastic beta cell detector.

Chapter 2

Background

Nuclear fission occurs when heavy elements split into fragments known as fission products. Neutrons are also produced, further inducing additional fission reactions producing a chain reaction. This chain reaction is fundamental to nuclear energy and nuclear weapons. Of the fissionable isotopes, uranium and plutonium are most widely used. A variety of isotopes are released in the process, based on the fission mass yield curve of the isotope as shown in Figure 2.1.

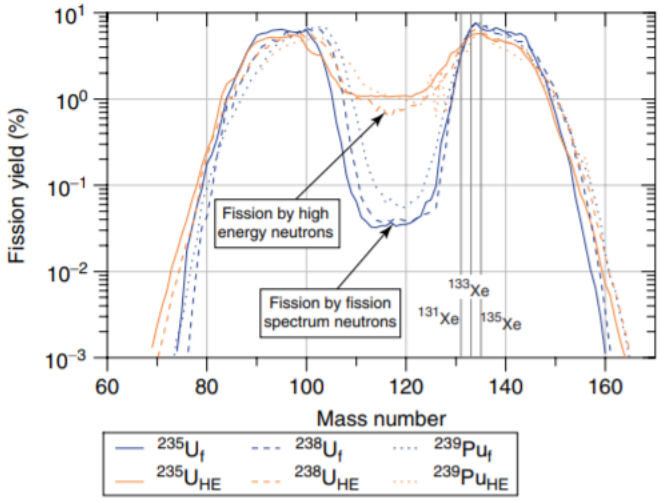

Figure 2.1: Fission yield mass curve for ^{235}U, ^{238}U, ^{239}Pu for fission induced by thermal (0.025 eV) and high-energy (14 MeV) neutrons with the percentages of the radioxenon isotopes of interest highlighted, taken from the chapter on xenon from the *Encyclopedia of Inorganic Chemistry* [33].

Many of the fission fragments can be found in particulate samples from nuclear explosions. However,

in the case of underground explosions, noble gases are of great importance due to their ability to escape and be detected. For uranium and plutonium, xenon has the highest cumulative fission yield of the noble gases produced. Other noble gases that are measured for nuclear explosion forensics are ^{37}Ar and ^{85}Kr. There are four isotopes of interest for verification of the CTBT: ^{135}Xe, ^{133}Xe, ^{133m}Xe, and ^{131m}Xe. The cumulative fission yields for ^{135}Xe, ^{133}Xe, ^{133m}Xe, and ^{131m}Xe are 6.61%, 6.6%, 0.189%, and 0.0313% for ^{235}U induced by thermal neutrons, and 7.36%, 6.99%, 0.216%, and 0.041% for ^{239}Pu induced by thermal neutrons respectively [34].

2.1 Radioxenon Decay

Each of the isotopes of interest emits a beta or conversion electron, with a photon or X-ray immediately following or in coincidence for detection purposes. To detect each isotope, a region of interest (ROI) is identified based on the emission energies. The specific decay and particles emissions for each of the isotopes of interest is discussed below. The resultant beta-gamma coincidence spectrum is discussed in Section 2.2.1.

2.1.1 Xenon-135

The shortest-lived isotope of interest is ^{135}Xe, having a half-life of 9.14 hours. The decay scheme of ^{135}Xe is shown in Figure 2.2. This isotope undergoes β^- decay, where a neutron is converted into a proton, emitting a beta (electron) and antineutrino. The beta and antineutrino share the Q-value energy, resulting in a range of energies for the beta particle up to the endpoint energy, which is the maximum of the Q-value. The endpoint energy for the primary beta decay level of ^{135}Xe is ~910 keV. As shown, the 250 keV photon is most commonly emitted in coincidence with the beta particle, resulting in one region of interest for ^{135}Xe. The coincidence emission at this energy level is also highlighted in the coincidence spectrum.

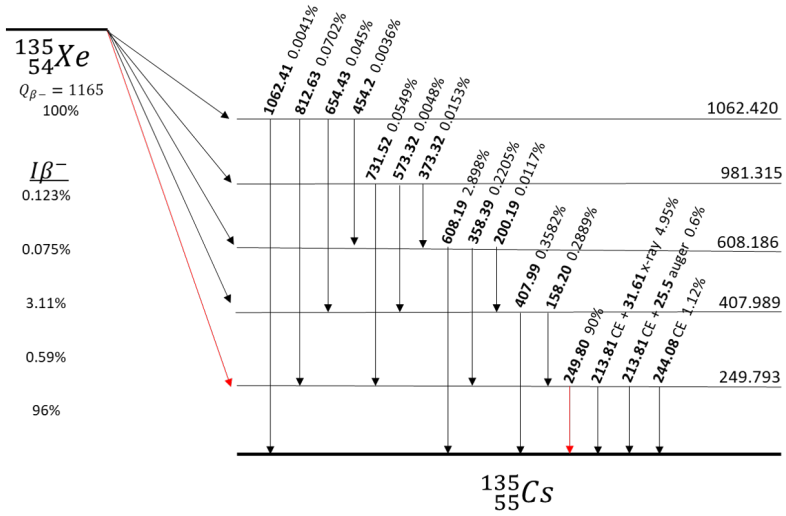

Figure 2.2: Decay scheme for ^{135}Xe.

2.1.2 Xenon-133

The half-life of ^{133}Xe is approximately 5.25 days and has the most complex decay scheme of the isotopes of interest. At the primary energy level for the β^- decay (81 keV), the internal conversion coefficient (α) is greater than one resulting in de-excitation of the nucleus through electron and gamma emissions. The electron emission for this isotope is primarily a 45 keV conversion electron (CE) in coincidence with an average 30 keV X-ray; the X-rays emitted have a range of energies. The gamma emission is primarily an 81 keV photon. The decay scheme is shown in Figure 2.3 and results in two regions of interest for ^{133}Xe.

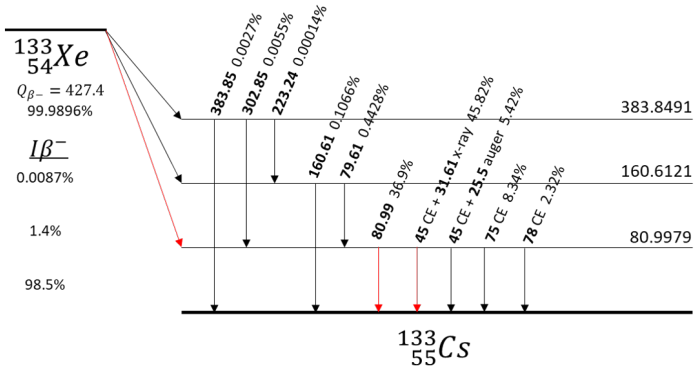

Figure 2.3: Decay scheme for ^{133}Xe.

2.1.3 Xenon-133m

The isotope ^{133m}Xe is the metastable isotope for ^{133}Xe with a half-life of 2.2 days. This isotope decays through internal conversion, where either a CE is emitted with an X-ray or Auger electron, or a photon is emitted based on the de-excitation energy level as shown in Figure 2.4. The most probable CE emitted in coincidence is 199 keV with an approximate 30 keV X-ray. The ROI for ^{133m}Xe is a small box instead of a rectangle since the CE has a distinct energy. Because this isotope is constantly decaying into ^{133}Xe, it is never measured as a pure isotope. Additionally, the characteristic X-rays of ^{133m}Xe have a similar energy range to those emitted by ^{133}Xe, thus the ^{133m}Xe ROI is within the boundaries of the ^{133}Xe 30 keV ROI.

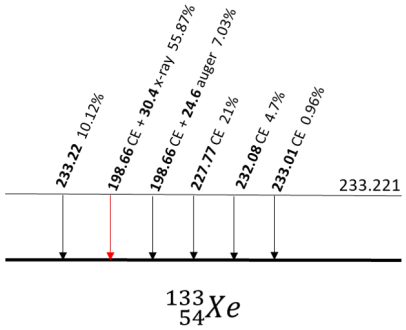

Figure 2.4: Decay scheme for ^{133m}Xe.

2.1.4 Xenon-131m

The isotope ^{131m}Xe is the metastable isotope for ^{131}Xe, has a half-life of 11.84 days and has the simplest decay scheme of the four isotopes of interest as shown in Figure 2.5. As with ^{133m}Xe, ^{131m}Xe decays through internal conversion producing emissions based on the de-excitation energy level. The most probable CE emitted in coincidence is 129 keV, also with an approximate 30 keV X-ray, again producing a tight ROI. Similar to ^{133m}Xe, the ROI for ^{131m}Xe is within the boundaries of the ^{133}Xe 30 keV ROI due to the common characteristic X-rays. Additionally, depending on the beta detector resolution, the CEs emitted by the metastable isotopes can overlap.

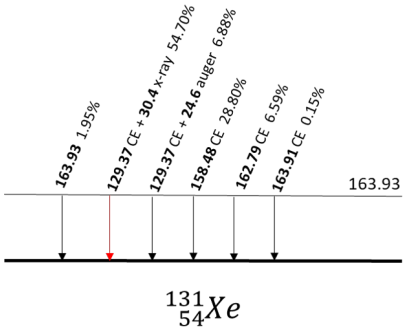

Figure 2.5: Decay scheme for ^{131m}Xe.

2.2 Radiation Detection for Beta-Gamma Coincidence

Measurement of radioxenon through beta-gamma coincidence requires a cell to contain the gas, a beta detector, and a gamma detector. This section gives a summary of the detection mechanisms for the most commonly used beta-gamma coincidence detector: plastic and NaI(Tl). For a more in-depth discussion on detector types and detection mechanisms, refer to [35, 36].

Scintillator detectors fluorescence when de-excitation of the atomic molecules occurs. For inorganic scintillators, fluorescence is due to the impurities introduced in the crystalline structure that allow for de-excitation of the electron-hole pairs through activation sites [35]. For organic scintillators, fluorescence is due to transitions between the energy levels of the molecule [35]. The fraction of kinetic energy that is converted to light, known as the light output, characterizes the performance, where inorganics have a higher light output than organics. This light is converted to pulses using a light sensing device, typically a photomultiplier tube (PMT). A key benefit of the de-excitation mechanism of organic scintillators is that the emission time of the light is dependent on the rate of energy loss. Therefore, through pulse shape analysis, some organic scintillators can discriminate between the different particle types, and are considered to pulse shape discrimination (PSD) capable.

The NaI(Tl) detectors used for radioxenon detection were chosen because of their low-cost, gamma efficiency, resolution, and ease to manufacture. To maximize coincidence detection efficiency, a

well is typically drilled into the crystal where the plastic cell is placed resulting in a near 4-pi geometry. For radioxenon measurements, the photons emitted interact with inorganic scintillators through two primary modes: Compton scattering and photoelectric effect. Compton scattering occurs when the photon ($h\nu$) is deflected at some angle (θ) by scattering on an electron, transferring a portion of its energy in the process. Compton scattering produces a continuum in the pulse height spectrum due to the transfer of energy occurring at all scattering angles. The energy of the recoil electron is given by

$$E_{e^-} = h\nu - h\nu' \tag{2.1}$$

$$h\nu' = \frac{h\nu}{1 + \frac{h\nu}{m_0c^2}(1 - cos\theta)} \tag{2.2}$$

where m_0c^2 is 511 keV, electron rest mass energy [35]. The Klein-Nishina formula predicts the distribution of the scattered photons, where forward scattering is favored at high energies [35]. Photoelectric absorption occurs when a photon interacts with the atom and disappears, resulting in the emission of a photoelectron. Photoelectric absorption produces a full energy peak in the pulse height spectrum due to photoelectron emission. The energy of the photoelectron is given by

$$E_{e^-} = h\nu - E_b \tag{2.3}$$

where E_b is the binding energy of the photoelectron in its original shell resulting in transfer of most of the original photon energy [35].

The plastic cells used for radioxenon detection were chosen because of their ease to manufacture into a variety of shapes, specifically hollow shapes. Creating a hollow plastic cell enables it to

be used as both the gas container and beta detector. The thickness of the plastic cells results in a detection efficiency of almost 100%, due to the limited range of electrons. Therefore, the energy of the radioxenon electrons is fully absorbed in the material resulting in full-energy peaks. However, full-energy peaks are only visually apparent with the CE emissions since beta decay results in a range of electron energies. The use of plastic, a low-Z material, as the container for the radioxenon samples also minimizes the attenuation of photons further maximizing the coincidence detection efficiency. A coincidence time window is set up between the beta detector and the gamma detector to identify coincidence events.

2.2.1 Beta-Gamma Coincidence Spectrum

As mentioned previously, the primary mode of detection for radioxenon is beta-gamma coincidence. Detector background is minimized by requiring coincident events, because the ambient coincidence background count rate is typically low. Additionally, detecting related particle emissions increases the probability of correctly identifying the isotope of interest. The isotopes are identified using ROIs, which represent the respective isotopes primary coincidence. Figure 2.6 shows the simulation of a coincidence spectrum containing the four isotopes of interest. The energy deposited in the beta cell is plotted along the x-axis, and the energy deposited in the NaI(Tl) detector is plotted on the y-axis. Each dot in the 2-D histogram is a matrix element and representative of the number of coincidences counts at the specific beta-gamma energies. The color bar to the right gives a visual representation of the counts, where regions of higher counts correspond to primary coincidence emissions. The quantification methods of the isotopes are discussed in Chapter 3.

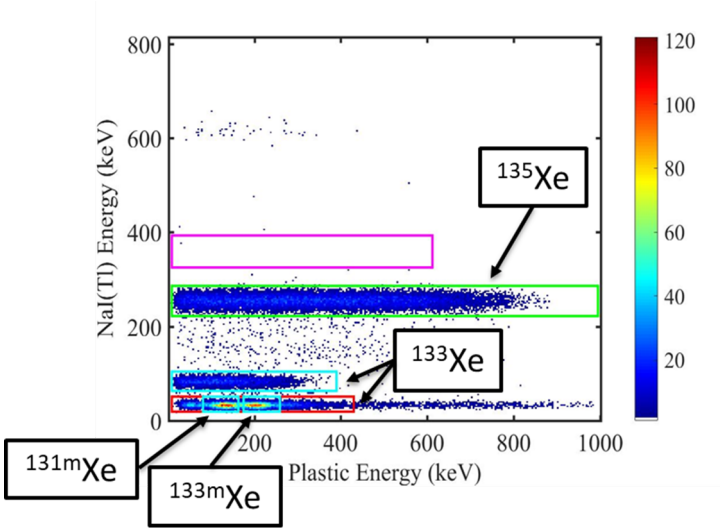

Figure 2.6: Beta-gamma coincidence detection simulation [37] highlighting the ROIs of the radioxenon isotopes of interest.

2.3 Literary Review of Radioxenon Detectors for Nuclear Explosion Monitoring

The previous section summarized the primary mechanisms used for coincidence detection of radioxenon. In 2010, Auer [38] discussed the past ten years of development of equipment for radioxenon monitoring. During this time, the systems developed for use in the IMS were the Automatic Radioanalyzer for Isotopic Xenon (ARIX), Automated Radioxenon Sampler-Analyzer (ARSA), Swedish Automatic Unit for Noble Gas Acquisition (SAUNA), and Système de Prélèvement Automatique en Ligne avec l'Analyse du Xénon (SPALAX). Each system is meant to be automated and thus contains a gas processing system as well as a robust radioxenon measurement system that has a minimum detectable concentration (MDC) of 1 mBq/m^3 for ^{133}Xe. Although the steps for each system are different the overall technique is the same: xenon is extracted from the air through its adsorption on activated charcoal, after which the xenon is released by heating the charcoal and flushing it with a carrier gas, and then passed through a system of traps to remove ^{222}Rn and other atmospheric gases [39].

Varying factors such as, decreasing the number of photomultiplier tubes (PMT) for easier gain matching and calibration, better sensitivity, higher resolution, and increased detection efficiency,

resulted in modifications to some of the existing systems discussed in the introduction. As technology has developed, an emphasis has been placed on increasing the sensitivity and resolution of the detectors. Particularly, the need to distinguish the metastable isotopes (^{131m}Xe and ^{133m}Xe) from the ground isotopes (^{133}Xe and ^{135}Xe) focused the development of these new systems. The following presents a literary review on the various detector types that have been developed.

2.3.1 Gamma Spectroscopy Detectors

The detectors discussed in this section typically consist of high-resolution detectors along with a container to hold the gas sample. The detector used in the SPALAX^{TM} system consists of a single high-purity germanium (HPGe) detector, with a planar crystal, and a counting cell. This approach was preferred to beta-gamma coincidence because of the ability to detect all four xenon isotopes with high spectral resolution. The SPALAX HPGe approach, while needing cooling, requires a less complex system, making it suitable for on-site usage [40].

An improved system was developed using a broad energy germanium (BEGe) detector and a carbon fiber counting cell. The BEGe detector design has energy coverage from 3 keV to 3 MeV and is especially enhanced for efficiency below 1 MeV, which is ideal for radioxenon measurements. The carbon fiber entrance window allows the transmission of more than 85% of photons with 10 keV energy and almost 100% transmission of photons with energies higher than 20 keV, improving the efficiencies of the SPALAX aluminum window by a factor of 2.3 [41, 42].

In 2014, a system using two HPGe detectors, with planar crystals, was developed. For this system, the gas source was contained in a cell with carbon fiber windows and placed between the two detectors, where the spectrum from each was summed into one using GammaVision software [43]. By replacing the source cell window with carbon fiber, the detection sensitivity for the metastable isotopes (^{131m}Xe and ^{133m}Xe) was improved [43]. The benefit of using two detectors was the increased full energy peak efficiency; however, summing the spectra caused an increase to the MDC [43]. A large well germanium detector was tested in [44]. The end cap that covers the well was

constructed of Vespel, a polymide thermosetting plastic which minimized the attenuation of the low-energy radioxenon gamma rays [44].

2.3.2 Beta - Gamma Coincidence Detectors

The use of beta-gamma coincidence for radioxenon detection enables the use of room-temperature detectors. The detectors discussed in this section typically consist of an electron detector that also acts as the sample container and a photon detector. The detection events from each detector are analyzed within a predetermined time window for coincident energy deposition and used to create a 2-D histogram spectrum to measure radioxenon. The use of coincidence measurements leads to a significant reduction of the background allowing the systems to have MDCs below the IMS requirements [38]. Additionally, most of the systems have a near-4π geometry allowing for high efficiency measurements. The most commonly-adopted beta-gamma coincidence detector uses a plastic cell as the electron detector and a NaI(Tl) detector as the photon detector. Several detector geometries are discussed in references [45–49]. Figure 2.7 shows schematics of the detectors used in the ARSA and SAUNA systems. The ARIX system is slightly different than the ARSA and SAUNA systems consisting of a well-type NaI gamma detector and a thin-wall aluminum measuring chamber, coated with polystyrene, an organic scintillator [48]. Instead of 2-D coincidence measurements, the early ARIX systems relied on beta-gated gamma measurements, where the detector only records the gamma spectrum if an electron was detected [48].

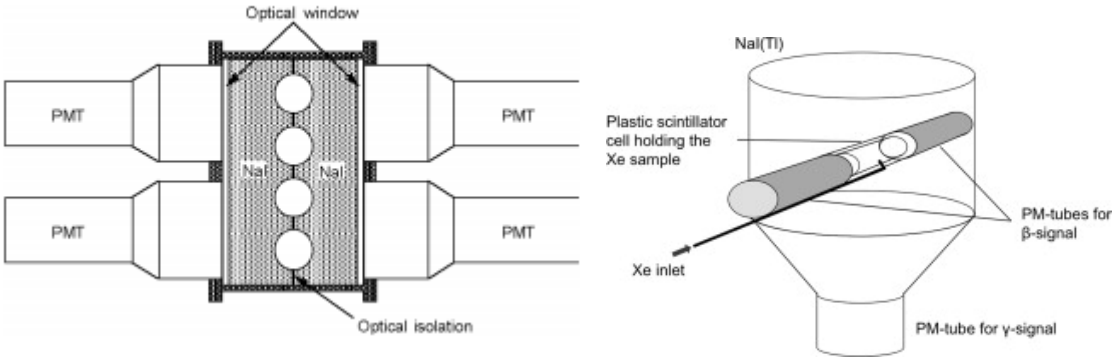

Figure 2.7: Schematic images of the ARSA and SAUNA detectors [46, 50]

The original design of the ARSA system made it complicated to calibrate because of the need to gain match PMTs. Pacific Northwest National Laboratory (PNNL) constructed a new plastic scintillation gas cell, and did an initial comparison of three different well-type detectors: NaI(Tl), CsI(Na), and CsI(Tl) [51]. From this analysis, CsI(Na) was chosen as the replacement due to its good mechanical properties, better efficiency, and similar time constant to NaI(Tl) so that electronics would not be affected [51].

A simplified β-γ coincident detector was developed in 2007 to improve the ARSA system [52]. The design consisted of set of four single CsI(Na) well detector and gas cell, each detector with a single PMT. The overall detection efficiency improved with the increase of the solid angle of detection and the beta cell energy resolution was maintained by rounding the ends of the cell and using a larger PMT [52]. Ultimately, this detector decreased the complexity of the quality assurance and control through each set being able to be calibrated independently of the others. In a study of the CsI(Na) crystals, it was found that the presence of Cesium in the detector crystal allows excitation of the detector material causing the same X-ray energies to be produced as those produced by the decay of ground state radioxenon isotopes (31 keV X-rays), causing degradation in this energy peak [53]. In 2016 a similar detector set up to that discussed in Cooper [52], using a well-type NaI(Tl) and BC-400 cylindrical plastic scintillator, was used to create the Iranian Noble Gas Analyzing System (INGAS) [54]. Through the use of check sources and Monte Carlo simulations, the energy resolution, efficiency, and minimum detectable activity of this system were measured and shown to be comparable with previously developed radioxenon systems.

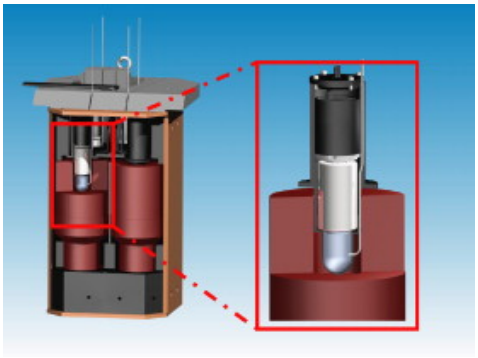

Figure 2.8: Schematic of coincidence detector with rounded plastic cell [52]

2.3.2.1 Silicon

In 2012, Hennig [55] studied silicon as an alternate for high resolution radioxenon measurements, potential advantages being high resolution, low background, and sensitivity to both photons and electrons. From these studies, for a 100 mm^2 side of an Si detector, he concluded that the probability of full energy deposition of an electron was 12%; for photons, it depended strongly on the energy, ranging from 14% to 2% for 4.1 keV and 30 keV, respectively [55]. However, very good energy resolutions (below 1 keV for most energies) were shown to be useful for separating the xenon X-rays of the four isotopes. Due to the ability of the high energy photons and electrons of ^{135}Xe (250 keV and 905 keV, respectively) to pass through the silicon detector, it was recommended that these high energy particles be measured using an additional component [55].

A beta-gamma coincidence, muon-photon anti-coincidence detector was developed in Austria in 2010. The nuclear detector consisted of a fully depleted silicon surface barrier detector for electron detection, a HPGe detector for gamma detection, lead shielding, and six plastic scintillator guard detectors for cosmic muon detection [56]. The plastic scintillator can differentiate between the terrestrial background radiation and the energy deposited by the cosmic muons through pulse shape discrimination [56]. The muon-photon anti-coincidence reduced the number of background counts by a factor of 1.98 ± 0.14 and reduced the memory effect [56]. This approach helps compensate for the low detection efficiency due to the 2π geometry and provides increased sensitivity [56].

A 24-element PIN diode detector was developed by Cox [57] in 2013. It contained four 25 mm^2 PIN diodes on each of six sides of a cube made of copper, for a total active area of 600 mm^2 [57]. To reduce cross talk, data collection was inhibited during the reset of any PIN diode, increasing the total dead time of the detector [57]. To analyze the measurement, the digital outputs were summed after pulse processing and some peak broadening was observed, which was said to be multiplets in the electron peak attributes, electron absorption in the gas sample and entrance window of the detector, and electron backscatter, thus deconvolution software was required [57]. Coincidence gating between the diodes allowed for the measurement of conversion electron/beta coincidences, which is not possible when using a single electron detector such as plastic [57].

In 2013, Le Petit [58] developed a gas cell with two large planar silicon (PIPS) detectors for radioxenon measurements. The gas cell was surrounded by a well-type NaI(Tl) detector with the window facing the gas cell having a thick aluminum layer to minimize the attenuation at 30 keV [58]. The solid angle of the PIPS detector was calculated to be 0.526 ± 0.041; however, the detection efficiency was experimentally determined to be lower due to PIPSbox dead volume [58]. Due to the optimization of the silicon depletion region (to minimize noise) and the geometry of the PIPSbox, at least 60% of the beta emissions are fully depleted [58]. Additionally, no memory effect was observed when the gas volume was vacuumed for 10 hours [58].

The detection system developed in Le Petit [58], was improved by using a HPGe detector instead of NaI(Tl). By using high resolution for both electron and photon detection, complete distinction between metastable and ground state isotopes can be done as well as distinction between ^{131m}Xe and ^{133m}Xe [59]. The photon energy resolution also allows clear distinction between radon and radioxenon peaks, which is useful for detecting radioxenon in an environmental sample where radon progenies could be preset [59]. The efficiency of this detector was significantly higher than the detector in [56].

In Le Petit [60], a new SPALAX^{TM} system was developed with high energy resolution for electrons

and photons, using a BEGe detector and PIPSBOX^{TM}. The PIPSBOX^{TM} is a "leak tight gas cell made of ultrapure aluminum fitted with two face-to-face large area PIPS detectors from Canberra Semiconductor NV" [60]. The introduction of these high-resolution systems provides the possibility of more accurate measurements at low levels since the interference correction factors are weak and the availability of triple coincidence measurements could improve metastable radioxenon detection sensitivity [60]. Additionally, the memory effect factor is less than 0.1% and a new type of radionuclide station has been proposed with the capability of measuring particulate and noble gas samples without any spectral interferences due to the high resolution of the detectors [60].

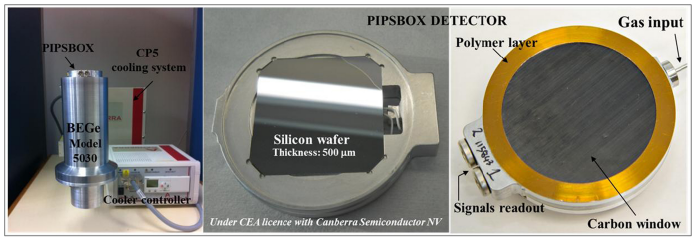

Figure 2.9: Next generation SPALAX detector developed by CEA [60]

2.3.3 Alternative Detectors

Many alternative detectors have been developed over the years to further improve radioxenon measurements. The detectors discussed in this section are mostly experimental, and include proportional counters, various scintillators, and CdZnTe (CZT).

A high-pressure plastic scintillation detector was developed and tested in 1999. Flow detectors were integrated into a portable Gas Analysis, Separation, and Purification system (GASP), with the idea of calculating the count rate measured by the detector as a function of pressure and flow rate [61]. However, due to the high-pressure operation of the system, self-absorption caused the detection of beta particles to be inefficient above a certain pressure limit [61].

A detector consisting of gas proportional scintillator counters (GPSCs), a multi-wire proportional counter (MWPC), and silicon detectors was developed and tested in 2003. The sample chamber consisted of two silicon surface-barrier detectors placed in a face-to-face configuration and spaced

such that they created a MWPC using the gas sample as the filing gas and placing the wire in between the two detectors [62]. These components were enclosed in a beryllium pillbox forming a sample chamber which was surrounded by twin GSPCs, allowing for detection of conversion electrons in coincidence with X-rays [62]. The energy resolution of the GPSCs was 1.4 keV for 30 keV X-rays and the energy resolution of the silicon detectors was no greater than 25 keV for electrons [62]. Also, the use of gas detectors reduced the cosmic-ray background counting rate to about 1 Bq compared with scintillators; however, it was suggested that an inorganic scintillator be included to improve the detection efficiency for ^{133}Xe and ^{135}Xe [62].

A triple-coincidence detector was developed in hopes of eliminating the need for chemical separations altogether. The detector consisted of a 60-cc gas cell made of two paddles of plastic scintillator with a Mylar sheet in between and two NaI(Tl) detectors placed against the paddles [63]. The detector electronics were modified such that the only events captured were those that interacted in both scintillator paddles and one NaI detectors. The triple-coincidence data shows a reduction in the Compton-scattered background and shows that the radon interference is reduced, and makes it possible to measure much lower levels of radioxenon which radon contamination; however, some cross talk is shown in the measurements [63].

In Ranjbar [64], a prototype CZT detector was developed. The detector consisted of two co-planar CZT detectors and uses beta-gamma coincidence by detecting the electron in one detector and the photon in the other detector. The detector was also able to make triple coincidence measurements [64]. The memory effect is expected to be improved due to the crystalline structure of the material inhibiting the diffusion of xenon into the material. In this prototype, the geometric efficiency is low due to the use of only two crystals causing the MDC to be higher than the 1 mBq/m^3 limit. It is estimated that using a six-element detector will improve the geometric efficiency and lower the MDC [64]. A detector consisting of plastic and CZT is also being developed [65].

2.3.3.1 Phoswich Detectors

The idea of the phoswich detector came from combining two different phosphorous materials together in a sandwich, which was then viewed by a single light detection system [66]. Generally, a slow decay-time material is combined with a fast-decay time material and read out by a PMT. Pulse shape discrimination occurs by calculating the ratio of the integral of the tail of the pulse and the total of the pulse. In the case of beta-gamma detection, it was hypothesized that a single beta-gamma coincidence pulse could be deconvoluted into its gamma and beta components and that a single detector could be used to perform isotopic identification based on the separated energies [66]. This section is ordered chronologically by institution.

The detector used in Ely [66], was a cylindrical NaI crystal with a thick window of CaF_2(Eu) on one end separated by a quartz optical window, and on the opposite end was a PMT. The gas cell was an aluminum hollow cylinder that was attached to the detector. Measuring radioxenon, the fast and slow rising pulses can be separated into two distinct distributions and it appeared that the detector can differentiate between pulses formed in the NaI and CaF_2(Eu) [66]. However, pulses with rise times in between the two distinct distributions were not able to be identified from the method used in [66]. A phoswich detector consisting of yttrium aluminum perovski (YAP) and bismuth germanate (BGO) was also tested but, due to the thickness of the YAP, the 30-keV X-ray was attenuated [67].

In Hennig [68], a study was conducted to analyze the performance of optically coupled plastic and CsI(Tl) scintillator for measuring radioxenon. Digital pulse shape analysis (PSA) was used to determine if the interaction occurred in either or both parts of the detector as well as measure the energy deposited, using a single PMT. The prototype detector was enough to develop the PSA algorithms but had a very low detection efficiency due to the geometry of the measurement with at least half of the sample being emitted away from the detector [68]. The PSA algorithm correctly classified events with an efficiency of at least 95-97% [68].

The PhosWatch detector consisted of a BC-404 plastic cell, enclosed in and optically coupled to a CsI(Tl) cylinder [69, 70]. Using CsI(Tl), the photon energy resolution was approximately 7.3% at 662 keV, and due to the detection of low energy X-rays, the efficiency was increased [70]. Additionally, since the system only used one PMT, the need for gain matching was eliminated and, because compact electronics were used, the physical size of the detector was reduced allowing it to be field deployable [70].

The PhosWatch detector was redesigned in 2014 to reduce size, weight, cost, complexity, and memory effect [71]. After test simulations, the detector built consisted of two BC-404 plates with aluminum coated Mylar film to combat the memory effect and a CsI(Tl) cylindrical crystal split in half to go on each side of the plates. Using the Mylar reduced the memory effect to below 1% [71]. The resolution of the system is similar to that of the PhosWatch detector developed in 2009 and the coincidence spectra are similar to that of the SAUNA and ARSA systems minus a few differences due to the geometry of the detector [71]. A planar stilbene and CsI(Tl) detector was also tested and was shown to have a decreased memory effect (~0.1%) and pulse shape discrimination capabilities, however the material composition made it difficult to contain the gas sample [72].

In 2007, another phoswich detector was developed for alpha, beta, and gamma spectroscopy using a plastic scintillator and NaI(Tl) combined with liquid scintillators and the data processing was done using digital PSD analysis [73]. This detector with the use of the liquid scintillator was able to measure low radioactive levels from actinides and increase the alpha detection efficiency to 70%. [73].

A triple layer phoswich detector was analyzed for beta-gamma coincidence measurements. The detector consisted of BC-400 plastic scintillator, CaF_2(Eu) inorganic crystal, and NaI inorganic scintillator [74]. A customized digital pulse processor (DPP) was developed at Oregon State University to characterize the pulses and showed that the system had better discrimination for low-energy beta and gamma sources, but for high energy radiations, a larger portion of the pulses

were mischaracterized or rejected due to the presence of dual components in the pulses [74].

The phoswich detector developed at Oregon State University was improved by using three scintillation layers, BC-400, CsI(Tl), and BGO [75]. The BC-400 acts as the gas cell and the electron detector, the CsI(Tl) acts as the photon detector, and the BGO is used for Compton suppression. Field Programmable Gate Array (FPGA) processing was developed for the Compton suppressed phoswich detector [76]. The Compton suppression mechanism reduced the Compton continuum by 20-50% in the low energy region of the spectrum [75].

A well-type phoswich detector was also developed. It was fabricated by optically coupling BC-400, CsI(Tl), and BGO to a single photomultiplier tube using concentric cylinders [77]. This detector also used pulse shape discrimination to determine the origin of interaction. However, there was degradation in the energy resolution likely due to poor light collection efficiency [77].

2.4 Sources of Radioxenon

In addition to nuclear explosions, radioxenon is emitted from a variety of civilian nuclear processes, including nuclear reactors and medical isotope production facilities (MIPFs). These various sources contributed to the background of the IMS. As an example, the average order of magnitude releases from sources of radioxenon in Becquerel are: 10^9 for nuclear power plants, 10^{14}- 10^{15} for the North Korean nuclear explosion in 2006, 10^{12} - 10^{14} for fission-based isotope production, and 10^{19} for the Fukushima nuclear accident [78]. Therefore, it is important to understand the signatures of these radioxenon sources in addition to explosion signatures.

Nuclear reactors contribute to the global ^{133}Xe background, particularly to IMS stations that are within the wind trajectory of the facility. Starting in 1997, various in-field experiments were conducted using ATM to show that elevated ^{133}Xe measurements were due to reactor releases [79–84]. Results of these studies showed that approximately 10^{15} Bq is released collectively by North American and European nuclear power plants per year [83], resulting in a background of

several mBq/m^3 [81]. Research reactors also contribute to the IMS station backgrounds as shown in the TRIGA Mark II study in Vienna, where five radioxenon isotopes were detected [85, 86]. Additionally, reactor accidents, Chernobyl and Fukushima, have been measured using radionuclide detection technologies [25, 43, 87–91]. The Fukushima accident was measured at a number of IMS stations and ATM models were able to help identify and quantify the radioactive isotope releases. This accident further illustrated the capabilities of the IMS [25, 88–91].

MIPFs also contribute to the global ^{133}Xe background. A single MIPF emission can exceed all nuclear power plants collectively based on the study conducted in [83]. A study conducted during the shutdown of MIPFs in Canada and Europe showed a noticeable reduction (one to two orders of magnitude) of radioxenon peak values during the shutdown period [92]. MIPFs also produce radioxenon samples of ^{133}Xe, which is contaminated with ^{131m}Xe, that shows up as the same decays due to its longer half-life [93]. Stack monitoring of BaTek MIPF showed that ^{133}Xe and ^{135}Xe were typically observed [94, 95]. Additional MIPFs studies are discussed in [20, 24, 78, 92, 96–102].

The focus of the IMS is the detection of nuclear explosions. The five declared nuclear tests by the Democratic People's Republic of Korea (DPRK) are the only nuclear tests that have been conducted in the last 15 years. These tests have been measured by at least one technology of the IMS, typically seismic. However, the tests in 2006 and 2013, released radioxenon signatures that were detected by IMS stations. The nuclear test in 2006 was detected in Yellowknife, Canada, with ^{133}Xe levels consistent with a 10% hypothetical release of a one kiloton underground nuclear explosion [103]. A mobile radioxenon sampling system in the Republic of South Korea also detected ^{133}Xe and ^{131m}Xe, from the nuclear test in 2006 [104]. at IMS stations in Japan and Russia also detected ^{133}Xe and ^{131m}Xe from the nuclear test in 2013[105].

2.4.1 Isotopic Ratios

In order to distinguish between the different sources of radioxenon, the ratios of the isotopes of interest are used as shown in Figure 2.10. As discussed, radioxenon has been measured from a

variety of sources which can be separated into three main groups: nuclear explosions, nuclear power plants, and MIPFs. Kalinowski used experimental data as well as simulation data to develop a multi-isotopic ratio correlation (MIRC) plot that can be used to discriminate between the different sources. However, as shown in Figure 2.10, there are cases where the signatures from a civilian source overlap those of nuclear explosions. Therefore, it is important that not only is the isotope of interest detected, but it also has to be quantified with high certainty to reduce the chances for misclassification of the source.

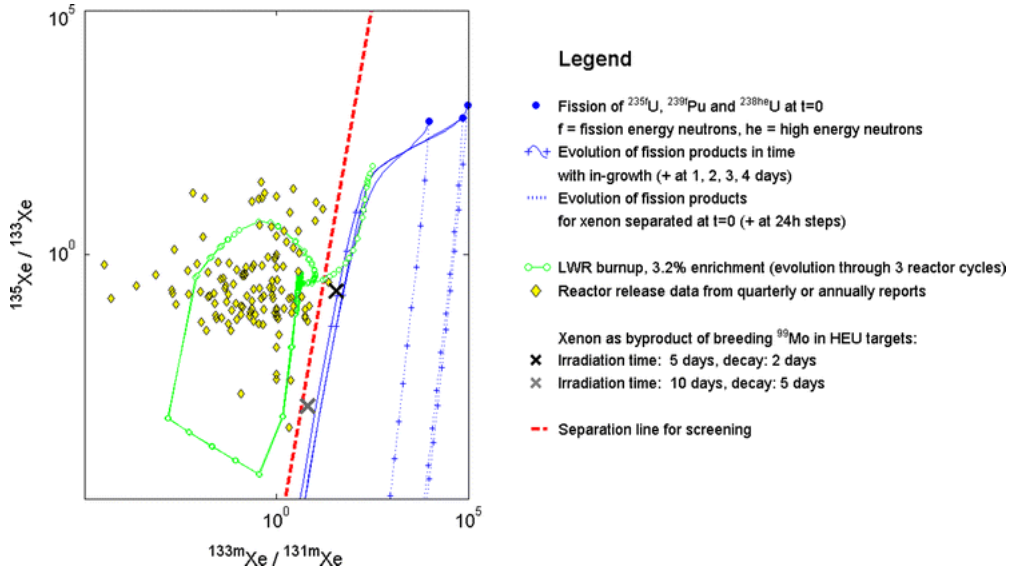

Figure 2.10: Example isotopic ratio plot developed in [106] for distinguishing sources of radioxenon.

The identification and quantification of the metastable isotopes is very important to radioxenon source characterization. As discussed in [85], metastable isotopes play a vital role in distinguishing the sources of radioxenon. Using previously published data, Figure 2.11 shows how sources of radioxenon can be discriminated using only two isotopes, ^{131m}Xe and ^{133}Xe.

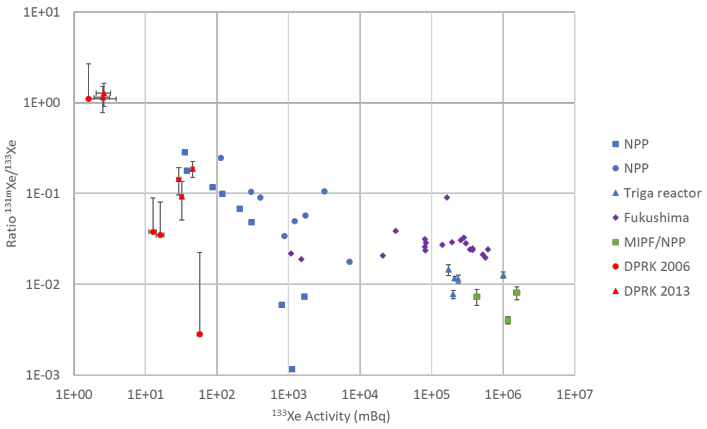

Figure 2.11: Isotopic ratio plot of a variety of radioxenon sources using only two isotopes for the ratio analysis, where NPP stands for nuclear power plant.

2.5 Current Limitations of Radioxenon Detection

The goal of radioxenon detectors is to detect and quantify the isotopes of interest with high certainty. These detections are then used to discriminate between the various radioxenon sources using isotopic ratios. Over the years, the current radioxenon detectors, plastic and NaI(Tl), has exhibited properties that make this analysis challenging. This section describes the limitations of memory effect and isotopic interference on radioxenon detection.

2.5.1 Memory Effect

Memory effect occurs when radioxenon activity remains in the cell even after the cell has been evacuated and flushed, thus being detected in subsequent measurements. The memory effect is caused by the diffusion of radioxenon into the plastic scintillator. It was estimated that 3-4% of the sample remains in the cell and increases the background in subsequent measurements, which in turn raises the detection limit [107]. As an example, the typical MDC level of the SAUNA II system is 0.1-0.2 mBq/m^3 but when a high activity sample such as 300 mBq/m^3 is measured this raises the MDC level of the subsequent measurement to 0.4 mBq/m^3 [107]. One method of decreasing the memory effect is to coat the plastic cell with a material that prohibits the diffusion of xenon and was tested using a variety of materials as discussed in Seifert [108] and Blackberg [50, 107]. While

coating the cell can decrease the memory effect it can also decrease the efficiency of the cell due to attenuation of low energy electrons and photons. Identifying materials where the memory effect is significantly decreased, such as stilbene and silicon, is an alternative approach and is discussed in previous sections.

Of the surface coatings, the use of an Al_2O_3 surface coating with a thickness of 425 nanometers had the best performance, reducing the memory effect by a factor of 100 compared to the control [107]. In Blackberg [50], results from the measurement of a coated cell show that the memory effect is about a factor of 1000 lower than that measured in uncoated detectors. The measurement also showed that the coating did not significantly impair the electron efficiency or the energy resolution. Although, after about 6 months some degradation of the cell was observed [50], this coating has been implemented in field SAUNA systems [109].

In order to account for the memory effect, background measurements known as gas backgrounds, are taken in between sample measurements. These gas background measurements are used to quantify the memory effect present in the cell and subtract it from the subsequent measurements. Although, this method has proven to be sufficient in analysis techniques, the presence of additional background decreases the sensitivity of the detection system and increases measurement uncertainties. If the memory effect is high, subsequent measurements will be void since no counts would be detected above the memory effect. Additionally, the need to take additional gas background measurements, reduces the time the detection system has to measure radioxenon samples. Therefore, the use of plastic as the sample container and beta detector can limit the effectiveness of the detection system because of memory effect.

2.5.2 Isotopic Interference

There are two main types of isotopic interference that occur in radioxenon measurements: radon and inter-isotopic interference, primarily ^{133}Xe. Radon is present in the background as a decay product of uranium. The decay scheme of ^{222}Rn with associated half-lives and relevant particle

emissions is shown in Figure 2.12. The emissions of radon overlap with all radioxenon ROIs, thus contaminating radioxenon samples.

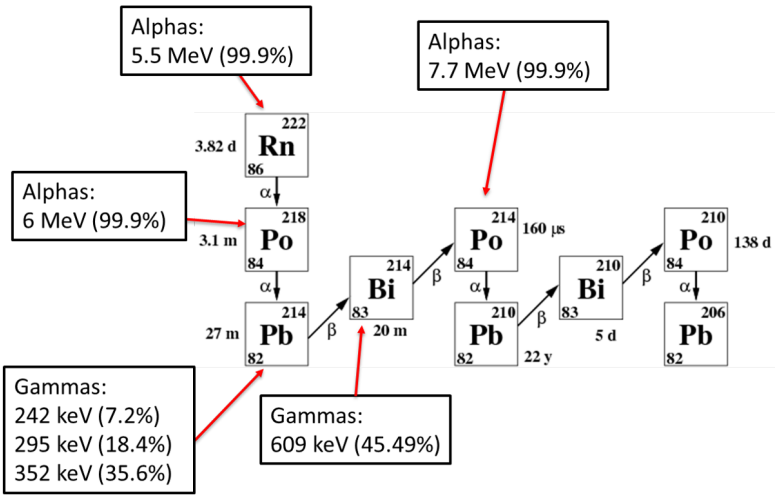

Figure 2.12: Radon decay chain with particle emission types and energies relevant to radioxenon detection, modified from *A Radon Progeny Deposition Model* [110].

The non-metastable isotopes, ^{135}Xe and ^{133}Xe, have more complex decay schemes than the metastable isotopes. Additionally, the energy levels of the non-metastable isotopes are higher, emitting higher energy particles than the metastable isotopes. Therefore, isotopic interference occurs from high energy to low energy for the radioxenon isotopes, where each isotope of interest interferes in some way. As mentioned previously, aside from its primary coincidence emission,^{135}Xe decay emits other particles in coincidence. As shown in Figure 2.13, ^{135}Xe interferes with all the ROIs below it.

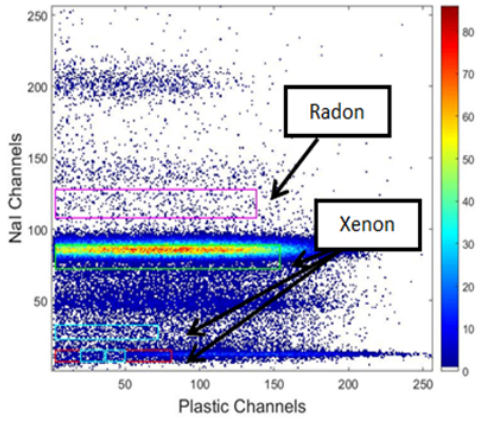

Figure 2.13: Coincidence spectrum of ^{135}Xe measurement showing the isotopic interference of this isotope on the other ROIs, particularly the 30 keV ROI.

The second inter-isotopic interference, ^{133}Xe, is due to the common characteristic X-rays that are emitted in the 30 keV region. As shown in Figure 2.6, the ROIs of the metastable isotopes, ^{131m}Xe and ^{133m}Xe, are encompassed in the 30 keV ROI for ^{133}Xe. Therefore, whenever a metastable isotope is present in a sample containing ^{133}Xe, the counts in the metastable ROI have to be characterized for each isotopes decay. And as mentioned previously, many of the civilian sources of radioxenon emit ^{133}Xe causing it to be commonly measured at IMS stations, thus interfering with the detection of the metastable isotopes. This interference with metastable isotope detection makes the use of isotopic ratios challenging. Additionally, the metastable isotopes can interfere with one another if their CE emissions overlap, due to the beta detector resolution.

Over the last couple of years, multiple declared nuclear weapons tests by the DPRK have illustrated that, although the IMS is capable of monitoring nuclear explosions, when the isotopes are well contained it is difficult to say with high confidence that an explosion was nuclear in nature. An example of this issue is shown in Figure 2.14. Measurements of ^{133}Xe occurred at stations near the DPRK around the time of the declared nuclear test in 2016 [111]. However, due to the low activity of ^{133}Xe present in the sample, it was difficult to quantify the metastable isotopes that could be used in isotopic ratio analysis. Therefore, the development of radioxenon detectors is ongoing.

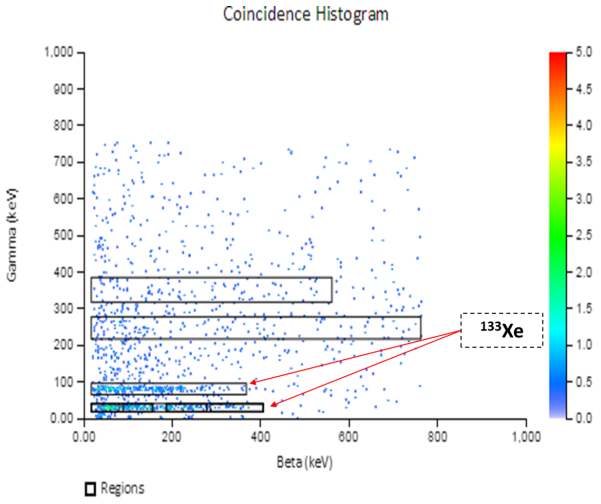

Figure 2.14: Radioxenon measurement at IMS station JPX38, February 2016.

Chapter 3

Radioxenon Analysis Methods

3.1 Motivation

The quantification method of radioxenon isotopes is equally important to the detection mechanisms because of isotopic ratio analysis. Radioxenon detectors undergo thorough calibration to establish the ROIs and coincidence efficiencies. This information is vital to the characterization of the coincidence system, and its use in forensic analysis. The net coincidence count method, referred to as the traditional method, has been used to identify various sources of radioxenon, as discussed in the previous chapter. However, due to prevalent ^{133}Xe measurements, the current technique is sometimes difficult to use when quantifying metastable isotopes because of the overlapping ROIs.

This following section summarizes the traditional method used to calibrate radioxenon detectors and analyze samples. Section 3.3 describes an alternative analysis technique to quantify metastable isotopes, focusing on ^{131m}Xe.

3.2 Traditional Method

A full calibration of the plastic and NaI(Tl) coincidence system typically involves the measurement of background, ^{137}Cs, the four radioxenon isotopes, and radon. The X-ray and gamma ray peaks are used to calibrate the NaI(Tl) detector and the CE and beta endpoint energies are used to calibrate the plastic cell. The resolution of the various peaks is also measured to produce energy resolution curves for the detectors. With this information, the ROI bounds are set with the width for the photon

and CE peaks typically being twice the full width at half maximum (FWHM). Each isotope of interest and radon has an ROI based on its emission energies. An example of the ROI locations in a coincidence spectrum is shown in Figure 3.1.

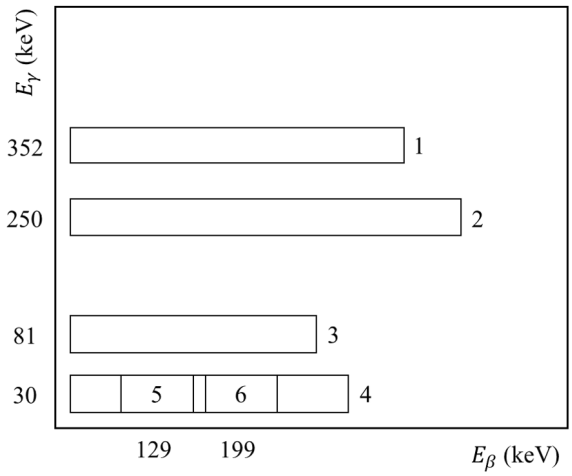

Figure 3.1: Coincidence histogram example of ROI locations with each ROI numbered for the traditional analysis method.

With the ROI bounds set, the efficiency of the detectors can be calculated. The efficiency calculation is typically done using the absolute efficiency calibration method [112, 113]. This method allows for the efficiency to be calculated without knowledge of the sample's activity. The activity calculation, not accounting for collection and processing time, is shown in Equation 3.1,

$$A = \frac{\lambda C}{BR * \varepsilon * (1 - e^{-\lambda T})} \tag{3.1}$$

where A is the activity in Becquerels, C is the net counts in the ROI, λ is the decay constant of the isotope, BR is the branching ratio, ε is the total efficiency of the detector, and T is the acquisition time of the measurement. In this form, the activity can be calculated by gamma emissions, beta emissions, or coincidence emissions, and thus these activity equations can be simplified, set equal to one another, and solved for the efficiency of interest. A generalized case is shown in Equations 3.2, 3.3, and 3.4

$$A = \frac{C_\beta}{\varepsilon_\beta BR_\beta} = \frac{C_\gamma}{\varepsilon_\gamma BR_\gamma} = \frac{C_{\beta\gamma}}{\varepsilon_{\beta\gamma} BR_{\beta\gamma}} \tag{3.2}$$

$$\varepsilon_\beta = \frac{C_{\beta\gamma}}{C_\gamma BR_\beta} \tag{3.3}$$

$$\varepsilon_\gamma = \frac{C_{\beta\gamma}}{C_\beta BR_\gamma} \tag{3.4}$$

where the β subscript represents betas, the γ subscript represents gammas, and the $\beta\gamma$ subscript represents coincidence events. This analysis is done for each ROI and varies in complexity due to the branching ratios of the emissions.

Additionally, the interference ratios are calculated after the ROI bounds are established. For each calibration isotope measured, the interference ratio is calculated as

$$R_{i:j} = \frac{C_i}{C_j} \tag{3.5}$$

where $R_{i:j}$ is the ratio of counts from ROI j that interfere with ROI i, C_i is the counts in ROI i of the sample, C_j is the counts in ROI j of the sample. The interference ratios are calculated in order of high gamma energy to low gamma energy since low energy emissions do not contribute to the higher energy ROIs. As an example, Figure 3.2 shows a coincidence spectrum of a sample containing ^{133}Xe and ^{131m}Xe. In order to account for the isotopic interference in the metastable ROI, the ratio of ROI 3 to ROI 5 is calculated for the ^{133}Xe calibration sample. Then, for subsequent measurements, the counts in ROI 3 are calculated and then multiplied by the interference ratio to account for the counts from ^{133}Xe that are in ROI 5. These counts are then subtracted from the counts in ROI 5 to account for the isotopic interference.

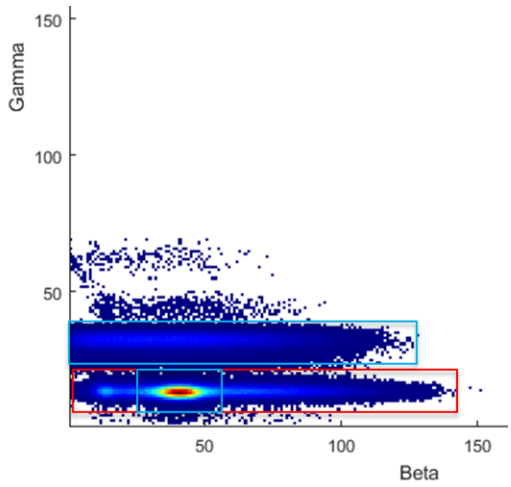

Figure 3.2: Mixed ^{133}Xe and ^{131m}Xe sample showing the isotopic interference that occurs for the metastable isotope.

The MDC is based on the detector background and isotopic interferences and is calculated by

$$MDC(\frac{mBq}{m^3 air}) = \frac{2.71 + 4.65\sigma_0}{\varepsilon_\gamma \varepsilon_\beta \gamma_{BR} \beta_{BR}} \frac{\lambda^2}{(1 - exp(-\lambda T_C))exp(-\lambda T_P)(1 - exp(-\lambda T_A))} \frac{T_C * 1000}{V_{air}} \quad (3.6)$$

$$\sigma_0 = \sqrt{(\sigma_B)^2 + \Sigma(\sigma_{I_j})^2 + (\sigma_G)^2} \quad (3.7)$$

where ε_γ is the gamma efficiency, ε_β is the beta efficiency, γ_{BR} is the gamma branching ratio, β_{BR} is the beta branching ratio, λ is the decay constant, T_C is the xenon collection time, T_P is the processing time of the gas, T_A is the acquisition time of the counts, V_{air} is the sampled air volume, σ_B is calculated from the background count error, σ_{I_j} is calculated from the isotopic interference error, and σ_G is calculated from the gas background count error. The MDC characterizes the sensitivity of the detector, giving the concentration limit above which, the sample can be declared as having activity. Therefore, the MDC also increases significantly for the metastable isotopes when ^{133}Xe is

present in the sample.

With the ROI bounds set through energy calibration and resolution analysis, calculation of detector efficiency, interference ratios, and MDC, the detector is fully characterized. Next, the activity can now be calculated using equation 3.1. The counts, C, that are attributed for each isotopes ROIs must be corrected for isotopic interference, memory effect, and background:

$$C_i = M - C_B - C_G - \sum(C_j * R_{i:j}) \tag{3.8}$$

where C_i is the counts in ROI i, M is the measured counts in ROI i, C_B is the background counts in ROI i, and C_G is the gas background counts in ROI i. The gas background counts, C_G, are corrected by a factor F that accounts for the time that has elapsed between the measurements:

$$F = \frac{t^G_{real}}{t^G_{live}} \frac{t^S_{real}}{t^S_{live}} e^{-\lambda\tau}(1 - e^{-\lambda t^S_{real}})/(1 - e^{-\lambda t^G_{real}}) \tag{3.9}$$

where the superscripts G and S represent the gas background and sample, respectively, t_{live} is the live time, t_{real} is the real time, and λ again is the decay constant of the isotope.

As an example, the net counts for the ^{131m}Xe, ROI 5, shown in Figure 3.2 is calculated as

$$net\ C_5 = C_5 - C_{B_5} - (F * C_{G_5}) - (C_1 * R_{5:1}) - (C_2 * R_{5:2}) - (C_3 * R_{5:3}) \tag{3.10}$$

where C_5 is the counts in ROI 5 of the sample measurement, C_{B_5} is the counts in ROI 5 of the detector background, $(F * C_{G_5})$ is the decay corrected counts in ROI 5 of the gas background, $(C_1 * R_{5:1})$ is the counts in ROI 5 due to radon, $(C_2 * R_{5:2})$ is the counts in ROI 5 due to ^{135}Xe interference, and $(C_3 * R_{5:3})$ is the counts in ROI 5 due to ^{133}Xe. More detailed descriptions of the

traditional method are found in [114–116].

3.3 Anticoincidence Method

As previously mentioned, the interference of ^{133}Xe with the metastable isotopes, increases the MDC making it difficult for the metastable isotopes to be identified. To mitigate this issue, an alternative method has been identified as a way to quantify the metastable isotopes in the presence of ^{133}Xe using an anticoincidence beta spectrum [117, 118]. This method still employs the use of a beta-gamma coincidence detector; however, the anticoincidence spectrum consists of events that only occurred in the beta detector, using the gamma detector as a veto to reject other events. Therefore, a simple way of extracting the anticoincidence spectrum is to subtract beta coincidence events from the beta singles spectrum.

3.3.1 Methodology

The metastable radioxenon isotopes decay through internal conversion, and the conversion electrons (CE) emitted in the process have energies corresponding to the electron shell emissions. Due to the energy threshold of the plastic scintillator beta detector, coincidence decays above the K-shell, emit particles undetectable by the coincidence detector setup [47, 52]. Therefore, CE emissions with a corresponding undetectable coincidence decay qualify as anticoincidence events since only the beta detector is triggered. In addition, the coincidence decay of the K-shell electron can sometimes classify as anticoincidence when the corresponding x-ray is not detected by the gamma ray detector. The branching ratios of the most probable decay events for ^{131m}Xe are shown in Table 3.1 with their classification as an anticoincidence event. Anticoincidence events accounts for approximately 60% of the beta detector response.

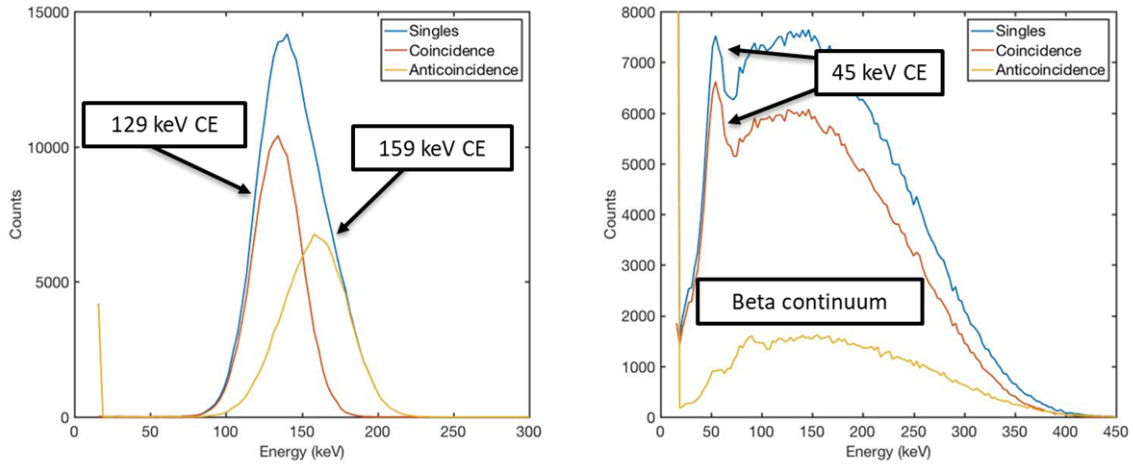

(a) (b)

Figure 3.3: Beta spectra for ^{131m}Xe and ^{133}Xe showing the contributions of coincidence and anticoincidence events to the beta singles spectrum.

Table 3.1: Key branching ratios of ^{131m}Xe [119]

Emission	Branching Ratio	Anticoincidence Event
Gamma-ray (163 keV)	1.95%	No
CE K (129 keV) + x-ray K (30 keV)	54.7%	Sometimes
CE K (1249 keV) + Auger K (24 keV)	6.88%	Yes
CE L (158 keV)	28.8%	Yes
CE M (162 keV)	6.59%	Yes
CE N (163 keV)	0.15%	Yes

Figure 3.3 shows the contributions of coincidence and anticoincidence events to the simulated beta singles spectrum for ^{131m}Xe and ^{133}Xe. For ^{131m}Xe, Figure 3.3a, the coincidence events are centered around 129 keV whereas the anticoincidence events are centered around 159 keV which is expected based on the decay scheme. For ^{133}Xe, Figure 3.3b, the anticoincidence event contribution is small, due to ^{133}Xe emitting a beta with every decay. Therefore, the interference from ^{133}Xe is minimized in the anticoincidence spectrum compared to the coincidence spectrum as shown in Figure 3.4.

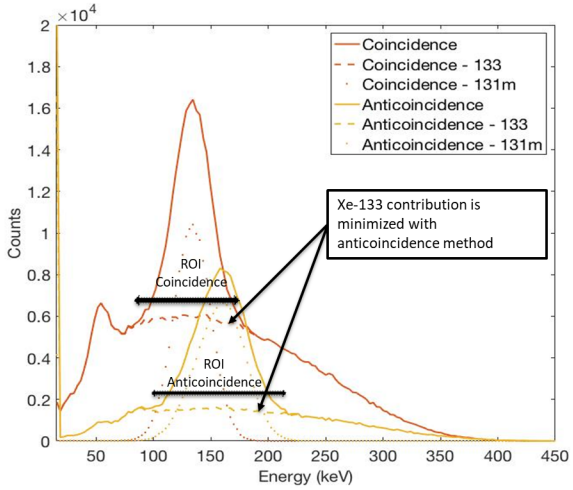

Figure 3.4: Beta spectra of simulated mixed sample of ^{131m}Xe and ^{133}Xe with the isotopic contributions to the spectrum shown.

The net counts for ^{131m}Xe are calculated as shown in Equation 3.10. The interference ratio is calculated in a manner similar to that for the traditional method described above. Once the ROI is chosen using the ^{133}Xe calibration source, the counts in what is traditionally known as ROI_3, or the 2-D 80 keV region, are used to calculate the interference ratio as shown in Equation 3.11,

$$R = \frac{ROI_{Acoin}}{ROI_3} \tag{3.11}$$

where R now represents the interference ratio. The branching ratio and efficiency are also with respect to the anticoincidence ROI. In order to solve for the activity using the anticoincidence method (ACM), the efficiency and branching ratio of each decay that contributes to the spectrum has to be accounted for. The calculation for ^{131m}Xe is shown in Equation 3.12,

$$BR*\varepsilon = [BR_{124+30}*\varepsilon_{129}*(1-\varepsilon_{30})]+[BR_{129+24}*(1-(1-\varepsilon_{24})(1-\varepsilon_{129}))]+BR_{158}+BR_{162}+BR_{163} \tag{3.12}$$

where the subscript values refer to the energies of the electron or x-ray (with plus signs indicating coincidence), the efficiency values are calculated during the calibration of the detector, and it is assumed that the efficiency of the plastic detector for energies greater than 124 is approximately 1.0. The net counts, C, is used in Equation 3.1 to calculate the activity, and the uncertainty in Equation 3.1 is calculated in Equation 3.13,

$$\sigma_A = \sqrt{A^2 \left[\left(\frac{\sigma_C}{C} \right)^2 + \left(\frac{\sigma_{BR*\varepsilon}}{BR * \varepsilon} \right)^2 \right]} \tag{3.13}$$

where σ_C and $\sigma_{BR*\varepsilon}$ are calculated through error propagation of Equations 3.10 and 3.12 respectively. Similar to the MDC but simplified, the MDA is calculated using the Currie equation for 95% uncertainty,

$$MDA = \frac{\lambda(4.65\sigma_0 + 2.71)}{BR * \varepsilon * (1 - e^{-\lambda T})} \tag{3.14}$$

$$\sigma_0 = \sqrt{(\sigma_{bkgd})^2 + (\sigma_{1_{int}})^2 + (\sigma_{2_{int}})^2 + (\sigma_{3_{int}})^2} \tag{3.15}$$

where σ_{bkgd} is calculated from the error in counts of the background, $\sigma_{1_{int}}$ is calculated from the error in the interference counts due to radon, $\sigma_{2_{int}}$ is calculated from the error in the interference counts due to ^{135}Xe, and $\sigma_{3_{int}}$ is calculated from the error in the interference counts due to ^{133}Xe for ^{131m}Xe [115, 120]. For the data analyzed in this work, $\sigma_{1_{int}}$ and $\sigma_{2_{int}}$ are close to zero because radon and ^{135}Xe are not present in the samples.

Ideally, the ROI would be chosen for a specific range of decays as discussed. Alternatively, the calibration sample can be used to calculate the branching ratio and efficiency of various anticoincidence ROIs, assuming the activity is known or can be calculated [112]. This is shown in Equation 3.16,

$$U = BR * \varepsilon = \frac{M}{N} \tag{3.16}$$

where M is the number of counts in the ROI, N is the total number of counts emitted by the source, and U now takes the place of the branching ratio and efficiency of the ROI in Equation 3.17. Equation 3.16 eliminates the need to determine branching ratios and efficiencies for each decay line and also allows multiple ROI bounds to be tested.

This method also allows for optimization of the anticoincidence ROI. To optimize the ROI, the interference ratio should be minimized while maximizing the detection of the isotope (maximizing the branching ratio and efficiency). A figure of merit (FOM) was established and is calculated as shown in Equation 3.17,

$$FOM = \frac{BR * \varepsilon}{R} \tag{3.17}$$

with the most optimal ROI having the highest FOM. Figure 3.5 shows an example of the ROI optimization, where ROI 1 encompasses both CE emissions and ROI 2 focuses on the 158-keV through 163-keV CE emissions. Although the FOM of ROI 1 is higher, this analysis shows that for some detection systems, ROI 2 may be higher if the efficiency for this region was increased given their close FOM values. Therefore, the results presented in the following sections use the calibration sample method and optimization of the ROI using Equation 3.17.

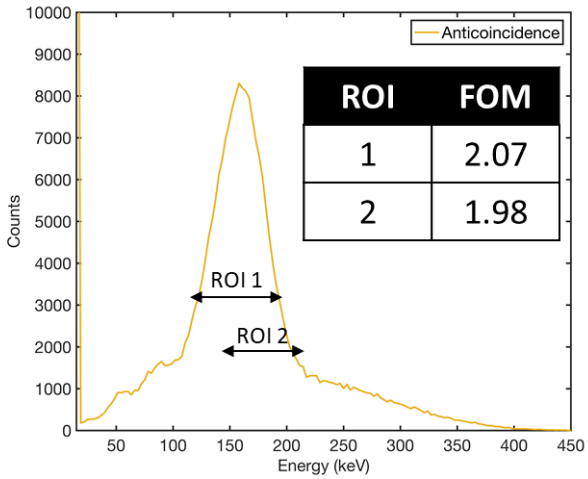

Figure 3.5: An example of ROI bound optimization for the ACM where ROI 1 has a higher FOM than ROI 2.

3.3.2 Mixed Sample Experimental Results

To check the analysis techniques and accuracy of the ACM, a control experiment was conducted. A mixed sample containing approximately 150 Bq of ^{133}Xe and less than 10 Bq of ^{131m}Xe was injected into a beta-gamma coincidence detector using plastic and NaI(Tl) and counted for 50 days. As shown in Figure 3.6, as ^{133}Xe decays, the CE from ^{131m}Xe become more apparent. Thus, the interference from ^{133}Xe is decreasing making it easier to identify ^{131m}Xe present in the sample.

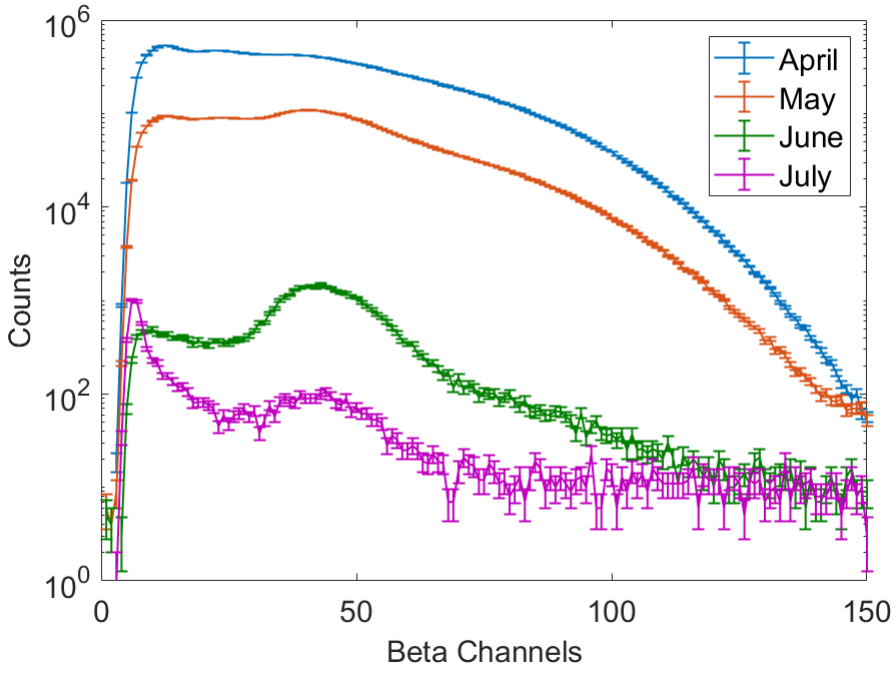

Figure 3.6: Beta spectrum of mixed ^{133}Xe and ^{131m}Xe sample over the course of the experimental period. Over time the CE peaks from ^{131m}Xe become more apparent as ^{133}Xe decays.

The counts from the measurement were recorded in 1-hour intervals to examine the activity change over time during the measurement. In this manner, the activity and MDA calculation of the traditional method and ACM can be compared. A program developed by PNNL, calcMain, was used to calculate the activity and MDA for the traditional analysis[1]. A Matlab script was used to calculate the activity and MDA for the ACM. The results of this analysis are shown in Figure 3.7. The blue line in the plot represents the estimated true activity of ^{131m}Xe in the mixed sample. The activity calculations are represented by red and green dots for the traditional method and ACM respectively. The same colors are also used for the MDA calculations. This plot shows that the ACM, correctly quantifies the ^{131m}Xe sooner (approximately hour 400) than the traditional method (approximately hour 500). Additionally, throughout the experiment, the MDA of the ACM is lower than the traditional method, signifying that the ACM is more sensitive to ^{131m}Xe for this sample.

[1]This program calculates concentrations and thus these values were converted to activity assuming a gas volume 12-15 m^3, thus dividing the value by (1000/(1.3/0.087)).

As the ^{133}Xe interference decreases, the MDAs of the two methods eventually converge further illustrating the effect of ^{133}Xe interference in identifying ^{131m}Xe. However, the ACM needed to be tested at various mixed sample ratios to understand where this method could best be applied.

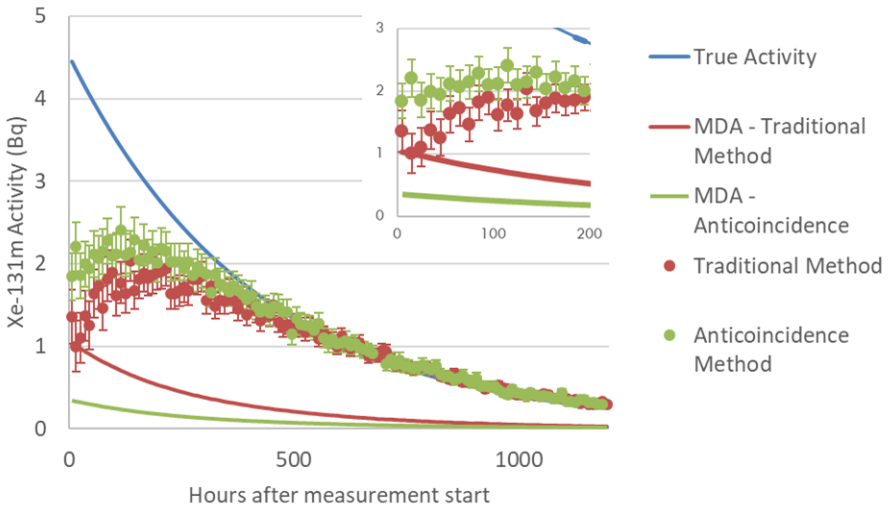

Figure 3.7: Activity calculation comparison of ^{131m}Xe in a mixed sample of ^{131m}Xe and ^{133}Xe at various increments over the 50-day experimental period. This figure shows that the MDA for the anticoincidence method is lower and that the anticoincidence method calculates the correct activity sooner than the traditional method.

3.3.3 Simulation Results

As an additional check to analyze the benefits of the ACM, the spectrum simulation tool discussed in Deshmukh 2017 was used [37, 121]. Various ratios of ^{133}Xe and ^{131m}Xe were simulated with and without detector background (~0.01 coincidence counts per second). Additionally, to simplify the error calculation, 100 files of each ratio were simulated, and the average activity and MDA were determined. The standard deviation of the average activity is presented as the uncertainty for the activity calculation. The results are presented as either constant ^{133}Xe activity, resulting in a steady MDA, or constant ^{131m}Xe activity where the MDA fluctuates due to the ^{133}Xeinterference.

Three levels of ^{133}Xe interference were simulated: 8, 30, and 150 mBq. Figure 3.8 shows the simulated 2-D spectra for each of the ^{133}Xe activities having equal amount of ^{131m}Xe (3.4 mBq) with no background. The three levels of ^{133}Xe interference will be referred to as low, medium, and

high for 8, 30, and 150 mBq respectively. Bar graphs with error bars are presented for the activity calculation results separated by simulations with and without background counts. The average MDA for each ratio overlays the activity bar graph such that lines above the solid color bar graphs indicate the MDA being higher than the calculated activity.

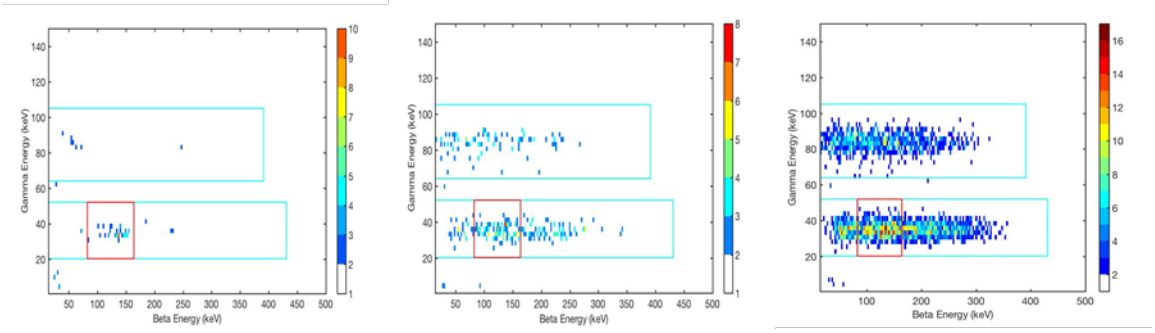

Figure 3.8: Simulated coincidence spectra of 3.4 mBq of ^{131m}Xe and 8.0 (left), 30.0 (middle), 150.0 (right) mBq of ^{133}Xe showing the various interference levels.

Figure 3.9 shows the results of the ^{131m}Xe activity calculations compared to the simulated ^{131m}Xe activity with low ^{133}Xe interference and no background. In this case, the MDA of the coincidence method is higher than the anticoincidence MDA due to interference counts. The ratios of 0.09 and 0.18 are below the MDA for the coincidence method, while only 0.09 is below the MDA for the ACM. Overall, the two methods calculate the true activity within uncertainty bars, although the ACM is more accurate. These results show that the analysis methods are working as intended.

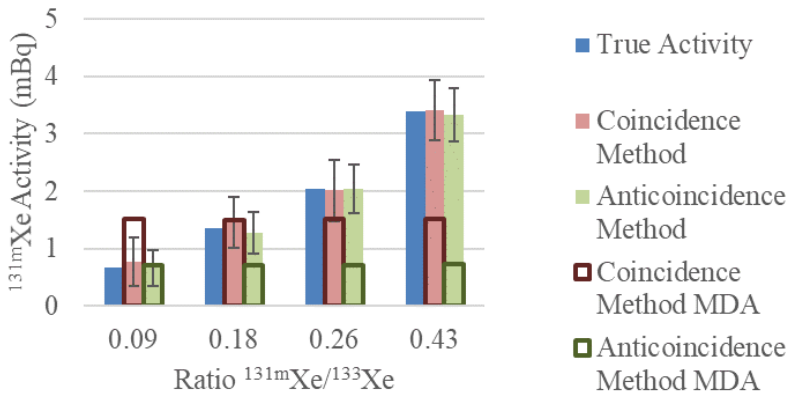

Figure 3.9: Activity calculation comparison of ^{131m}Xe with 8.0 mBq ^{133}Xe interference without background (idealized case) showing the ability of both methods to calculate the simulated activity within error bars.

Figure 3.10 shows the activity calculation comparison of the three levels of interference with background counts included in the simulations. In the case of low interference, the MDA of the ACM is a lot higher than the coincidence method due to the number of background counts that contribute to the anticoincidence spectrum. Additionally, the statistics of the ^{133}Xe contribution are poor, resulting in larger fluctuations in the activity calculations for both analysis methods. However, excluding the MDA limitations, the activity calculations agree. In the case of medium interference, a similar trend is observed for the MDA although the effect is smaller. The activity analyses agree within uncertainty bars, although there are slight differences, which could affect isotopic ratio analysis. In the case of high interference, the MDA for the ACM is lower than the coincidence method, due to interference counts dominating over background counts. Both methods calculate the activity within uncertainty bars with the coincidence method tending to overestimate, while the ACM underestimates the simulated activity.

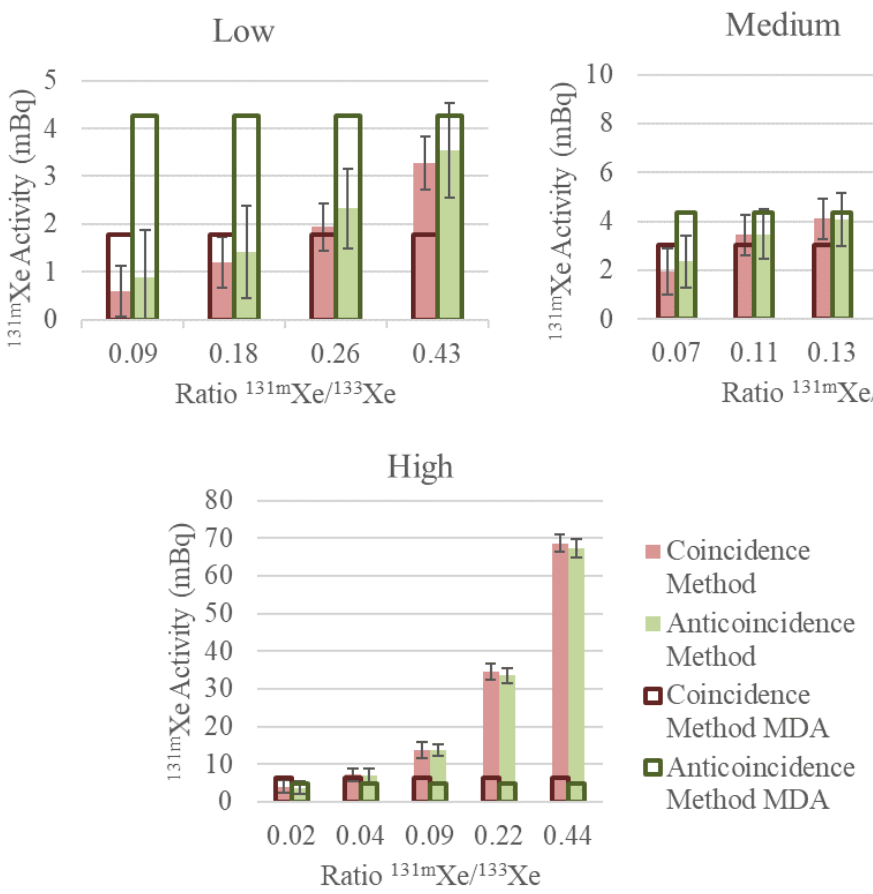

Figure 3.10: Activity calculation comparison of ^{131m}Xe with low (8.0 mBq), medium (30.0 mBq), and high (150.0 mBq) levels of ^{133}Xe interference with background simulations showing that background greatly affects the MDA of the ACM. .

Figure 3.11 shows the results of the ^{131m}Xe activity calculations with constant activity (14 mBq) and varying ^{133}Xe activities. The MDA for the two methods changes with activity ratio as expected and the coincidence method MDA decreases at a higher rate than the ACM as ^{131m}Xe activity increases. Again, both methods calculate the true activity within uncertainty bars.

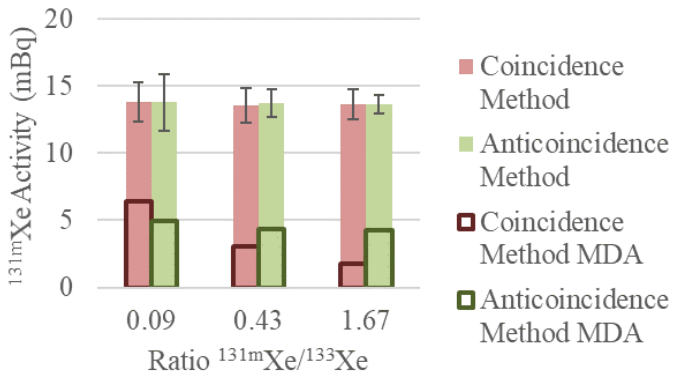

Figure 3.11: Constant ^{131m}Xe activity calculation (14 mBq) comparison with varying ^{133}Xe interference and background showing the faster decrease of the MDA for the coincidence method.

3.3.4 In-Field Experimental Results

To further test the ACM, a series of measurements from a radioxenon system were analyzed. The measurements were performed over a few months and used the standard plastic and NaI(Tl) coincidence scintillation detector set-up. This dataset included the use of gas background measurements further complicating the analysis by requiring the subtraction of interference counts due to the gas background in addition to interference from ^{133}Xe. Calibration data were used to calculate and optimize the ROI bounds. Figure 3.12 left shows the comparison of activity calculations for the two methods along with the corresponding MDA calculations. For many of the activity calculations the analysis methods agree within error bars. Because the MDA is due to the detector background and ^{133}Xe interference, when the activity of ^{133}Xe dominates (or is relatively high) the ACM has a lower MDA. As the ^{133}Xe activity increases, the MDA of the coincidence method increases at a faster rate than the ACM. Therefore, as the ^{133}Xe interference increases, the ACM method becomes more sensitive to ^{131m}Xe, resulting in more activity calculations of ^{131m}Xe above the MDA for the ACM as compared to the coincidence method as shown in Figure 3.12 right. The activity calculation results and the MDA effects on the isotopic ratios are discussed in the next section.

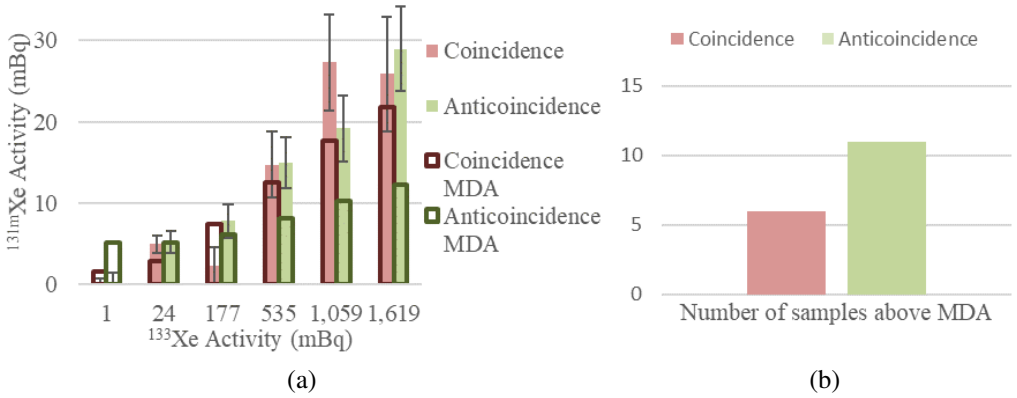

Figure 3.12: Activity calculation comparison of ^{131m}Xe for a selection of measurements showing that at high levels of ^{133}Xe interference the ACM is more sensitive to ^{131m}Xe (a) and number of samples above MDA for coincidence and anticoincidence method (b).

As discussed previously, isotopic ratios are used to distinguish the sources of radioxenon. However, it is important to include the detector limitations in these isotopic ratio plots. Figure 2.11 shows the limited range of the isotopic ratios and the importance of being able to quantify isotopes individually. Figure 3.13 shows the ratios of the activity calculations and the MDA for both methods. The ACM has more activity calculations above the MDA (11) than the coincidence method (6) due to increased sensitivity when high levels of ^{133}Xe are present. Therefore, an increase in statistically significant isotopic ratios could lead to improved source discrimination.

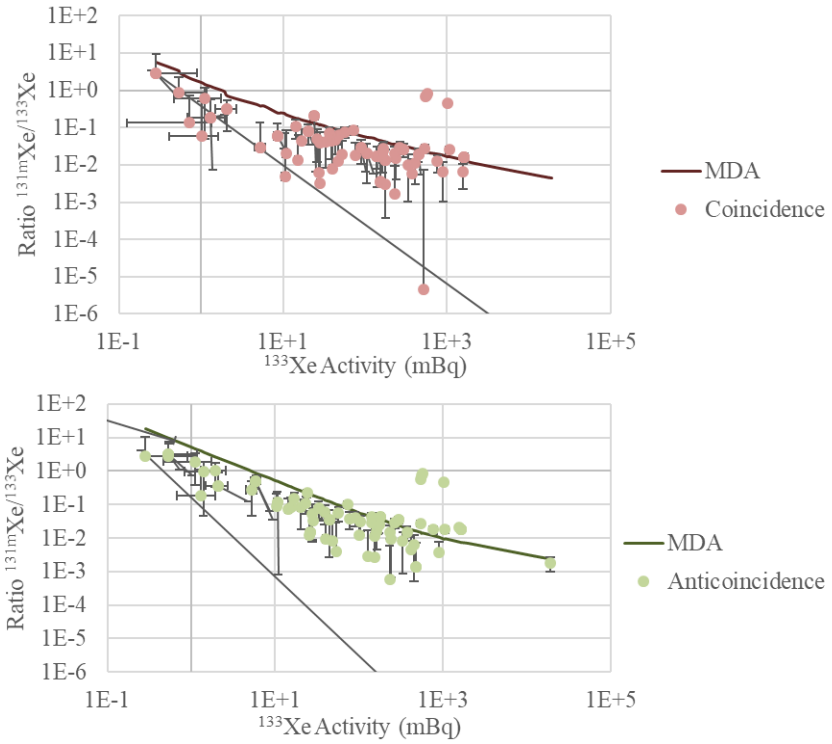

Figure 3.13: Ratio versus ^{133}Xe with MDA curve for the coincidence method (top) and the ACM (bottom) showing that the ACM method has more activity calculations above the MDA.

3.4 Conclusions

The ACM has been shown to improve activity calculations compared to the coincidence method when there is ^{133}Xe interference. The ACM is more sensitive than the coincidence method as the detector background is reduced. However, in the cases where realistic background is included in the simulation, the MDA of the coincidence method is much lower when the activity of ^{133}Xe is low (less than ~30 mBq). When the interference of ^{133}Xe is high (greater than ~150 mBq, dependent on detector background), the ACM outperforms the coincidence method in MDA and activity calculation. This result suggests that the ACM would be suited for measurements with a medium to high ^{133}Xe interference. In the cases where the detector background of the beta detector is high (greater than 0.01 coincidence counts per second), the activity calculation of ^{131m}Xe using the ACM will be accurate but a decision will have to be made of whether to use the value if it is below the MDA of the anticoincidence ROI. Additionally, methods to decrease the beta detector background

would improve the MDA of the ACM. Future work will include optimizing the anticoincidence ROI to minimize the MDA and applying the anticoincidence method to the other important metastable isotope ^{133m}Xe .

Chapter 4

MCNPX-PoliMi Modeling and Code Development

4.1 Motivation

The development of radioxenon detectors is vital to the verification of the CTBT. As previously discussed, the need for detectors with better resolution and sensitivity has increased. However, the use of materials such as silicon and stilbene can be expensive to test and manipulate, requiring the use of simulations. Additionally, it is difficult to produce a variety of mixed samples in a laboratory environment to analyze detector response. Programs such as BGSim [37] have been produced to help simulate detector response, but lack the flexibility to modify the materials used to detect the radiation. Previously developed alternative tools using Geant4 or MCNP are discussed in [122–124]. The MCNP method in [122] was limited by the inability of the code to correlate the emissions of the various isotopes, requiring individual simulations for each major decay. The Geant4 methods discussed in [123, 124] show good agreement between simulation and experiment, but require knowledge of the source code [123] and understanding of the Geant4 libraries.

MCNPX-PoliMi was developed to simulate correlated particle emissions [125]. It produces a collision file listing information about each particle history, such as the detector of interaction, energy deposited, and particle type, allowing for flexible tally options. The events written to the output file are determined by specifying the detectors of interest and the minimum number of detectors in which energy is deposited. This output file structure allows for singles or coincidence-only events to be collected and results in quick identification of coincidence events versus using

a coincidence timing window as discussed in [123, 124]. Because MCNP does not simulate optical photons, spectrum broadening is also included in the post-processing used to construct the histograms, by sampling a resolution curve. This flexible approach permits a more direct generation of 2-D histograms, compared to Geant4 or MCNP6. A new built-in source, the Single Decay Option, was developed to specifically simulate radioxenon decay, which the code was not able to do previously. The use of MCNPX-PoliMi, in conjunction with user-defined algorithms for detector response simulation, allows for the simulation of any detector type and geometry.

4.2 Simulation Model

The detectors used for this study are assumed to be a rounded plastic beta cell and a well-type NaI(Tl) detector, because detailed schematics of the detectors were not given. The activity of each sample was estimated from the measurements using traditional methods and the simulation was based on the activity estimation. From the measurement data, the energy calibration and resolution curve were determined and used for validation. The geometry of the detectors modeled in MCNPX-PoliMi is shown in Figure 4.1. The PMTs of the detectors and the aluminum casing of the NaI(Tl) were modeled to get a more accurate detector response due to additional scatters.

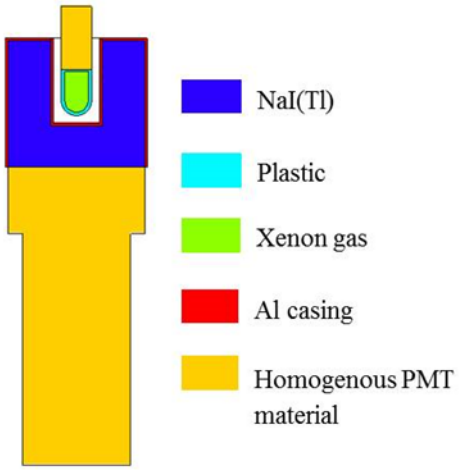

Figure 4.1: MCNPX-PoliMi model of plastic and NaI(Tl) detector.

The individual detector spectra are histograms of the energy deposited in either the NaI(Tl) or plastic scintillator, not accounting for interactions in the other detector. The coincidence spectra are a result of energy deposition in both the NaI(Tl) and plastic scintillator within a specified time window for the experiment or within a history for the simulation. The coincidence histogram shows energy deposited in the plastic scintillator detector on the x-axis and energy deposited in the NaI(Tl) detector on the y-axis. This approach results in a 2-D histogram, where the color bar illustrates the number of counts in each bin. The most probable coincidence photon energies for each isotope are given in Table 4.1.

Table 4.1: Radioxenon Isotopes of Interest Coincidence Energies [119]

Isotope	Electron Energy (MeV)	Photon Energy (MeV)
^{135}Xe	0.915 (endpoint)	0.250
^{133}Xe	0.346 (endpoint)	0.030 - 0.035 and 0.081
^{131m}Xe	0.129	0.029 - 0.034
^{133m}Xe	0.199	0.029 - 0.034

4.3 Summary of Changes for Versions 2.1.0-2.1.4

In order to simulate a coincidence decay, the Single Decay Source was used. This mode simulates correlated particles from radioactive decay. Using this source requires a few additional files and allows the user to select a parent and daughter nuclide pair to decay. Specifically, the parent and daughter isotopes are listed on the IPOL card in order for the correlated decay to be simulated. Examples of parent and daughter decays from the decay.dat file is shown in Figure 4.2.

```
13154    13154
131XE    131XE IT DECAY
  163.93
```

```
13555    13554
135CS    135XE B- DECAY (9.14 H)
  249.79 9.600E+01    910.0   0
  407.99 5.900E-01   -243.0   0
  608.19 3.110E+00    550.0   0
  981.32 7.500E-02    -46.0   0
 1062.42 1.230E-01    -23.0   0
```

Figure 4.2: Examples of the decay.dat file for ^{131m}Xe and ^{135}Xe.

In order to accurately simulate detector response, electron transport is required since beta and/or conversion electrons are emitted in the decay of radioxenon. Typically, electron detection is not

used in MCNPX-PoliMi, because the electron range is much shorter than the size of the detector system. However, in the case of beta-gamma coincidence systems, the plastic is thick enough to stop and detect the electrons, which are vital to radioxenon detections. Additionally, Compton scattering of the gamma-rays on electrons is also simulated with electron transport turned on. Therefore, the tracking of electrons can lead to large output files (on the order of gigabytes), due to the sub-step approach of charged particle transport. A few alterations can be implemented to limit the size of the output file such as turning off knock-on electrons and implementing a cut card. The use of the MCNP cut card allows for the remaining energy to be deposited at that location instead of continuing to be transported.

The first test with this source was unsuccessful due to the method, in which the code handled the transport of conversion electrons as shown in Figure 4.3a. In this version, 2.1.0, the energy of the conversion electron was deposited at the source location and never transported. Thus, the simulated plastic detector never registered counts. Additionally, the electrons were depositing negative energy, which affected the total energy deposited. This issue was fixed by turning off explicit x-rays and knock-on electrons on the Phys:E card. All of the following changes to the code were implemented by Professor Enrico Padovani from Politecnico di Milano. In version 2.1.1, the number of collisions printed to the output file was extended past 100. However, CE electron transport was still not fixed in versions 2.1.1-2.1.3.

In version 2.1.4, a new version of the Single Decay Option was implemented for the four radioxenon isotopes of interest. This implementation fixed the transport of the CEs as shown in Figure 4.3b. The code was also updated with the latest branching ratios from Firestone [119]. For the metastable isotopes, a simplified source was developed, simulating only the primary emissions. Along with updates to the Single Decay Source, a debugging file was added to confirm the energy of the source particles emitted. The final step for validating the model was including the resolution of each detector. This broadening was implemented by obtaining an energy resolution curve for each individual detector and then the energy deposited was broadened using the Gaussian function in

MATLAB. The validation results of version 2.1.4 are presented in the following section.

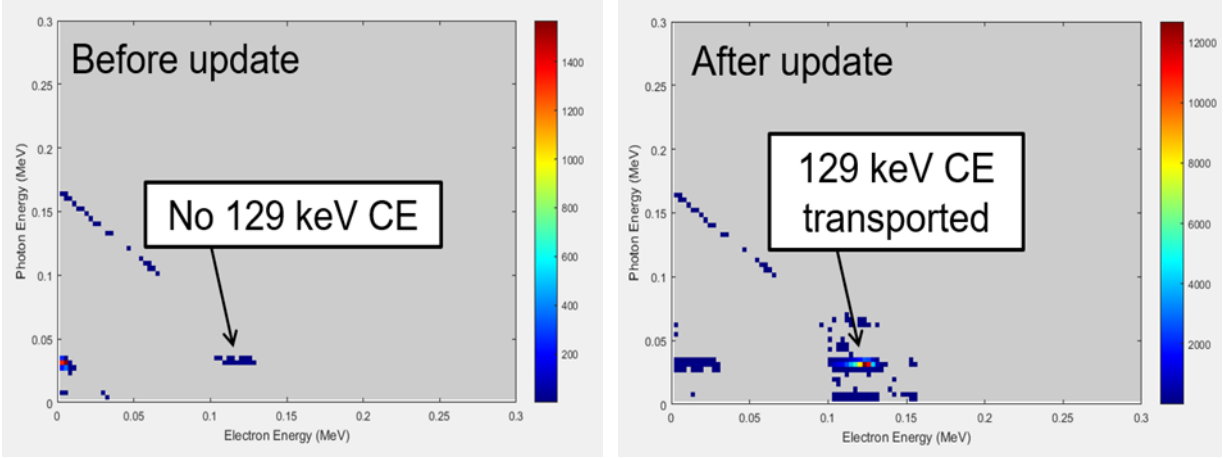

(a) (b)

Figure 4.3: Development of conversion electron transport

4.4 Validation with Experiments - Version 2.1.4

This section shows results from simulations of ^{135}Xe and ^{131m}Xe. The activity estimate of the sample was used to determine the number of particles to simulate. The singles and coincidence spectra of the two isotopes are presented.

The decay of ^{135}Xe results in the emission of a beta particle along with a gamma-ray or X-ray. Therefore, the beta spectrum has a continuum with endpoint energy of approximately 915 keV. The energies of the gamma-ray and X-ray are 250 keV and 30 keV, respectively. Figure 4.4a shows good agreement between the gamma spectra of the experiment and simulation apart from the difference of sample activity. Figure 4.4b compares the beta spectra of the experiment and simulation. The simulation has higher counts at low and high energies, which is likely due to the small range of the energy resolution curve. Therefore, a resolution function with a wider energy range may be required to properly broaden the simulated spectra. Additionally, the beta spectrum simulated is a

theoretical one, which also allows for some differences in the comparison.

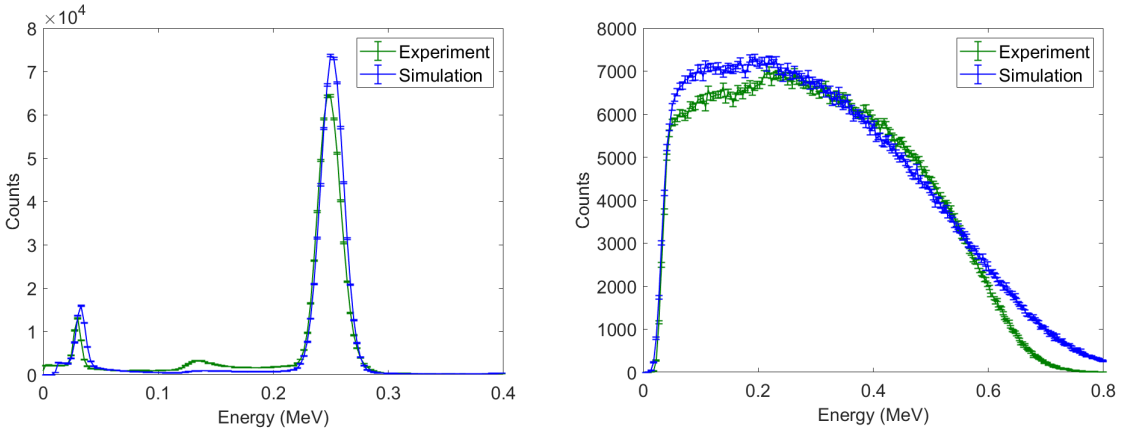

Figure 4.4: Singles spectra of (a) NaI(Tl) and (b) plastic scintillator for ^{135}Xe measurement (green) and simulation (blue).

Figure 4.5 shows the 2-D coincidence spectra for the experiment and simulation. Disagreement on the plastic energy axis again points to inadequacy in the energy resolution function due to energy range limitations. Overall, the simulation agrees well with the experiment in terms of detection efficiency. Improvements in the energy resolution measurement of the plastic detector are needed to allow for better agreement.

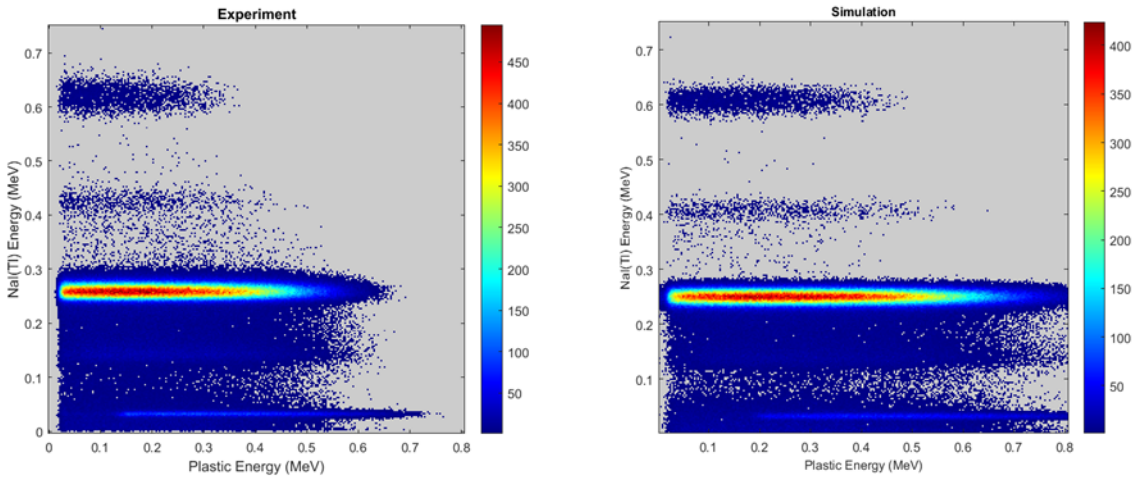

(a) (b)

Figure 4.5: Xenon-135 2-D coincidence spectra for (a) experiment and (b) simulation.

The decay of ^{131m}Xe results in two conversion electron energy peaks, 129 keV and 158 keV; however, the two peaks will be combined due to the energy resolution of the plastic. The energies of the gamma-ray and x-ray are 163 keV and 30 keV, respectively. Figure 4.6a shows good agreement for the gamma spectra, although the activity is less. Figure 4.6b shows the beta spectrum from the experiment and simulation. The results show that the energy resolution function is incorrect: the 158-keV peak is not as distinct in the simulation as the experiment.

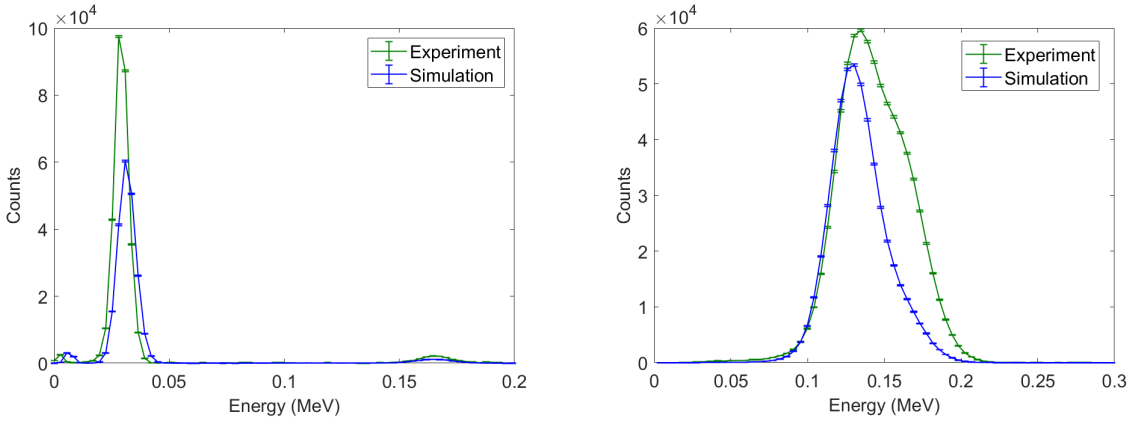

(a) (b)

Figure 4.6: Singles spectra of (a) NaI(Tl) and (b) plastic scintillator for ^{131m}Xe measurement (green) and simulation (blue).

A comparison of the 2-D spectra is shown in Figure 7 and illustrates the uncertainty in the energy resolution of the plastic, as well as the source activity. A more detailed analysis of the code is required to identify the true sources of the differences between the measurement and simulation. The low electron and photon energies of ^{131m}Xe could also contribute to the relative error of both simulation and measurement leading to less agreement in the comparison.

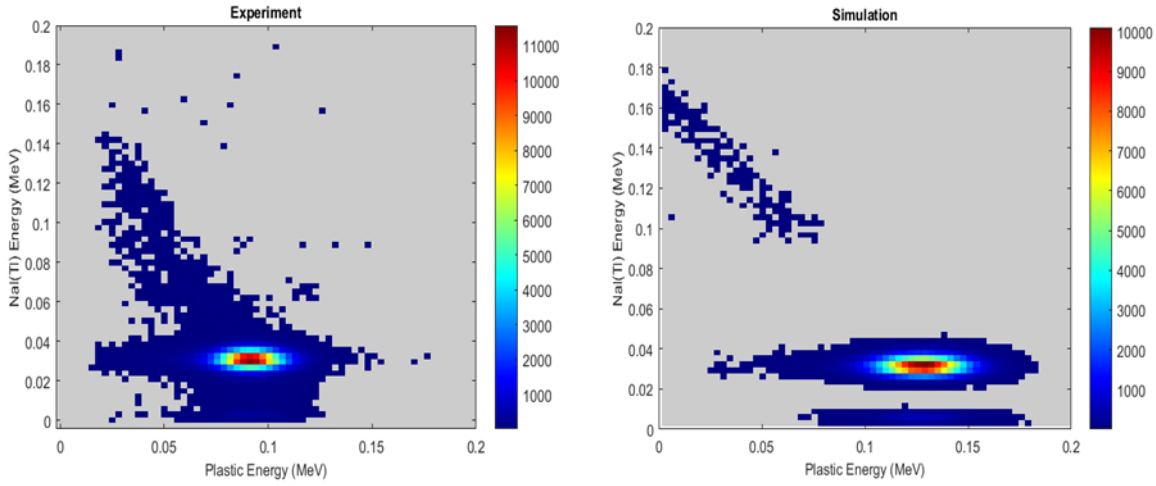

(a) (b)

Figure 4.7: Xenon-131m 2-D coincidence spectra for (a) experiment and (b) simulation.

4.5 Summary of Changes for Versions 2.1.5 and 2.1.6

As shown in Section 4.4, version 2.1.4 needed additional updates to improve agreement between experiment and simulation. Version 2.1.5 was updated to include a Single Decay Source for ^{127}Xe. Through a series of tests, it was found that the branching ratios for the low energy X-rays and CE emissions were slightly off. As a result, the simplified source developed for the metastable isotopes was shown to be too simplified because it emits the CEs in a slightly lower ratio than expected. This difference in branching ratios was the major reason for the difference in beta spectra in Figure 4.6b. Therefore, in version 2.1.6 the Single Decay Source was improved drastically for the metastable isotopes and slightly for the non-metastable isotopes. This version also removed the simplified decay source for the metastable isotopes. Additionally, a method of modifying the beta spectrum was implemented to allow for better agreement with experiments by modifying the high energy beta tail. The validation results of version 2.1.6 are presented in the following section.

4.6 Validation with Experiments - Version 2.1.6

This analysis uses the Gaussian Energy Broadening (GEB) function to simulate the spectrum shape as used in traditional MCNP instead of the function used in the previous validation section. The equation is a function of the full width at half maximum (FWHM) of the detector to be broadened,

$$FWHM = a + b\sqrt{E + cE^2} \tag{4.1}$$

where a, b, and c are in units of MeV, MeV$^{1/2}$, and 1/MeV and E is the energy of the photopeak in MeV. These coefficients are solved for by fitting the energy resolution points to Equation 1. Therefore, a detailed calibration is required in order to obtain the best agreement between simulation and experiment. Broadening of the MCNPX-PoliMi output was done in MATLAB by randomly sampling a Gaussian distribution based on Equation 4.1.

4.6.1 Results

In this section, the simulation results are compared to experimental data for each of the isotopes of interest. The background and gas background are subtracted for the experimental data; thus, no detector background is included in the simulation.

4.6.1.1 Xenon-135

The simulation of ^{135}Xe decay is the simplest of the four isotopes due to the emission of betas in coincidence with primarily a 250 keV photon. The use of Equation 4.1 has improved agreement between the measurement and simulation in comparison to version 2.1.4. The NaI(Tl) spectrum comparison, Figure 4.8a, shows good agreement between the experiment and simulation, producing two major photopeaks at 30 and 250 keV. The plastic scintillator spectrum comparison, Figure 4.8b, shows the beta spectrum of ^{135}Xe which has an endpoint energy of 915 keV. The experiment and simulation spectra have similar shape with the simulation having slightly more counts, due to the activity calculation. The tail end of the beta spectrum has more counts for the simulation than the experiments and is likely due to high energy electrons escaping the plastic cell experimentally and the method in which the simulation produces a beta spectrum. The tail end of the spectrum can further be modified in MCNPX-PoliMi, but a more accurate activity calculation and simulation geometry would improve the comparison. The coincidence histograms in Figure 4.9 shows similar features for the experiment and simulation with the 250 keV ROI having the most counts and the simulation having more total coincidence counts than the experiment. Figure 4.10 shows the projections of the coincidence histograms on the x-axis and y-axis for the plastic scintillator and NaI(Tl) detectors, respectively. The difference in gamma efficiency is illustrated in Figure 4.10b where the coincidence beta spectrum of the simulation has more counts than the experiment due to the activity estimation and the omission of the NaI(Tl) reflector. This trend is also seen for the following results.

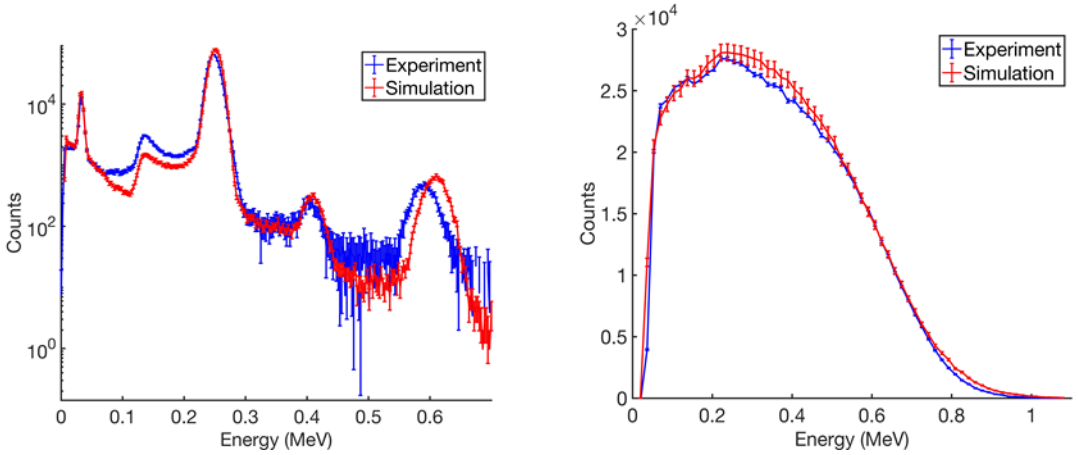

(a) (b)

Figure 4.8: Singles spectra of (a) NaI(Tl) and (b) plastic scintillator for ^{135}Xe measurement (blue) and simulation (red).

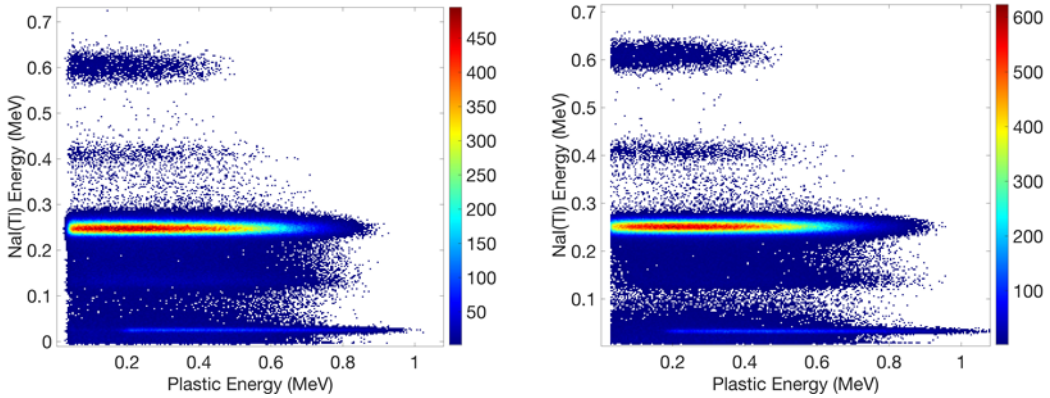

(a) (b)

Figure 4.9: Xenon-135 2-D coincidence spectra for (a) experiment and (b) simulation.

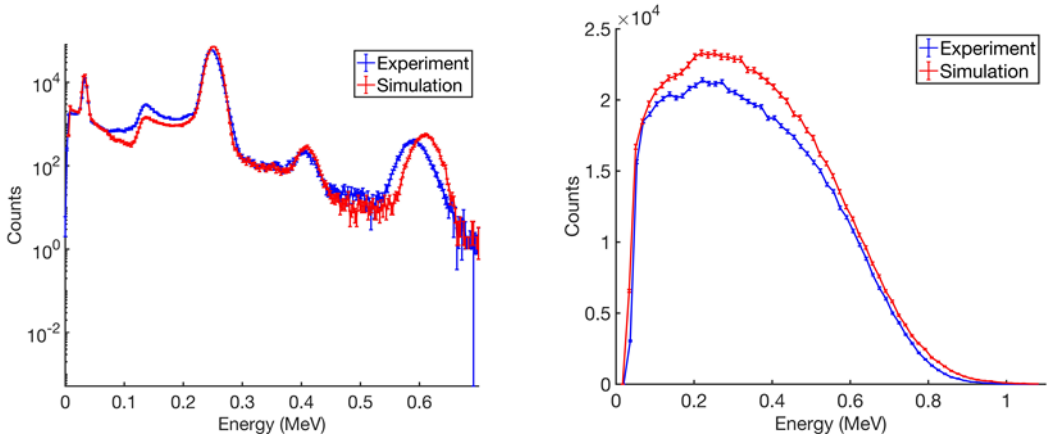

Figure 4.10: Individual coincidence spectra of (a) NaI(Tl) and (b) plastic scintillator detectors for ^{135}Xe.

4.6.1.2 Xe-133

The simulation of ^{133}Xe is more challenging than ^{135}Xe due to its complex decay scheme, which often includes a beta emission followed by a coincidence gamma-ray or coincidence conversion electron and X-ray. Additionally, the sample is produced through fission, which results in a small amount of ^{131m}Xe contamination that was not added to the simulation. The NaI(Tl) spectrum comparison, Figure 4.11a, shows good agreement between the experiment and simulation, producing two major photopeaks at 30 and 81 keV. Figure 4.11b shows the beta spectra comparison where the 45 keV conversion electron peak is much higher for the simulation than experiment due to threshold limitations of the simulation. Otherwise, the beta spectrum shape is similar between the experiment and simulation. Figure 4.12 shows the coincidence histogram of the experiment and simulation, with high count regions for the beta coincidences with 30 and 81 keV photons, with a slight bump in the experimental coincidence histogram at approximately 130 keV for the plastic (x-axis) and 30 keV for the NaI(Tl) (y-axis) due to the ^{131m}Xe contamination. The projected coincidence spectra are shown in Figure 4.13. The NaI(Tl) spectra in Figure 4.13a have similar features with the simulation again having more counts. The beta coincidence spectrum of the simulation also has more counts again due to the higher gamma efficiency of the simulation compared to the experiment. The

contamination of ^{131m}Xe is also producing a slight bump at 129 keV for the experiment in Figure 4.13b.

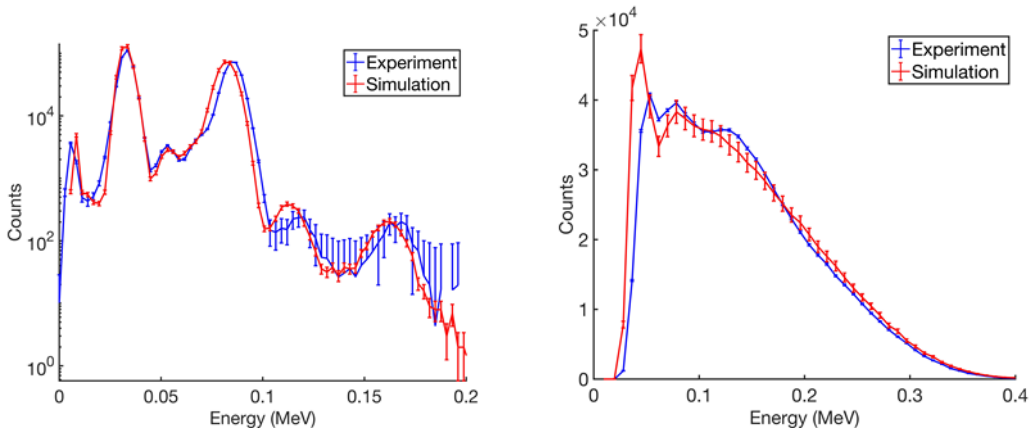

(a) (b)

Figure 4.11: Singles spectra of (a) NaI(Tl) and (b) plastic scintillator for ^{133}Xe measurement (blue) and simulation (red).

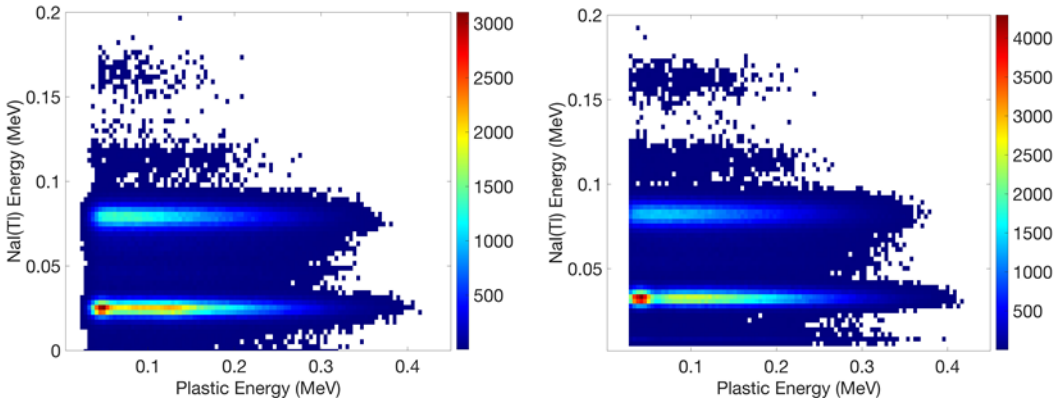

(a) (b)

Figure 4.12: Xenon-133 2-D coincidence spectra for (a) experiment and (b) simulation.

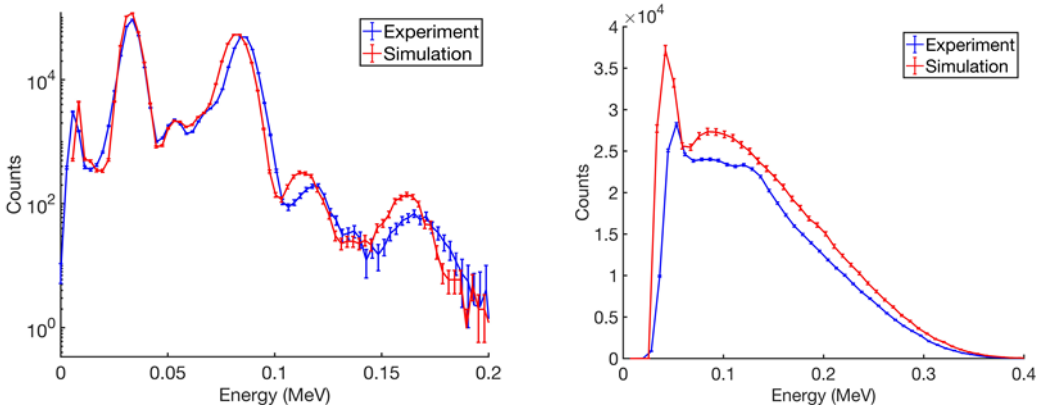

(a) (b)

Figure 4.13: Individual coincidence spectra of (a) NaI(Tl) and (b) plastic scintillator detectors for ^{133}Xe.

4.6.1.3 Xe-131m

The simulation of ^{131m}Xe in contrast to ^{133}Xe involves distinct CE energies. The NaI(Tl) spectrum comparison, Figure 4.14a, shows similar features for the experiment and simulation, producing 30 keV and 163 keV photopeaks. The plastic spectrum comparison, Figure 4.14b, shows experimental and simulation agreement and Gaussian fits of the 129 and 158 CE peaks for the experiment. Figure 4.15 shows almost identical features with the highest counts in the 129 keV ROI and the simulation having more counts, minor differences in the size of the circle are due to energy resolution broadening. The coincidence spectra projections are shown in Figure 4.16. Again, the gamma efficiency for the simulation is higher resulting in more counts in the coincidence beta spectrum as shown in Figure 4.16b. However, agreement has greatly improved with the use of Equation 4.1 and updates to the source compared to results shown for version 2.1.4.

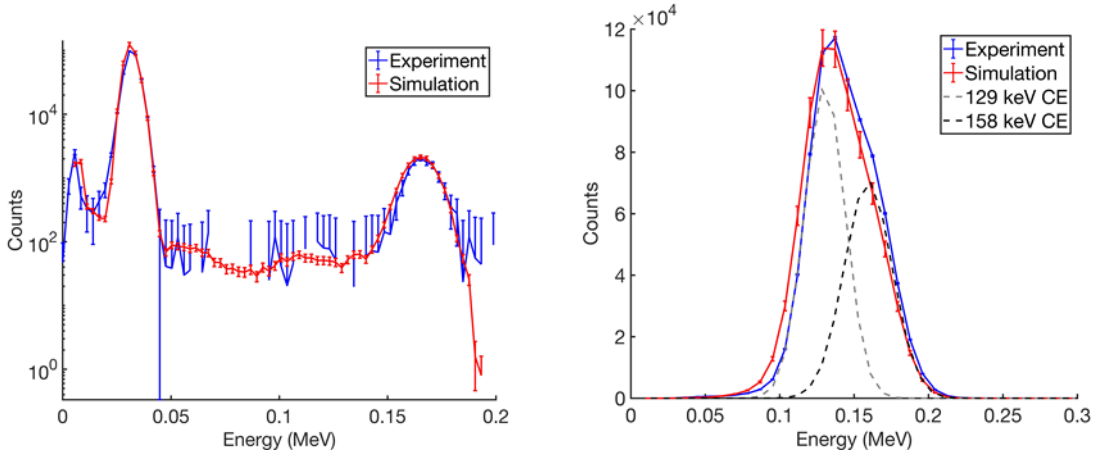

Figure 4.14: Singles spectra of (a) NaI(Tl) and (b) plastic scintillator for ^{131m}Xe measurement (blue) and simulation (red), with Gaussian fits to the experimental data to show the convolved 129 keV and 158 keV conversion electron energy peaks.

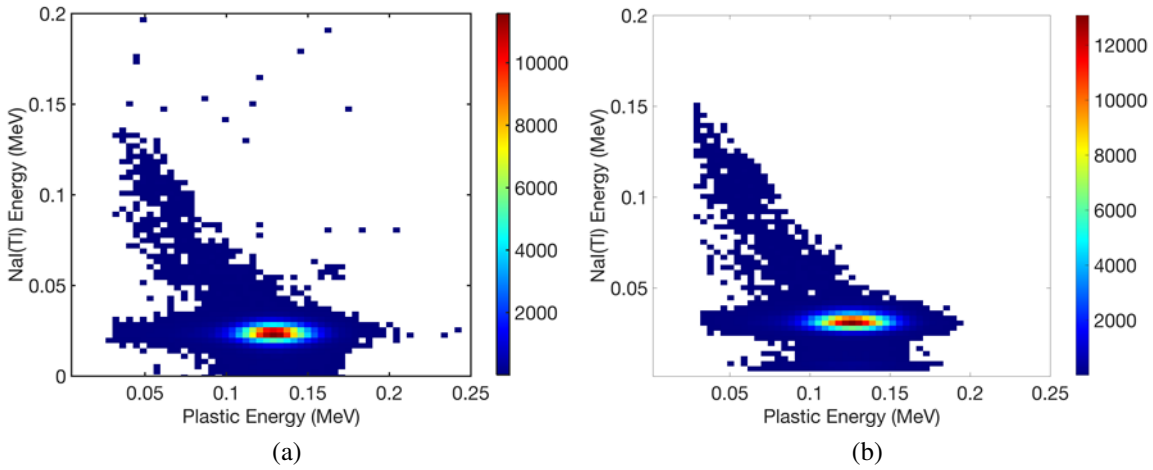

Figure 4.15: Xenon-131m 2-D coincidence spectra for the (a) experiment and (b) simulation.

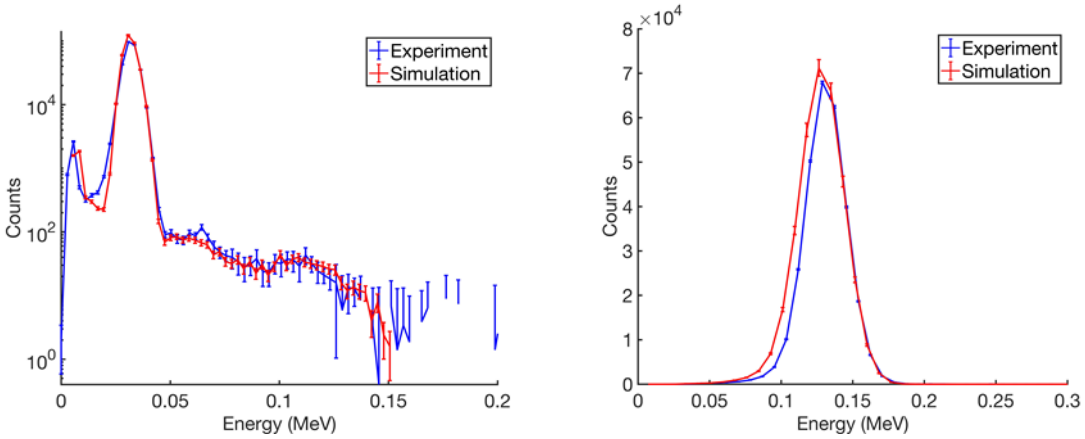

Figure 4.16: Individual coincidence spectra of the (a) NaI(Tl) and (b) plastic scintillator detectors for ^{131m}Xe.

4.6.1.4 Mixed Xe-133m, Xe-133, and Xe-135

The decay of ^{133m}Xe is more complex to simulate because it is constantly decaying into ^{133}Xe. Additionally, there was some ^{135}Xe still present in the cell that had to be considered. This simulation required the combination of individual simulations of ^{135}Xe, ^{133}Xe, and ^{133m}Xe using estimated activities. In contrast to the ^{133}Xe gamma spectra shown in Figure 4.11a, the ^{133m}Xe isotope also produces a 233 keV photon as shown on in Figure 4.17a. From ^{133}Xe decay, the 30 keV and 81 keV peaks are also present in the plot. The beta spectrum comparison, shown in Figure 4.17b, again overestimates the 45 keV conversion electron. However, there is good agreement between the experiment and simulation for the 199 keV conversion electron and the endpoint energies align fairly well. The coincidence spectrum, Figure 4.18, shows the ROIs due to ^{133}Xe as well as the 199 keV ROI from ^{133m}Xe, illustrating the ability of this tool to simulate the detector response of mixed samples. There is an additional feature at the 250 keV gamma line due to the ^{135}Xe presence in the experiment. Projections of the coincidence histogram are shown in Figure 4.19. The NaI(Tl) spectra in Figure 4.19a show similar features to that of Figure 4.17a with the simulation having more counts. The beta spectrum in Figure 4.19b have similar features but again show that the higher gamma efficiency of the simulation results in more counts in the coincidence spectrum of the simulation.

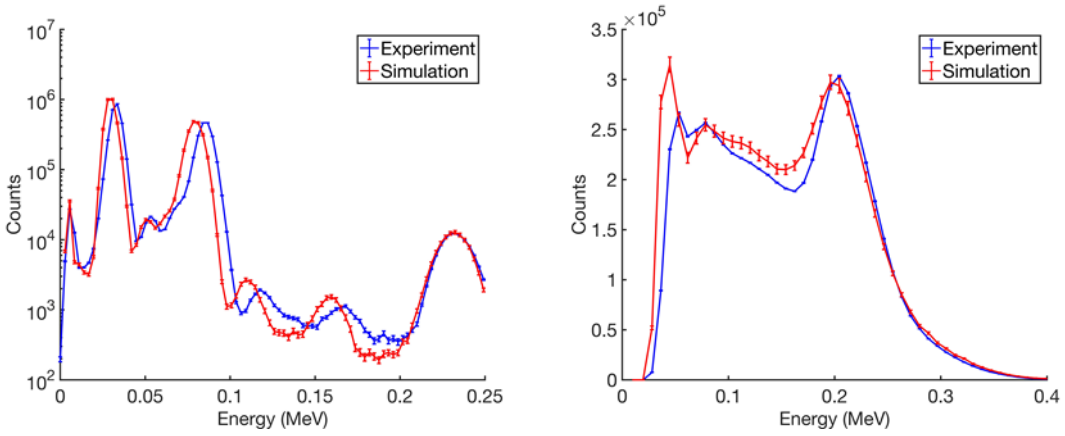

Figure 4.17: Singles spectra of (a) NaI(Tl) and (b) plastic scintillator for ^{133m}Xe, ^{133}Xe, and ^{135}Xe measurement (blue) and simulation (red).

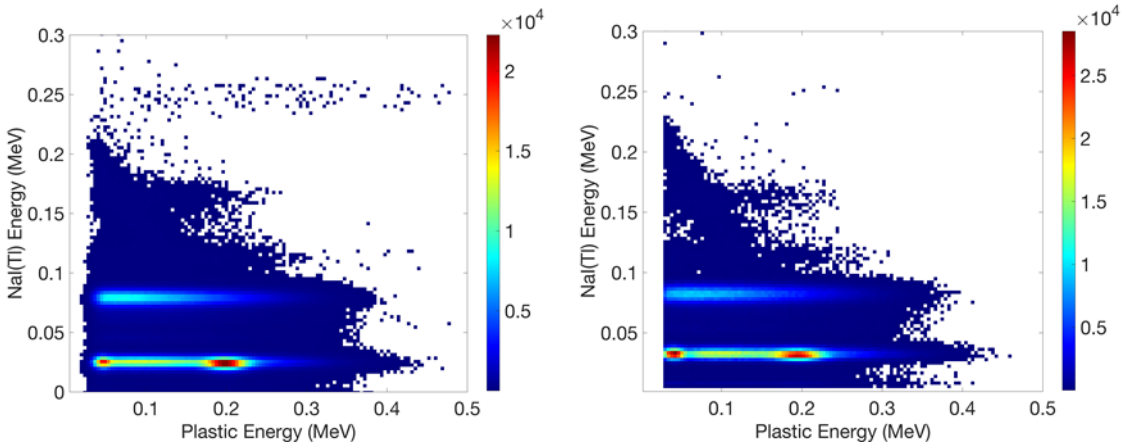

Figure 4.18: Xenon-133m, xenon-133, and xenon-135 2-D coincidence spectra for (a) experiment and (b) simulation.

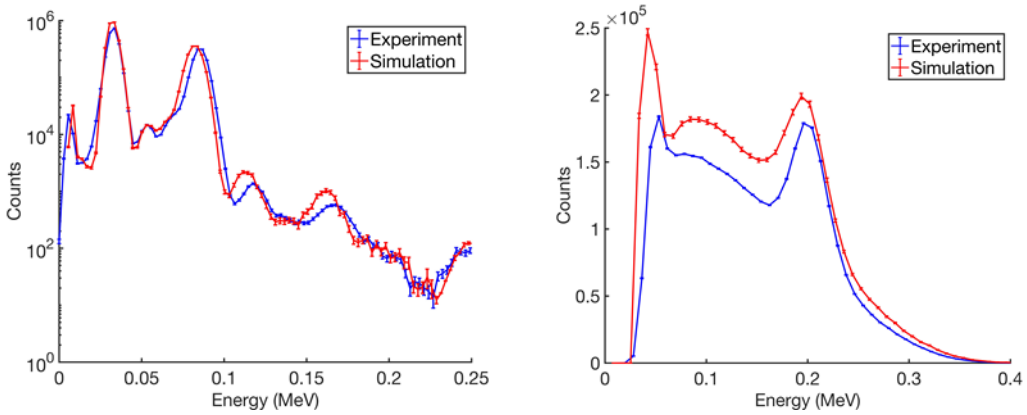

(a) (b)

Figure 4.19: Individual coincidence spectra of the NaI(Tl) (a) and plastic scintillator (b) detectors for mixed ^{133m}Xe, ^{133}Xe, and ^{135}Xe.

4.7 Conclusions

This chapter demonstrates and validates the use of a new Single Decay Option in MCNPX-PoliMi to simulate radioxenon decay using plastic and NaI(Tl) scintillators in a coincidence set-up. The results presented here include simulations of ^{135}Xe , ^{133}Xe, ^{131m}Xe, and a mixed source of ^{133m}Xe, ^{133}Xe, and ^{135}Xe and serve as validation of this tool for radioxenon detection in Comprehensive Nuclear-Test-Ban Treaty verification applications. The results show that the new tool is able to simulate the shape and magnitude of radioxenon signatures for both singles and coincidence mode. The observed differences between experiment and simulation were a result of having to estimate the activity of the sample and simplifications of the model. We also found that limitations arise if the resolution of the detector is not well known.

Further developments include the implementation of modified beta spectrum tails, low-energy x-ray emissions, light transport effects, and careful accounting of variances in detector geometry. This tool could be used to simplify current calibration measurements through simulation of the detector response, requiring fewer radioxenon measurements. Additionally, as shown with the mixed sample, this tool can be used to produce coincidence spectra for a variety of detector types with the purpose of training radionuclide analysts, as well as assisting in the analysis of measured samples such as

those collected by the IMS.

Chapter 5

Radioxenon Detector Development and Experiments

5.1 Introduction

The primary focus of this thesis was the development of an advanced radioxenon detector. After an extensive literature review, stilbene was chosen as the alternative material. Using stilbene instead of plastic in the beta-detection cell could create a more sensitive detector by 1) mitigating the memory effect [126], 2) improving the beta resolution, and 3) mitigating radon background using pulse shape discrimination (PSD) techniques [127]. Additionally, because stilbene is a crystalline organic scintillator, similar analysis techniques to those currently used for plastic scintillator cells can be employed. This use of an alternative scintillating material contrasts with the use of high-Z materials such as silicon or CZT, which produce large electron back-scatter effects in the spectrum that must be considered in analysis [55, 58, 64]. Furthermore, keeping a hollow-cell geometry maintains the near-4π geometry of the coincidence detection system, resulting in higher detection efficiencies than that of alternative silicon and CZT detector systems [60, 65]. Therefore, the goal of this research was to develop a robust stilbene beta cell detector to replace the plastic beta cell detectors currently in use. The next sections detail the testing of three prototype stilbene cells, manufactured in collaboration with Inrad Optics in Northvale, New Jersey [128]. However, the previous detectors developed using stilbene saw limitations in vacuum stability and thus were not fully tested as radioxenon detectors.

Compared to plastic, stilbene is more brittle and fragile, making it difficult to manufacture into a

variety of shapes. Stilbene, as with many detector materials, requires careful handling. For instance, dropping stilbene can cause the material to fracture or even break. Additionally, stilbene cannot be subject to sudden drastic changes in temperature as this could lead to cracks in the material. Previously developed stilbene cells were of the phoswich nature or used planar sheets of stilbene glued to act as the gas volume. As mentioned, the glued cells were not sufficient in acting as beta cells because they were not gas tight. Advances in technology allowed for collaboration with Inrad Optics to develop a hollow stilbene detector that could act as the beta cell detector similar to plastic. However, because of the fragility of stilbene, caution was taken in each prototype cell to maximize the ruggedness and optimize the detector response. Only certain shapes of stilbene are currently developed. This thesis presents the first known instance of a cylindrical stilbene beta cell detector.

5.2 Preliminary Stilbene Measurements and Simulations

As a first check to examine the benefits of stilbene as an alternative to plastic, experiments were conducted with cylindrical geometries of each. The first test comparing plastic and stilbene used solid cylindrical geometries on top of a solid NaI(Tl) crystal as shown in Figure 5.1. Data acquisition was done using CAEN electronics, details are discussed in Section 5.3.1. As mentioned previously, ^{137}Cs can be used to gain calibrate the coincidence system and can also be deconvolved to analyze beta cell detector resolution [129]. The Compton scatter of the 662-keV photon emitted by ^{137}Cs, results in partial energy deposition by the photon in each of the detectors. This energy deposition produces a diagonal line in the coincidence spectrum, where each x and y energy along the diagonal sum to 662 keV. The width of the coincidence line is attributed to the resolution of the two detectors or the coincidence system. Therefore, comparing the ^{137}Cs spectra of the two detectors gives insight to stilbene resolution as compared to plastic. The resolution is expected to be improved due to stilbenes increased light output. However, light transport and collection efficiency can greatly alter the detector response, degrading the resolution.

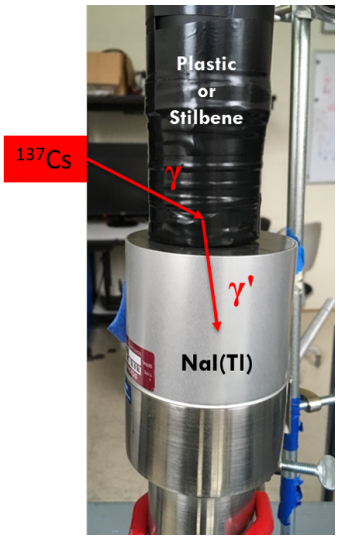

Figure 5.1: Experimental setup of preliminary plastic and stilbene comparison using solid cylindrical geometries placed on top of a cylindrical NaI(Tl) crystal.

Figure 5.2 shows the coincidence spectra of the plastic and stilbene measurements with ^{137}Cs. As shown, the thickness of the stilbene line is thinner than that of the plastic. Since the same NaI(Tl) detector was used for both acquisitions, the difference in organic detector response is due to different response of the plastic and stilbene. Horizontal cuts on the coincidence spectrum are shown in Figure 5.3. The horizontal cuts are a result of summing NaI(Tl) energy bins from 250 to 275 keV into one histogram that is plotted along the x-axis, representing the beta coincidence spectrum. The beta spectrum comparison at this energy range shows a 29% improvement of the FWHM for the stilbene crystal compared to the plastic scintillator.

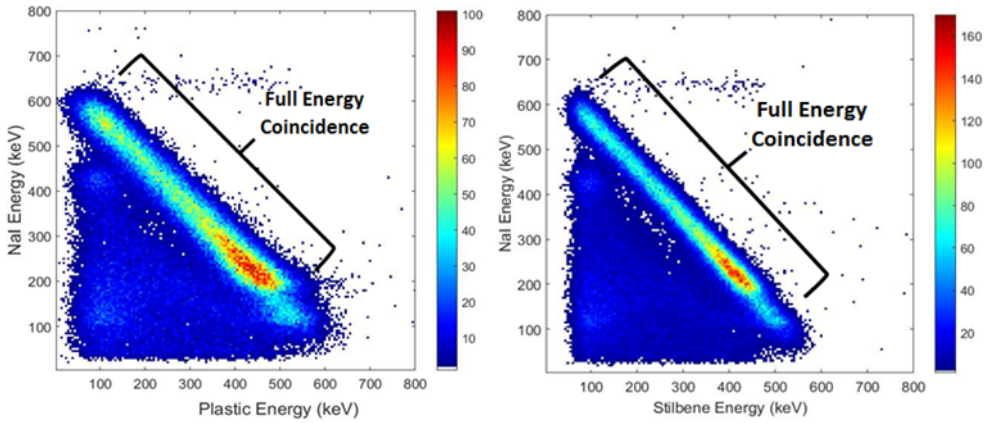

(a) (b)

Figure 5.2: Coincidence spectra from a ^{137}Cs measurement with (a) plastic scintillator and (b) stilbene crystal. The stilbene line is thinner than that of the plastic line suggesting an improvement in energy resolution.

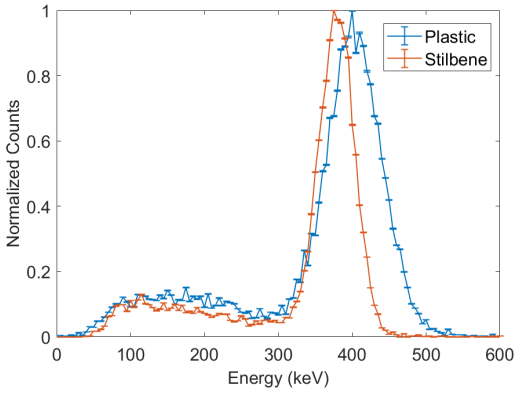

Figure 5.3: Comparison of horizontal cuts on the coincidence histogram for plastic and stilbene where the stilbene crystal has an improved FWHM of 29% compared to the plastic scintillator.

Using the newly developed MCNPX-PoliMi tool discussed in Chapter 4, simulations were conducted to analyze improvements on radioxenon detection. Mixed samples of ^{133}Xe and ^{131m}Xe were simulated to examine how the metastable isotope could better be identified. Figure 5.4 shows the coincidence spectra of simulated plastic and stilbene detector response. For Figure 5.4b, the ^{131m}Xe ROI highlighted by the counts denoted in red, is more concise compared to Figure 5.4a.

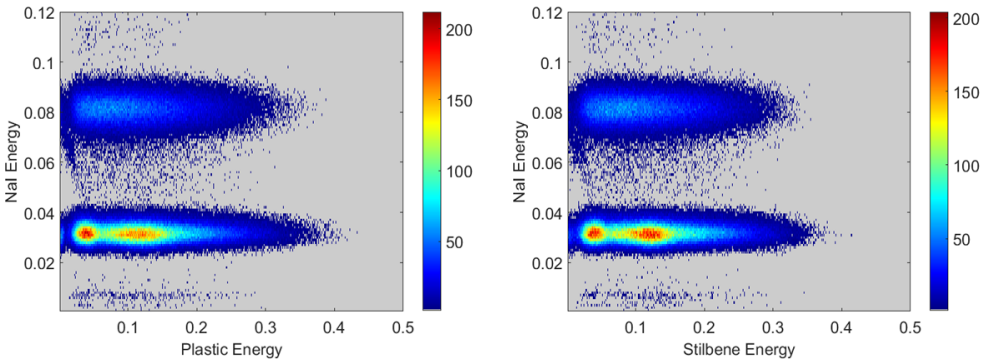

Figure 5.4: Simulated coincidence spectra of mixed ^{133}Xe and ^{131m}Xe samples for (a) plastic and (b) stilbene.

Figure 5.5 shows the beta spectrum of two different ratios of mixed ^{133}Xe and ^{131m}Xe samples. Figure 5.5a shows a 1-to-1 ratio of the sample, where the stilbene spectrum has a sharper peak than the plastic spectrum. Therefore, the continuum due to ^{133}Xe decay has a smaller impact on the counts in the ^{131m}Xe ROI for stilbene compared to plastic. The 5-to-1 ratio of the sample is shown in Figure 5.5b. In this figure, the ^{131m}Xe peak is almost hidden by the activity of ^{133}Xe. However, a defined peak is shown for the stilbene spectrum that is not present for the plastic spectrum. The results presented in this section highlight how the improved resolution of the stilbene detector can impact detection sensitivity of the metastable isotopes by decreasing ^{133}Xe interference.

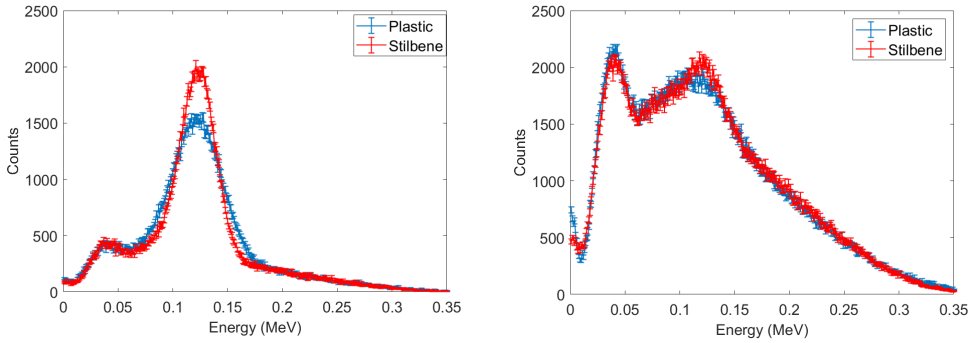

(a) (b)

Figure 5.5: Simulated beta spectra of mixed ^{133}Xe and ^{131m}Xe samples with an (a) 1 to 1 ratio and (b) 5 to 1 ratio. The improved stilbene resolution tightens the ROI bounds, leading to decreased ^{133}Xe interference.

5.3 Prototype 1

The first stilbene cell was manufactured by drilling through a cylindrical piece of stilbene. The cylinder was not completely drilled through so that the stilbene material resembles a cup. The endcap consisted of machinable ceramic with a brass insert, where the metal gas line would be attached. Ceramic was used so that stress would not be applied directly to the stilbene material. Figure 5.6 shows pictures of the first stilbene prototype. The dimensions of the cell are 4.45 cm long, 1.8 cm wide and 2 mm thick.

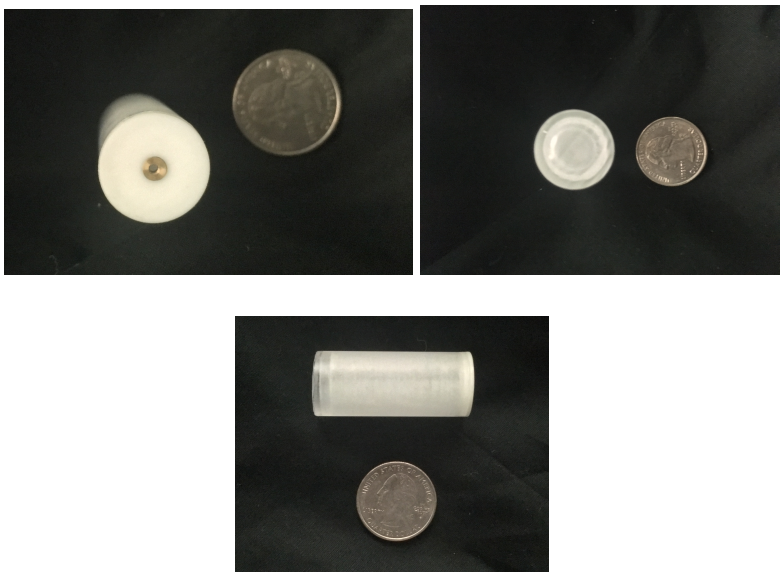

Figure 5.6: First stilbene prototype with ceramic endcap for gas line.

5.3.1 Experimental Setup

Each prototype was tested alongside a plastic beta cell detector developed by PNNL, shown in Figure 5.7. The same PMT type, 1-inch Bicron model 9111SB, was used for both cells with the threshold and voltage optimized. The same CsI(Na) well detector was used for both beta detectors, such that for each measurement the CsI(Na) detector remained in place while the beta cells were switched. The stilbene cell was wrapped with Teflon and black electrical tape. The plastic cell had a permanent 3D-printed housing to prevent exposure to light. A schematic of the coincidence geometry is shown in Figure

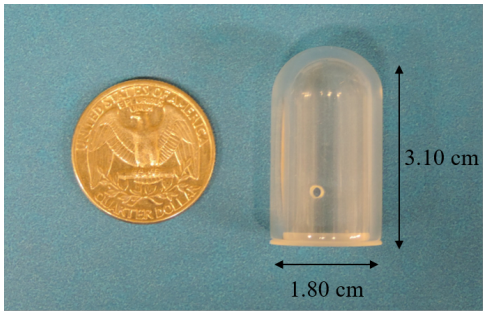

Figure 5.7: Plastic scintillator cell developed by PNNL.

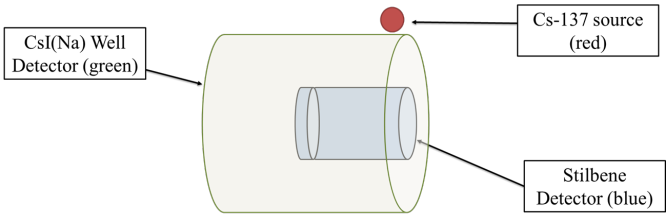

Figure 5.8: Schematic of experimental setup with beta cell and CsI(Na) detector.

A NIM high-voltage supply, CAEN N1470, was used to power the detectors. The DT5730 desktop digitizer by CAEN was used for data acquisition. These digitizers record waveforms with a 2-ns time step. The DPP-PSD firmware of the DT5730 allows for gain amplification on board by restricting the 2-V range to 0.5-V increasing the gain by 4. For the beta detectors, amplification was done using the digitizers gain amplification. A NIM bin amplifier was used for the CsI(Na) detector due to its low amplitude pulses. An example of the amplified pulses for the CsI(Na) detector is shown in Figure 5.9. Examples of the amplified pulses for the plastic and stilbene beta cells are shown in Figure 5.10

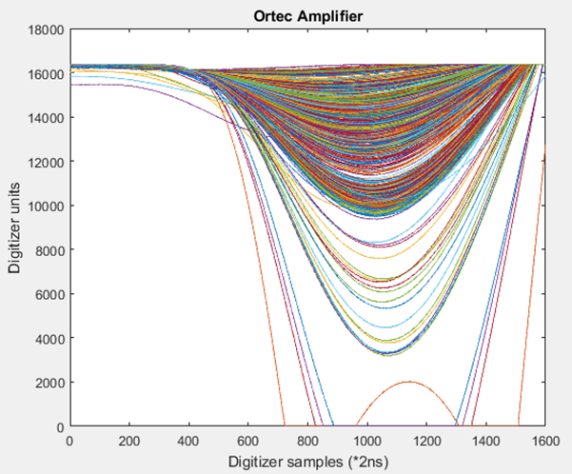

Figure 5.9: Amplified pulses for CsI(Na) detector.

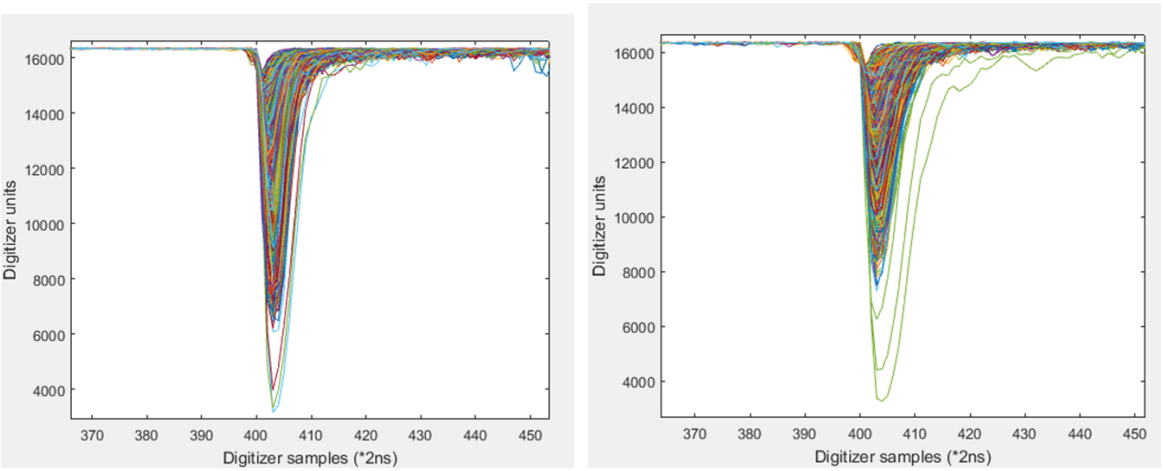

(a) (b)

Figure 5.10: Amplified pulses for (a) plastic and (b) stilbene beta cells.

The data from the digitizer were recorded using DAFCA, a program developed at the University of Michigan. DAFCA allows for the waveforms to be recorded along with list mode information such as the time of the event. The data files produced by DAFCA were processed using personally developed MATLAB scripts. The setting of the shift registers for the digitizer controls whether the measurement is taken in singles or coincidence mode. If the data were taken in singles mode, coincidence events were identified using the time tags given by DAFCA. Therefore, for the majority of the experiments, the shift registers were set such that only coincidence events were acquired to simplify analysis and minimize data file size.

The pulse height and pulse integral were acquired from the data files. Because the CsI(Na) pulses went through a NIM amplifier they are filtered and thus pulse height and pulse integral gave similar results. Because the beta cell pulses gain was increased their shape was not modified and thus typically, the pulse integral was used for data analysis. To plot the coincidence spectrum, a personally developed MATLAB function was created to bin the results in a 2D histogram and then plot using the MATLAB image function. The discussed electronics and data processing techniques were used for the preliminary and stilbene prototypes 1 and 2 measurements.

5.3.2 Measurement Results

The testing for the first prototype was conducted at the University of Michigan and consisted of ^{137}Cs and ^{252}Cf measurements. Figure 5.11 shows the coincidence spectra the of ^{137}Cs measurement for the plastic and stilbene detectors. It is expected that the Compton edge for the 662-keV gamma ray occurs at 478 keV. However, the stilbene cell response, Figure 5.11b, shows counts extending beyond the 478 keV Compton edge (end of the diagonal line). Because energy deposition of the ^{137}Cs beyond 478 keV is not possible with Compton scattering, this result suggests that the light output of the stilbene cell in non-uniform. This energy spread at the Compton edge is not present in the plastic spectrum, Figure 5.11a.

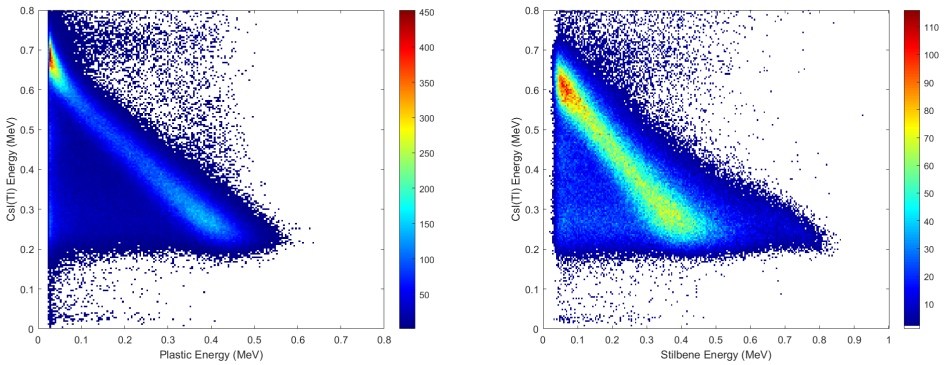

(a) (b)

Figure 5.11: Coincidence spectra of ^{137}Cs measurement for (a) plastic and (b) stilbene detectors.

Next, the beta spectrum of ^{137}Cs was measured for each of the detectors as shown in Figure 5.12. There is some low energy noise from the plastic detector, likely due to a light leak, that is cut off in the figure but otherwise the response is reasonable. However, the Compton edge for the stilbene detector is extended over a wide range of energies, different from the distinct Compton edge of the plastic detector. From the figure, it appears as if stilbene has two Compton edges due to 478 keV.

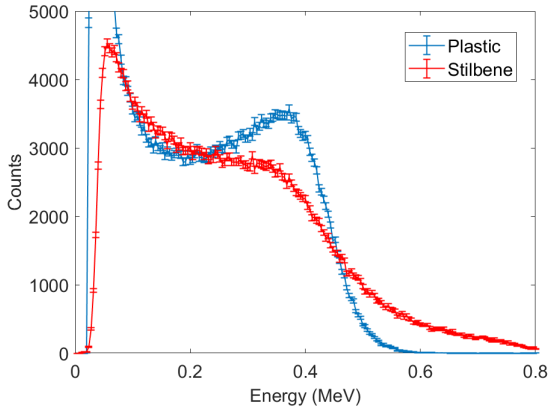

Figure 5.12: Beta spectrum comparison for ^{137}Cs measurement, where the Compton edge is extended for the stilbene detector showing degradation in the energy resolution.

To further test this idea, the stilbene source was measured at two locations on the stilbene cell as shown in Figure 5.13a. Figure 5.13b shows the response of the stilbene cell for the two source locations. Placing the source on the side contributes to the first Compton edge because less light is transported to the PMT. Placing the source at the top of the cell, it is assumed that events occurring in the bottom endcap contribute to the second Compton edge, since the light does not have to travel far to reach the PMT. These results are reasonable because it is expected for the surface closest to the PMT to have the highest light collection efficiency. However, this significantly degrades the beta energy resolution needed to identify radioxenon isotopes.

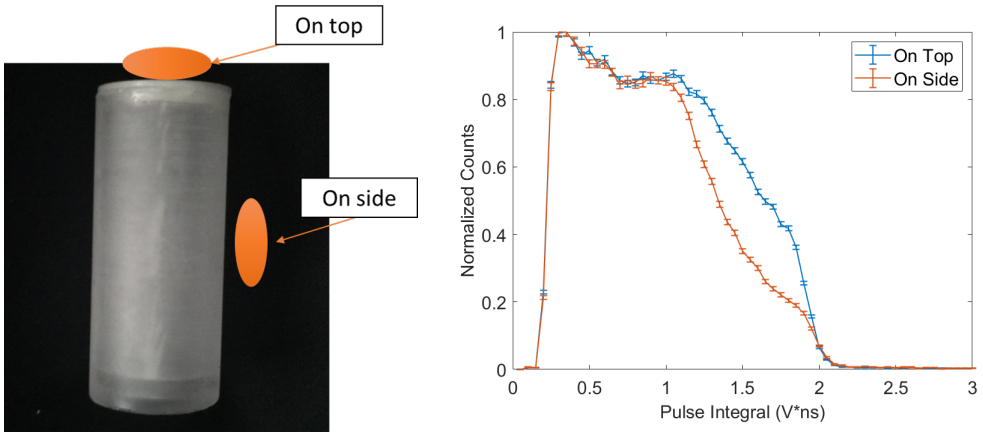

(a) (b)

Figure 5.13: Light output experiment; (a) locations of stilbene source and (b) detector response of stilbene at the two source locations.

Although the light output of the stilbene detector was non-uniform, a ^{252}Cf measurement was conducted. The purpose of this measurement was to examine the PSD properties of a hollow stilbene crystal. To do this, the waveform data acquired was analyzed for its tail and total integral values. Figure 5.14 shows the results of this analysis, where the neutrons are represented by the top band of points because more light is produced in the tail of the pulse and gamma rays are represented by the bottom band of points. This figure shows that there is separation between the neutrons and gamma rays emitted by ^{252}Cf due to the difference in light intensity of the tail of the pulse. Additionally, there is a curve in the tail integral versus total integral plot, which is attributed to the light output difference based on location of interaction in the cell. This preliminary result shows that the cell can perform PSD.

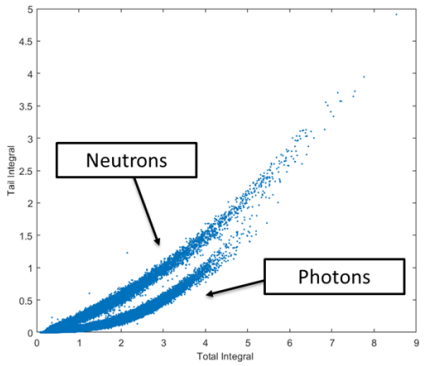

Figure 5.14: Tail versus total integral plot of ^{252}Cf measurement in stilbene cell. There is separation between the neutron and gamma emissions showing that the cell is capable of performing PSD.

5.4 Prototype 2

In an effort to improve the light output, the ceramic endcap of prototype 1 was replaced with a stilbene endcap containing a hole for the gas line. The testing for the second prototype was conducted at the University of Michigan and consisted of ^{137}Cs measurements. The same CsI(Na) well detector as the previous section was used, along with the same electronics and data processing techniques. This cell was slightly shorter than prototype 1 due to the removal of the ceramic endcap, which was cut off. Figure 5.15 shows images of the second stilbene cell prototype.

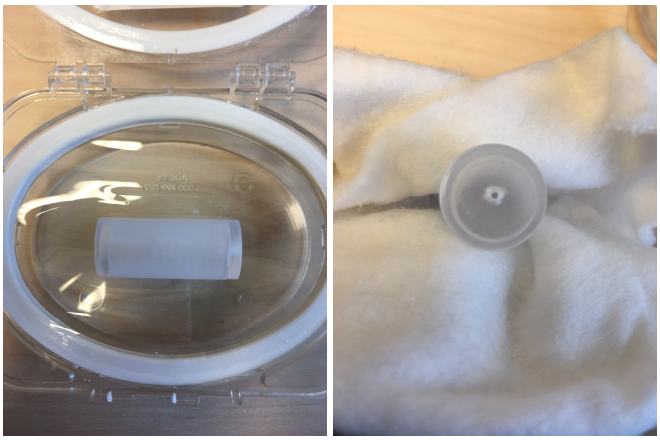

Figure 5.15: Second stilbene prototype with hole in stilbene endcap for gas line.

5.4.1 Measurement Results

To test the improvements in light output, ^{137}Cs was again measured. Figure 5.16 shows the coincidence spectra of the ^{137}Cs measurement for the plastic and stilbene detectors. Because the CsI(Na) detector is constant in both experiments, by visual inspection it is shown that the stilbene detector (5.16b) has a better resolution than the plastic detector (5.16a). The stilbene detector also appears to have a higher efficiency likely due to its increased detector volume (~61%) compared to plastic.

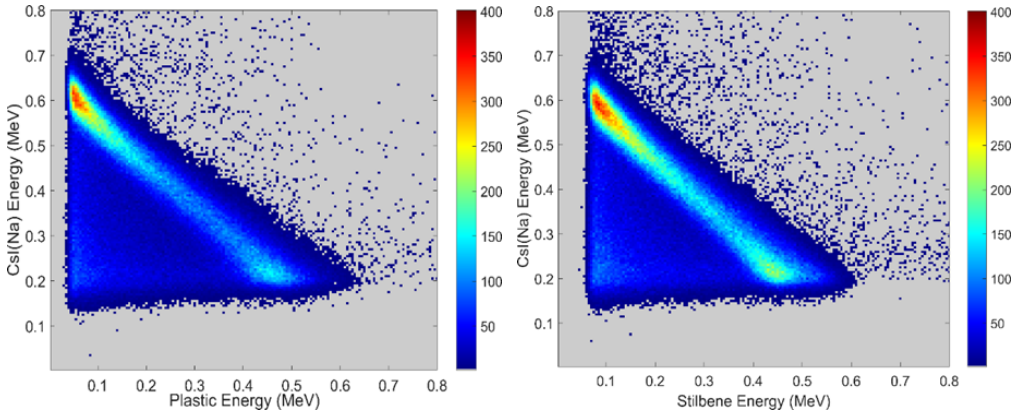

(a) (b)

Figure 5.16: Coincidence spectra of ^{137}Cs measurement for (a) plastic and (b) stilbene detectors with CsI(Na).

Perpendicular cuts on the coincidence spectrum are shown in Figure 5.17, to compare resolutions of the beta detectors. Figure 5.17a shows a cut at approximately 129 keV and Figure 5.17b shows a cut at approximately 198 keV for the plastic and stilbene detectors in coincidence with CsI(Na). These energies represent the conversion electron energies of ^{131m}Xe and ^{133m}Xe. The FWHM of stilbene decreases by 33% and 12% for 129 keV and 198 keV, respectively. Thus, this stilbene cell prototype has improved resolution with the replacement of the ceramic endcap with stilbene. To further characterize the detector radioxenon measurements are needed. This was attempted by taping the hole of the stilbene cell and injecting ^{127}Xe gas with a syringe. However, the stilbene

cell could not withstand the constant handling and shattered. Additionally, the efficiency of the measurement was very low due to the constant leaking of the gas. Thus, a new prototype cell was manufactured.

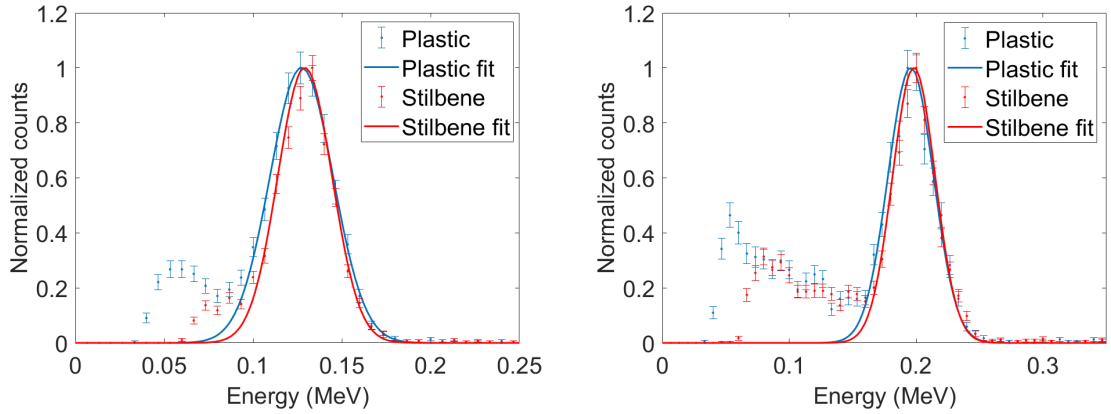

Figure 5.17: Coincidence spectra cuts for ^{137}Cs measurement at approximate energies of (a) 129 and (b) 198 keV, which correspond to the metastable isotope energies. The FWHM is decreased for stilbene which allows for improvements to measurement sensitivity.

5.5 Prototype 3

To create a more rugged stilbene cell, the walls and endcaps of the material were made thicker (2.8 mm). The width of the cell remained at 1.8 cm and the length was shortened to 4.1 cm. Additionally, for this prototype, instead of the cup body with one endcap, prototype 3 consisted of a cylindrical body with two endcaps. The endcap to be coupled to the PMT had an optical window permanently attached so that the stilbene surface was not mishandled. The opposite endcap had a Macor endcap attached again to protect mishandling of the stilbene surface. The hole for the stilbene endcap was wider than the Macor endcap to ensure that the gas line would not touch the stilbene endcap. Figure 5.18 shows the stilbene cell before the addition of the optical window and Macor endcap. Notice that this prototype is more polished than the previous two prototypes. Based on the results of prototype 2, this cell was taken to PNNL to measure the four radioxenon isotopes of interest and radon.

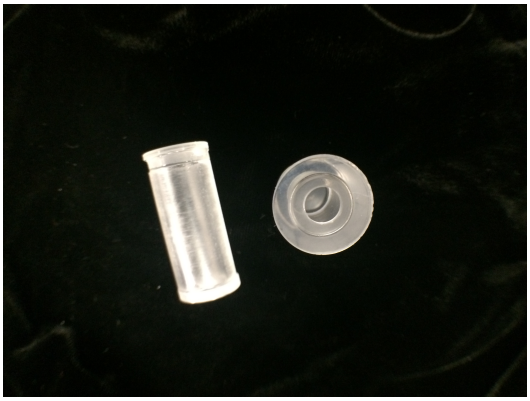

Figure 5.18: Third stilbene prototype manufactured with a cylindrical body and two endcaps to increase the structural stability of the cell.

5.5.1 Experimental Setup

As with the previous prototype measurements, the stilbene cell was tested alongside the rounded plastic cell developed by PNNL. Both plastic and stilbene cells were placed inside 3D-printed plastic housings to make the cells light tight and protect them from outside forces. Each cell was positioned inside a well-type NaI(Tl) detector to maintain the near-4π geometry of the beta-gamma coincidence setup. It is important to note that the stilbene cell prototype is longer and thicker than the traditional plastic cell, increasing the inner volume of the stilbene cell by approximately 20%. Both coincidence detector setups were placed inside a lead cave with a block of lead in between the NaI(Tl) detectors. A flexible tygon gas line was inserted into the Macor endcap of the stilbene cell to allow for flexibility in changing the gas-line, as shown in Figure 5.19a. The plastic scintillator cell used for this experiment had a permanently attached metal gas line. The gas lines of the plastic scintillator cell and stilbene cell were teed into one and connected to the gas manifold used for sample injection. Figure 5.19b shows the experimental setup of the coincidence detectors.

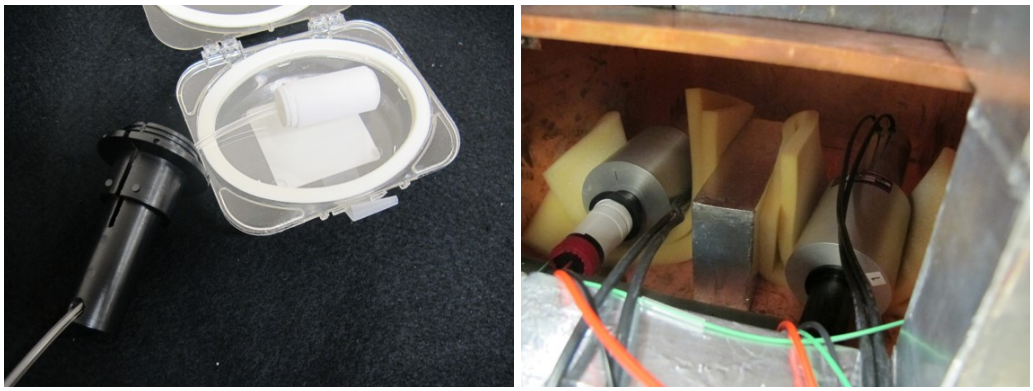

(a) (b)

Figure 5.19: Experimental setup; (a) plastic housing and flexible tubing used for the stilbene cell and (b) side-by-side beta-gamma coincidence experimental setup with stilbene on the left and plastic on the right (b).

Different electronics and data processing techniques were used for the measurement campaigns at PNNL. A National Instrument PXI crate containing the high voltage power supply and digitizer was used. Data acquisition was done using an XIA PIXIE-4 pulse processor. PNNL has developed a GUI for data acquisition where data acquired in list mode is converted to PBG file data that can be viewed in real-time. The final PBG files contain the binned singles and coincidence data preventing the need for data analysis techniques to produce the spectra. However, for these measurement campaigns list mode data was also acquired to allow for in-depth data analysis. The list mode data format outputs similar information to DAFCA. However, a key difference is that PIXIE-4, stores the hit pattern of the channels making it easy to pull out coincidence events versus analyzing the difference in time. The coincidence time window is set at the beginning of data acquisition for PIXIE-4. To analyze this data, personally developed MATLAB scripts were used. There are various list mode versions for PIXIE-4, with mode 100, allowing for waveform acquisition. The waveforms recorded by PIXIE-4 undergo a trapezoidal filter and are recorded in 13.3-ns time steps. This digitizer was developed to measure high purity germanium pulses; thus, fast pulses are typically difficult to digitize using this system. However, impedance mis-match of the cables stretches the fast pulses, allowing them to be digitized. Waveform data acquisition was only taken for a few

measurements, because it results in large datasets.

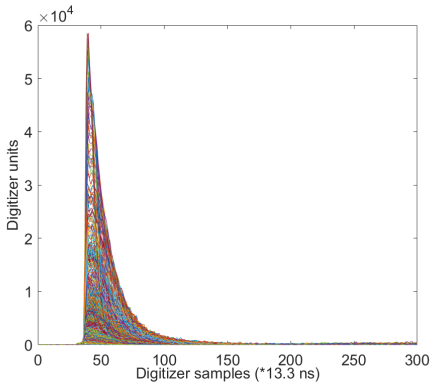

Figure 5.20: Digitized NaI(Tl) pulses from PIXIE-4 pulse processor.

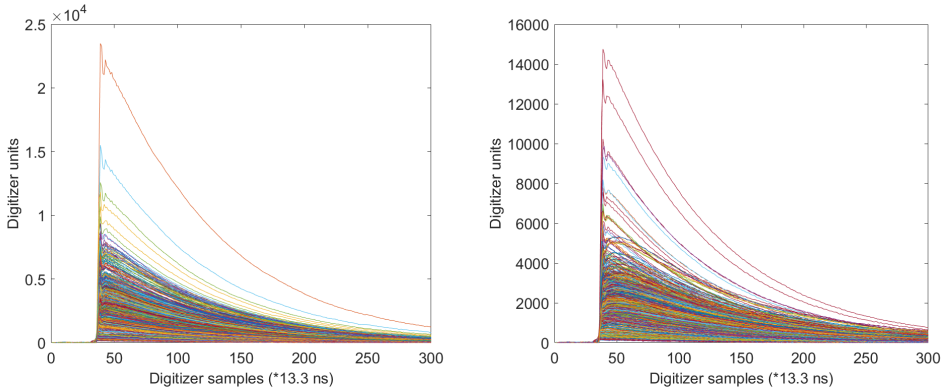

(a) (b)

Figure 5.21: Digitized (a) plastic and (b) stilbene pulses from PIXIE-4 pulse processor.

5.5.2 Measurement Campaign 1 Results

The first measurement campaign conducted at PNNL was conducted conservatively so as to preserve the integrity of the stilbene cell. Therefore, in between sample measurements instead of pumping the stilbene cells down to vacuum, the cells were pumped down to approximately 300 torr and expanded multiple times in an effort to remove the samples without compromising the integrity of the cell, this approach will be referred to as dilution and flush. Additionally, all of the radioxenon measurements were conducted close to room pressure (760 torr). For this campaign the background, ^{137}Cs, ^{133}Xe, ^{131m}Xe, ^{127}Xe, ^{252}Cf, and ^{222}Rn samples were measured for both cells.

Before any calibration measurements are conducted the background of the detectors is measured. This background measurement is used after calibration to determine the sensitivity or MDC of the coincidence system. The background was measured for approximately 14 hours and is shown in Figure 5.22. The stilbene cell has more concentrated counts at low energies than the plastic cell. The use of the lead cave helped lower the background count rate.

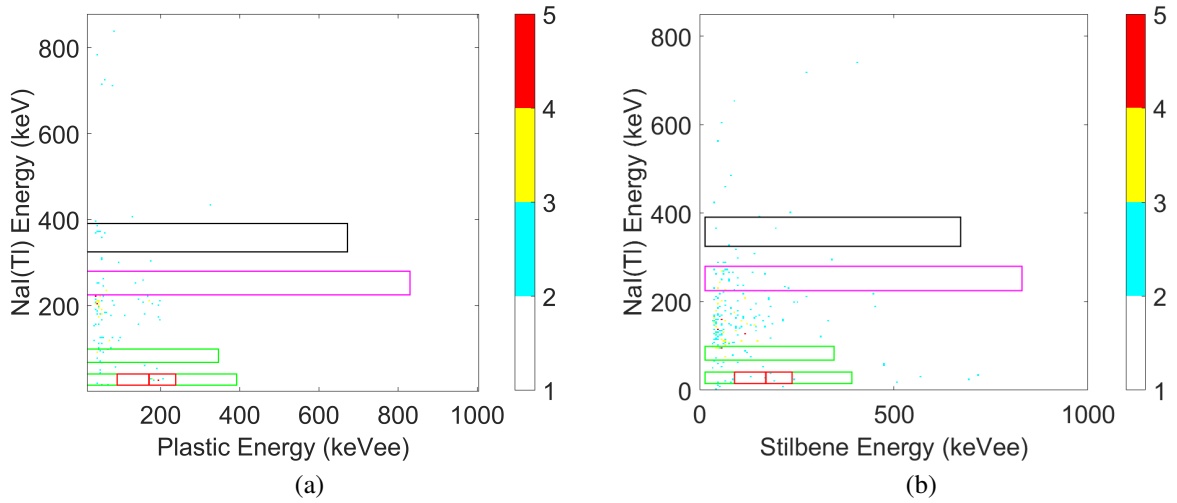

Figure 5.22: Coincidence spectra of background measurements for (a) plastic and (b) stilbene detectors.

Next, ^{137}Cs was measured to gain match the coincidence systems and was measured for approximately 4 hours. The results are shown in 5.23. Notice that the width of the line is thicker for the stilbene cell than the plastic cell suggesting degradation in the resolution of the stilbene cell. This result is different than the results shown in Figure 5.16, where the stilbene cell has a tighter line than that of the plastic cell. This broadening could be a result of spectrum smearing as discussed in [130] due to the stilbene cells improved polishing. Additionally, instead of just two pieces making up the cell, cup and end cap, now the cell consists of three pieces which could further impact the light transport to the PMT, lowering light collection efficiency.

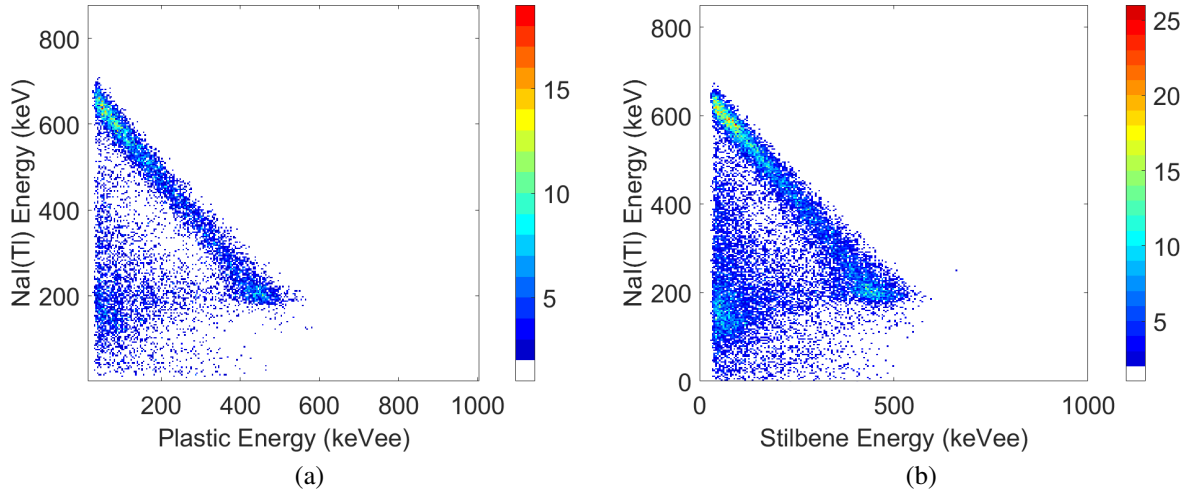

Figure 5.23: Coincidence spectra of ^{137}Cs measurements for (a) plastic and (b) stilbene detectors.

Next, ^{133}Xe was measured and the coincidence spectra results are shown in Figure 5.24. This isotope was measured for approximately 1 hour. The response of the cells is similar, showing some ^{131m}Xe contamination due to it being a medical isotope source. The count rates between the two cells are different due to the difference in cell size and the mixture of the sample, with the stilbene cell having more counts. Figure 5.25 shows the singles and coincidence spectra of the individual detectors. Figure 4.11b shows the beta spectra where the stilbene cell has a more defined low energy peak. This result could be due to differences in threshold, resolution, and photon attenuation. Additionally, the ratio between singles and coincidence counts is lower for the stilbene cell compared to the plastic cell, suggesting a decrease in gamma efficiency likely due to photon attenuation because of the increased thickness. Figure 4.11a shows the gamma spectra where there is a slight energy shift for the stilbene cell. The ratio of singles to coincidence events is again lower for the stilbene cell at both 30 and 80 keV, suggesting a decrease in beta efficiency. Whereas, at 30 keV, the beta efficiency for the plastic cell is close to 100%.

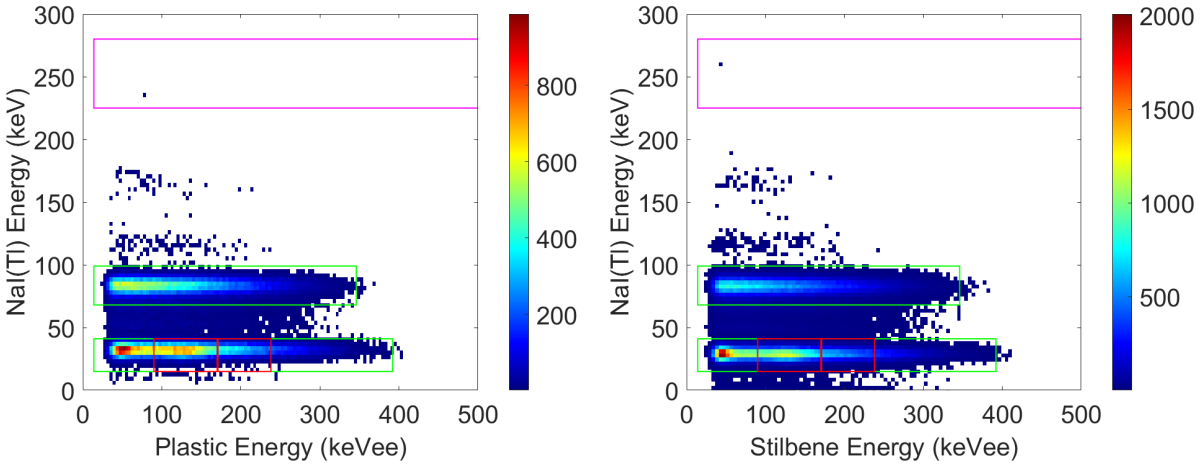

(a) (b)

Figure 5.24: Coincidence spectra of ^{133}Xe measurements for (a) plastic and (b) stilbene detectors.

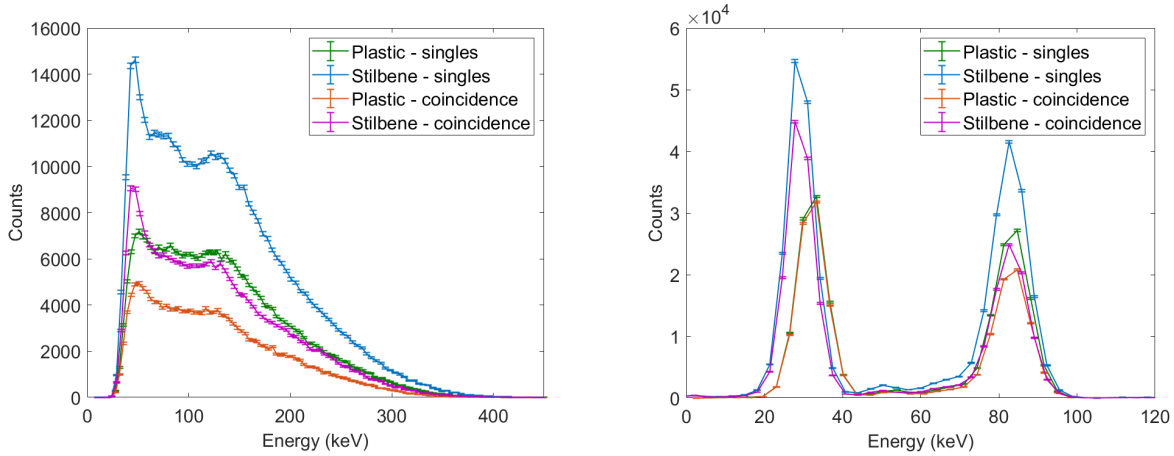

(a) (b)

Figure 5.25: Singles and coincidence spectra of ^{133}Xe measurements for the plastic and stilbene cell.

For each radioxenon measurement, a gas background measurement was taken to estimate the effectiveness of the dilution and flush process. The gas background for the ^{133}Xe measurement was acquired for approximately 16 hours and the results are shown in Figure 5.26 where the count rate for the plastic cell is less than the stilbene cell. Because list mode data was also taken during this measurement campaign, the count rate over time can be analyzed. A plot of the count

rate for the ^{133}Xe measurement is shown in Figure 5.27. The first five points represent sample measurement, after which dilution and flush occurs decreasing the count rate for the coincidence systems. Although, in Figure 5.26, it appears stilbene has worse memory effect, the decrease in count rate is more significant when examining Figure 5.27, thus suggesting an improvement in memory effect and highlighting the need to account for the amount of activity in the cell. Additionally, notice that the count rate for the stilbene cell increases with time suggesting that the plastic cell could be out gassing to the stilbene cell, gas could be trapped within the lead cave due to the leaking from the non-permanent gas line, or the gas line itself could be out gassing.

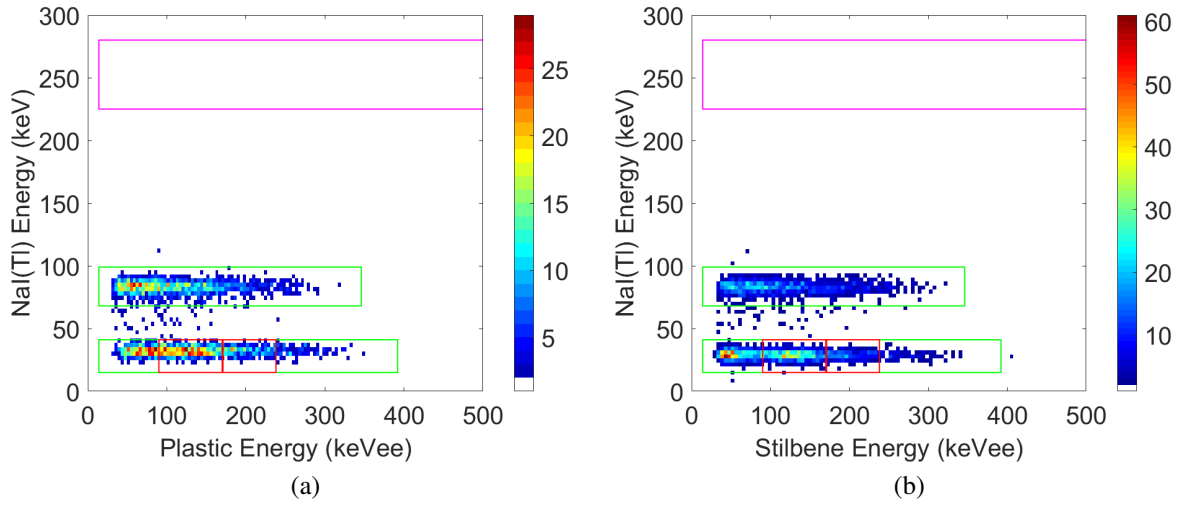

Figure 5.26: Coincidence spectra of ^{133}Xe gas background measurements for (a) plastic and (b) stilbene detectors.

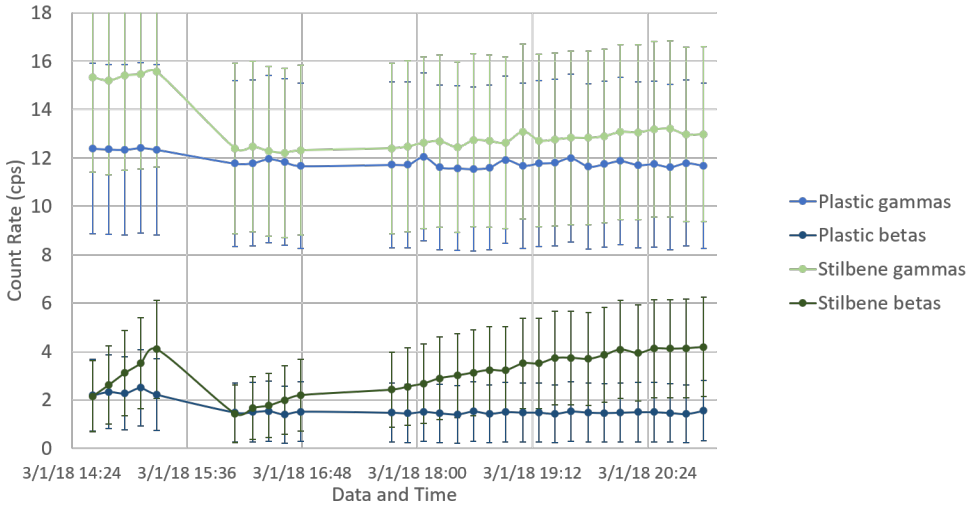

Figure 5.27: Count rate over time for ^{133}Xe measurement with list mode data acquisition. Notice that there is a larger drop in count rate for the stilbene cell compared to the plastic cell suggesting improved memory effect.

Next, ^{131m}Xe was measured for approximately 5 hours. Prior to this measurement, the tygon tubing was cut shorter in an effort to minimize memory effect in the tubing. The coincidence spectra results are shown in Figure 5.28, where there is ^{133}Xe memory effect present from the previous measurement. The cells show similar features, although the concentration of ^{133}Xe is higher for the plastic cell than the stilbene cell. Figure 5.29 shows the singles and coincidence beta spectra for the two cells. As discussed previously, ^{131m}Xe emits CE that produce peaks in the beta spectrum that can be used to analyze the resolution of the organic detector, where the singles spectra show the convolution of 129-keV and 158 through 163-keV CEs. By visual inspection of Figure 5.29, the resolution of stilbene is similar to plastic, suggesting degradation in the resolution of the stilbene cell.

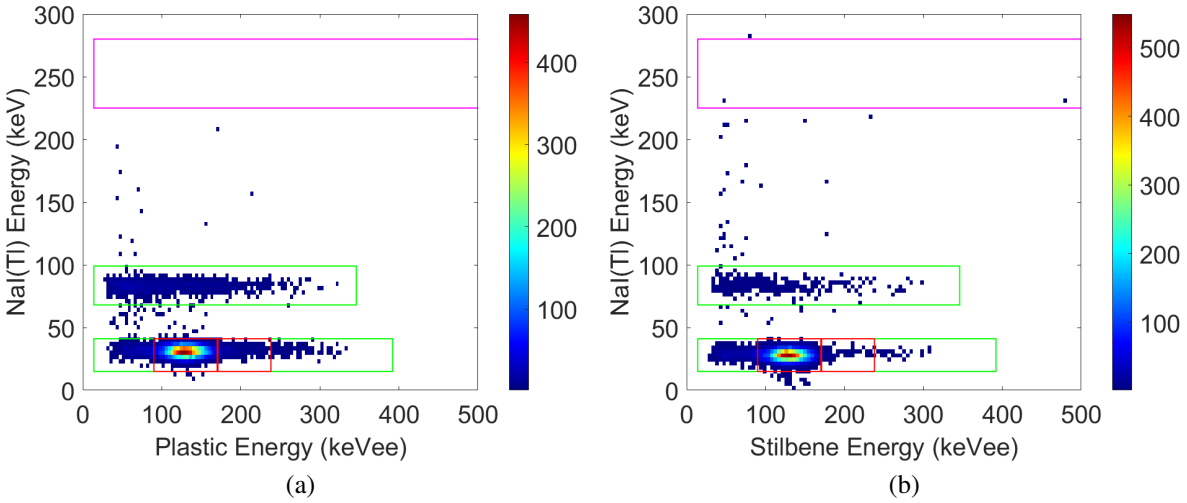

Figure 5.28: Coincidence spectra of ^{131m}Xe measurements for (a) plastic and (b) stilbene detectors.

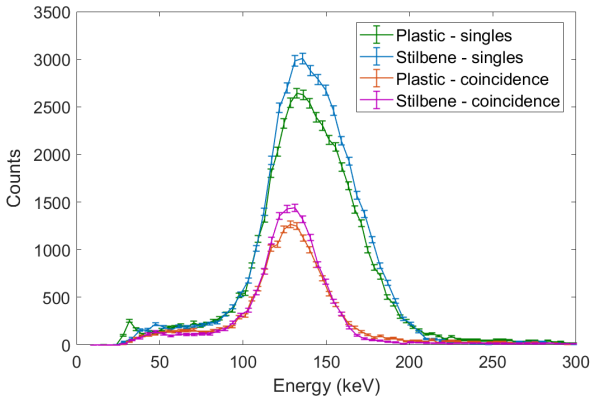

Figure 5.29: Singles and coincidence beta spectra of ^{131m}Xe measurements for the plastic and stilbene cell.

The gas background for the ^{131m}Xe measurement was taken over a weekend period lasting approximately 3 days. The results of the gas background measurement are shown in Figure 5.30. Again, the stilbene cell has less counts even though it has a higher count rate. Specifically, there is more ^{133}Xe present in the plastic spectrum compared to the stilbene spectrum, which again suggests a memory effect improvement for the stilbene cell. Again, the count rate over time is plotted in Figure 5.31. Now, the beta counts for the stilbene cell stay level instead of rising as in Figure 5.27, which could be due to the removal of the excess tubing.

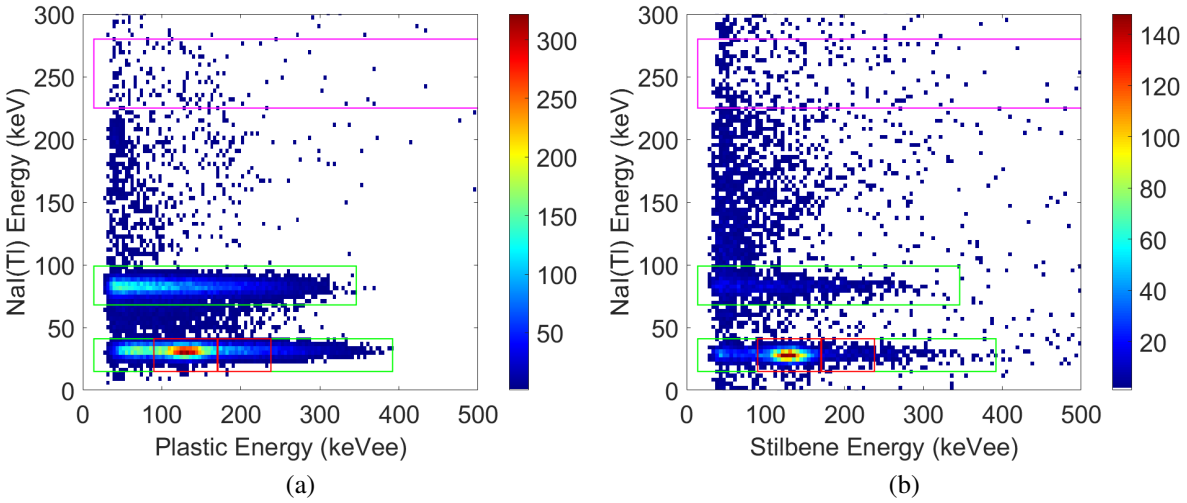

Figure 5.30: Coincidence spectra of ^{131m}Xe gas background measurements for (a) plastic and (b) stilbene detectors.

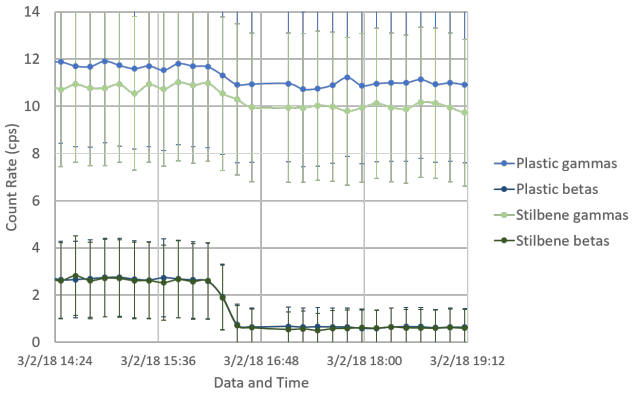

Figure 5.31: Count rate over time for ^{131m}Xe measurement with list mode data acquisition. Notice that there is a larger drop in count rate for the stilbene cell compared to the plastic cell suggesting improved memory effect.

Next, ^{127}Xe was measured for approximately 19 hours. This source has a complex decay scheme as discussed in [131, 132]. Therefore, a variety of features show up in the coincidence spectrum as seen in Figure 5.32. The plastic spectrum has a feature around 80 keV that is not as present in the stilbene spectrum, due to the ^{133}Xe memory. Additionally, the beta energies between 150-200, are highly concentrated in the plastic cell where the stilbene cell has a wider range. This result could be due to the resolution as these energies broadening the relevant energy peaks. However, due to the

low statistics, this measurement was not able to be used to analyze the resolution of the detectors.

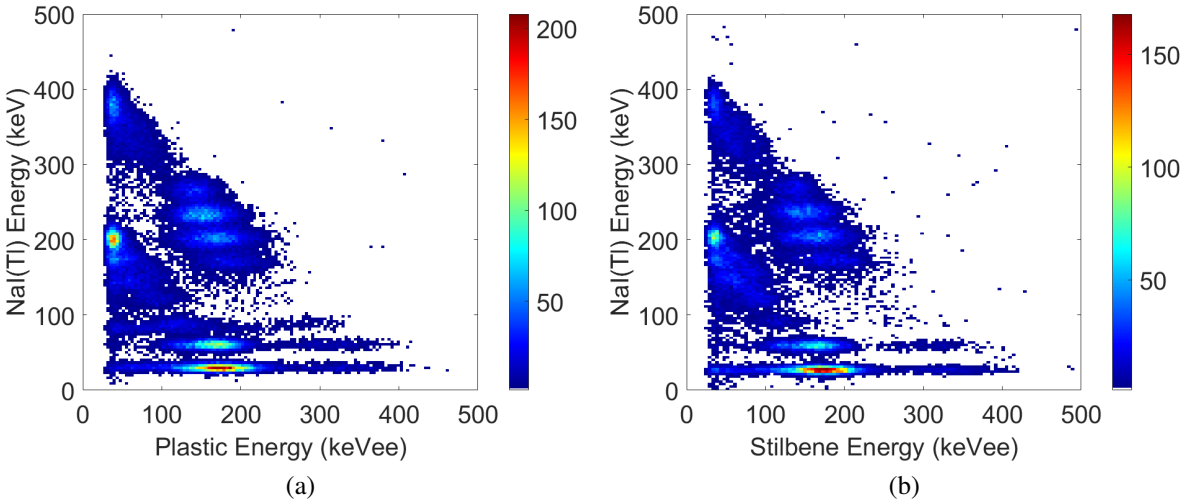

(a) (b)

Figure 5.32: Coincidence spectra of ^{127}Xe measurements for (a) plastic and (b) stilbene detectors.

A short memory gas background measurement, approximately 4 hours, was taken after the ^{127}Xe measurement. The results are shown in Figure 5.33 where the background is significantly reduced for both cells, but almost negligible for the stilbene cell. This result further highlights the drastic memory effect improvement, especially since the cells were never fully pumped down to vacuum.

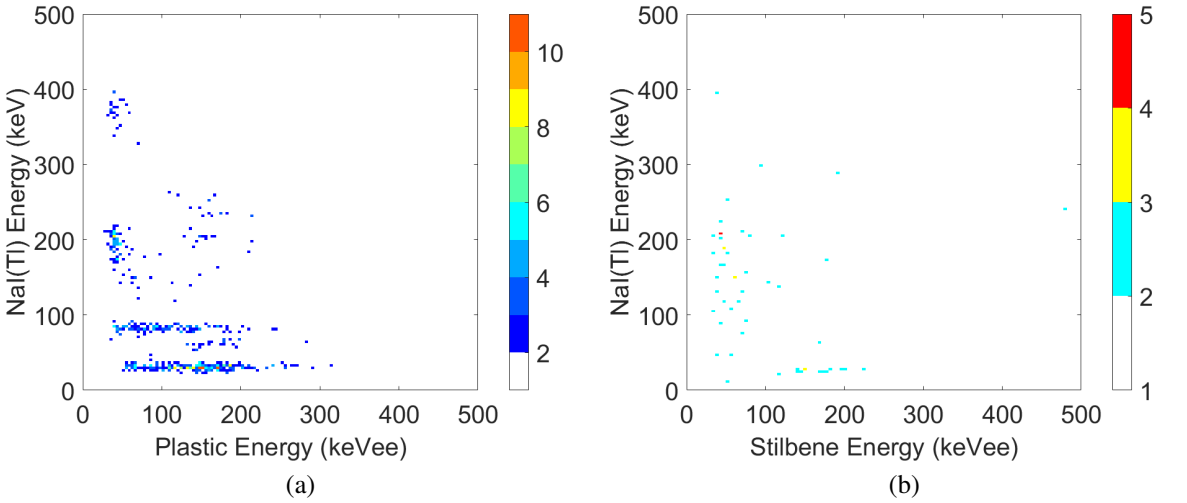

(a) (b)

Figure 5.33: Coincidence spectra of ^{127}Xe gas background measurements for (a) plastic and (b) stilbene detectors.

The next source measured was ^{252}Cf. The purpose of this measurement was to test the PSD parameters for the XIA output. Because the pulses are stretched due to impedance mismatch on the PIXIE inputs along with the trapezoidal filtering of the pulse, there was some thought that the pulses may not contain enough information to do PSD. As shown in Figure 5.34, the PSD is not great due to the overlap of neutron and photons ratios; however, this separation is enough to assume alpha/beta PSD is capable with XIA electronics. PSD was performed using the digital charge comparison technique [133–138], where the ratio of the tail integral of the pulse to the total integral of the pulse is used to discriminate between the different particle types. The start time of the tail pulse and the stop time of both pulses were optimized.

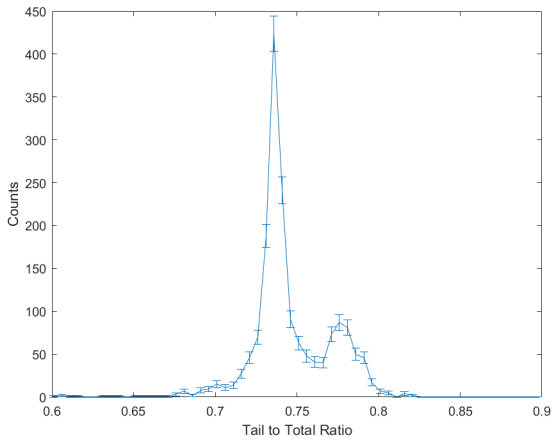

Figure 5.34: Tail to total ratio versus counts for ^{252}Cf measurement where there is some separation between the neutron and photon events but shows that the cell is capable of PSD.

Next, a series of ^{222}Rn measurements were taken. The results shown in Figure 5.35 were from a one-hour measurement taken 30 minutes after sample injection. The features present in the spectra are due to the ^{222}Rn daughter products, ^{214}Pb and ^{214}Bi.

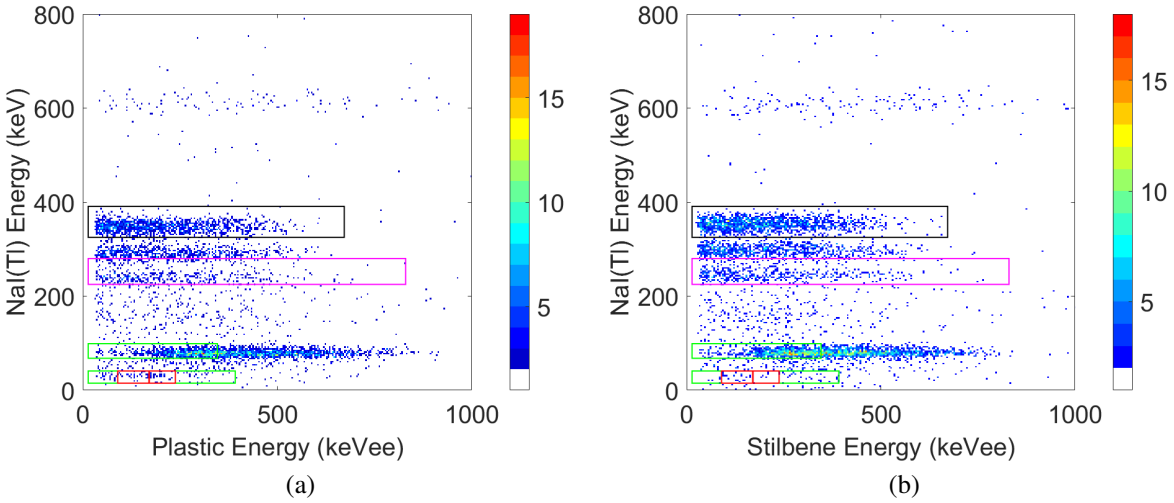

(a) (b)

Figure 5.35: Coincidence spectra of ^{222}Rn measurements for (a) plastic and (b) stilbene detectors.

Because it was shown previously that the cell has PSD capabilities, this was applied to the radon measurement. Figure 5.36 plots the tail-to-total ratio versus the integral calculated by the data acquisition system. In this figure, there is good separation between the alpha and beta/gamma events. Figure 5.37 shows digitized pulse for alpha and beta/gamma events. Because the pulses are filtered, the shape of the second peak of the pulse has a different shape instead of the tail having more light. Therefore, extra care must be taken in optimizing the start of the tail to incorporate this effect due to pulse filtering.

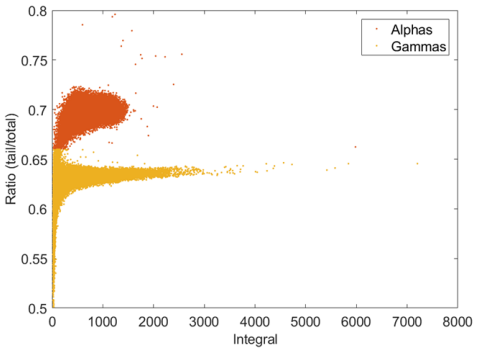

Figure 5.36: Tail to total ratio versus pulse integral for ^{222}Rn measurements where there is good separation between alpha and beta/gamma events.

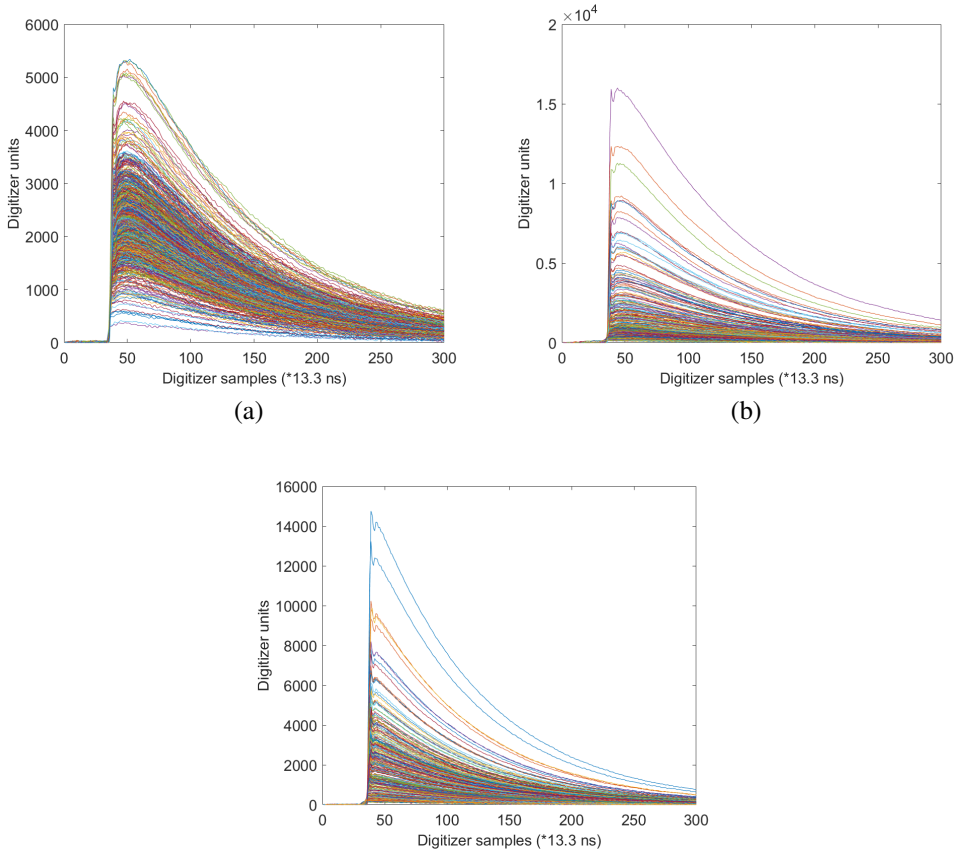

Figure 5.37: Digitized stilbene pulses for (a) alpha, (b) neutron, and (c) beta/gamma events using the tail to total ratio. Notice that the alpha events have more light in the hump than the beta/gamma events due to the filtering of the pulse.

Using the ratio to discriminate the particles, the components that make up the beta singles spectrum are shown in Figure 5.38. The three alpha energies due to ^{222}Rn (5.5 MeV), ^{218}Po (6 MeV), and ^{214}Po (7.7 MeV) show up as convolved peaks in the alpha component of the beta spectrum, where the light output is not proportional requiring a separate alpha calibration. However, this measurement has shown that PSD can separate the two components and could lead to radon mitigation.

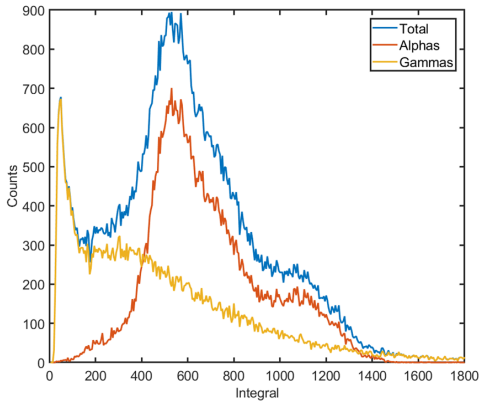

Figure 5.38: Stilbene beta spectrum with alpha and beta/gamma contributions identified using PSD.

Next, a strong ^{133}Xe sample was measured for approximately 9 hours. The coincidence spectra for this measurement are shown in Figure 5.39. As shown, over one million coincidence counts were registered in ROI 3 (30 keV), and there is still some ^{131m}Xe present in both samples due to its relatively long half-life. The purpose of this high activity measurement was to analyze the memory effects of the two cells.

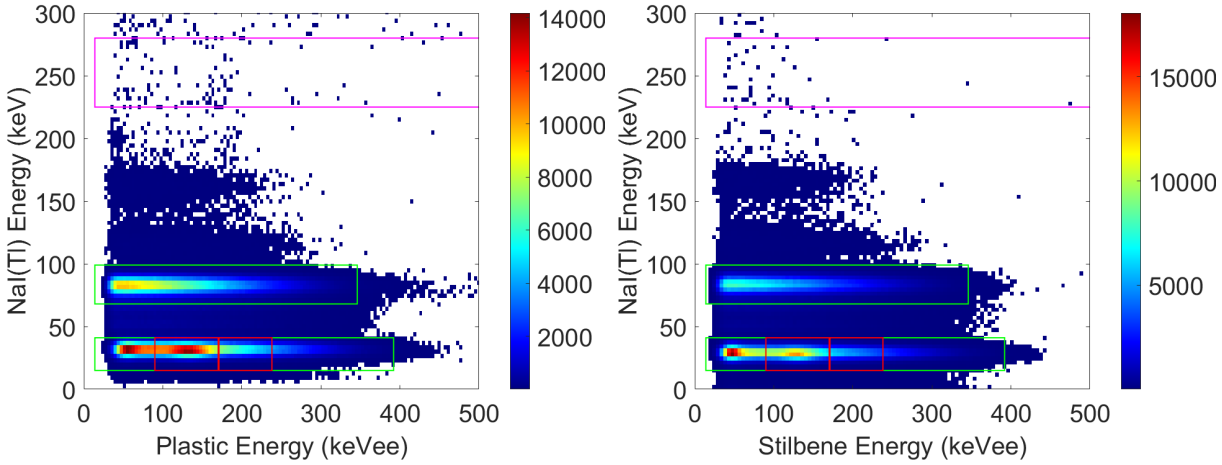

(a) (b)

Figure 5.39: Coincidence spectra of ^{133}Xe measurements for memory effect analysis for (a) plastic and (b) stilbene detectors.

Figure 5.40 shows the 15-hour gas background measurement of the cells. Again, there is some

^{131m}Xe contamination which is more apparent in the plastic cell than the stilbene cell. Because a proper pump and flush was not done in between each of the sample measurements, the results of these measurements could not be used to quantify the memory effect.

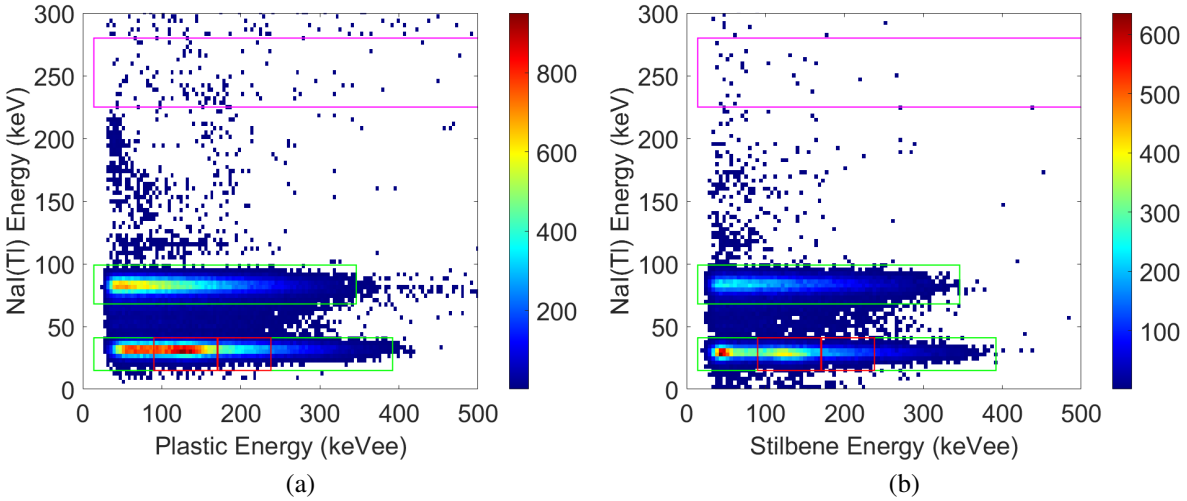

Figure 5.40: Coincidence spectra of ^{133}Xe gas background measurements for memory effect analysis for (a) plastic and (b) stilbene detectors.

To finish up the measurement campaign, ^{137}Cs was measured for approximately 22 hours to account for any gain shifts during the two-week experiment period. This measurement also contains ^{133}Xe background due to the previous memory effect measurement. The coincidence spectra are shown in Figure 5.41. The ^{133}Xe gas background is more apparent in Figure 5.41a than Figure 5.41b, again suggesting improved memory effect for the stilbene cell.

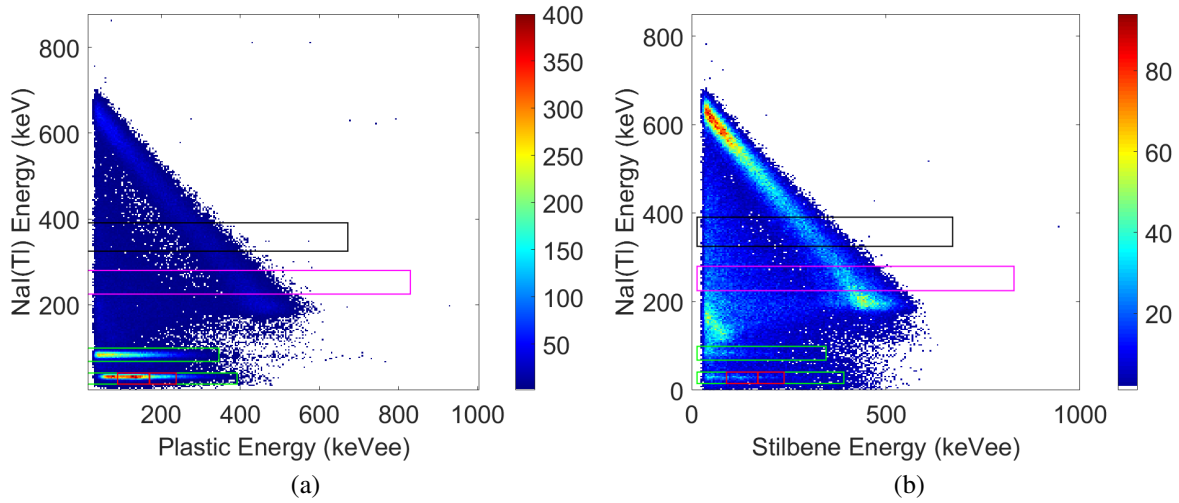

Figure 5.41: Coincidence spectra of ^{137}Cs and ^{133}Xe gas background measurements for (a) plastic and (b) stilbene detectors.

In addition to not pumping and flushing the cells, the gas samples were back-filled with air instead of a carrier gas, such as nitrogen or stable xenon. Thus, the concentration of the samples was different for each cell due to sample mixing after the gas was introduced in the cell. This difference in sample concentration along with the difference in cell volume, makes it difficult to directly compare the results of the first measurement campaign. This error in sample mixing is resolved in the second measurement campaign. However, these results helped improve the second measurement campaign presented in the next section.

A background measurement was conducted in between the two measurement campaigns, lasting for approximately 55 days. Figure 5.42 shows the results of this measurement where the plastic spectrum, Figure 5.42a, has memory effect present from both ^{127}Xe and ^{131m}Xe. In contrast to the stilbene spectrum, which appears to have some memory effect from ^{127}Xe but none from ^{131m}Xe. In either case, the count rate is low enough to be insignificant for the second measurement campaign.

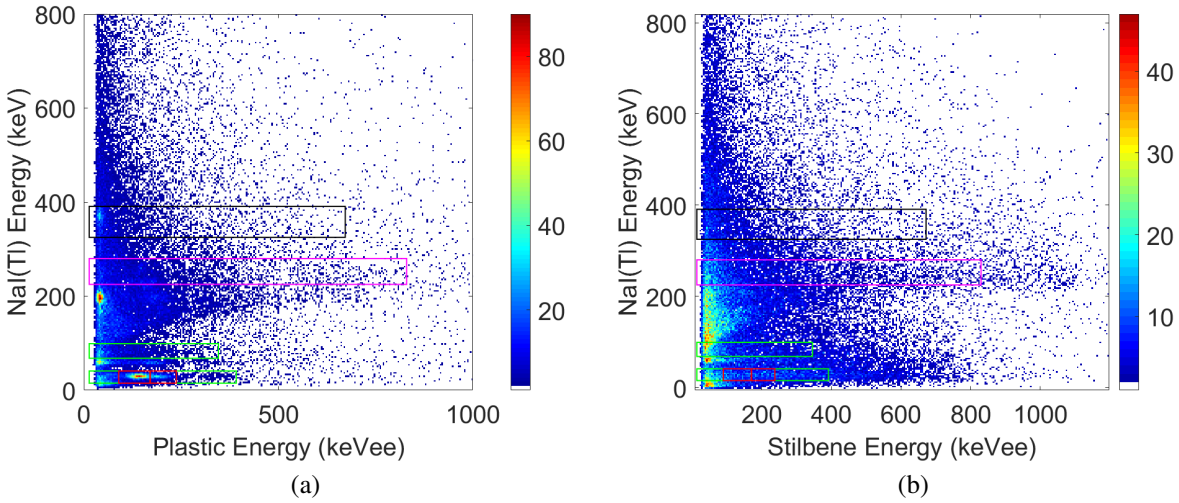

Figure 5.42: Coincidence spectra of background measurements for (a) plastic and (b) stilbene detectors for 55 days after the end of campaign 1.

5.5.3 Measurement Campaign 2 Results

The results presented in this section are from the second measurement campaign conducted at PNNL, after discovering the limitations in the first campaign. For these measurements a true pump and flush was done between sample measurements where the cell was flushed with air and pumped down to vacuum, three times. Therefore, the gas background measurements are not shown in this section although, the plastic cell does have some memory effect throughout the measurement campaign. For this second campaign, all four radioxenon isotopes of interest were measured along with radon. Each radioxenon sample used stable xenon as the makeup gas, except ^{135}Xe which used nitrogen gas. All of the measurements were taken at pressures between 200-335 torr.

The ^{137}Cs measurement shown in Figure 5.43 was taken at the end of the second measurement campaign. A horizontal cut of the coincidence spectra projected onto the x-axis is shown in Figure 5.44. The stilbene spectrum has a broader peak than the plastic spectrum, likely due to differences in the light output of the stilbene cell walls versus the two endcaps. The endcap closest to the PMT will have the best resolution due to light capture efficiency and the endcap at the other end will have lower resolution due to less light capture efficiency. This light output difference produces three

overlapping Compton edges in the ^{137}Cs spectrum, degrading the stilbene resolution.

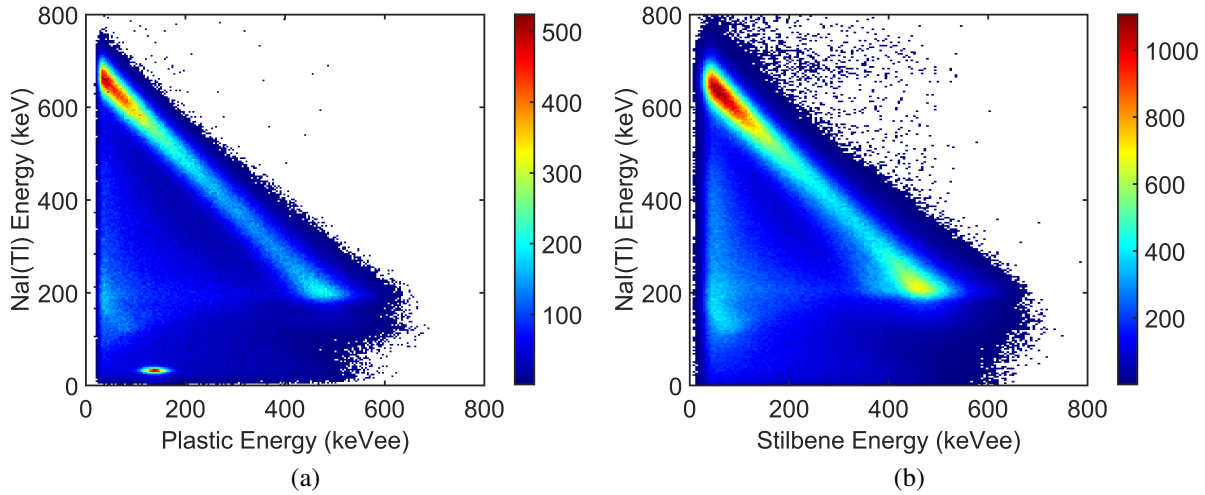

Figure 5.43: Coincidence spectra of ^{137}Cs measurements for (a) plastic and (b) stilbene detectors.

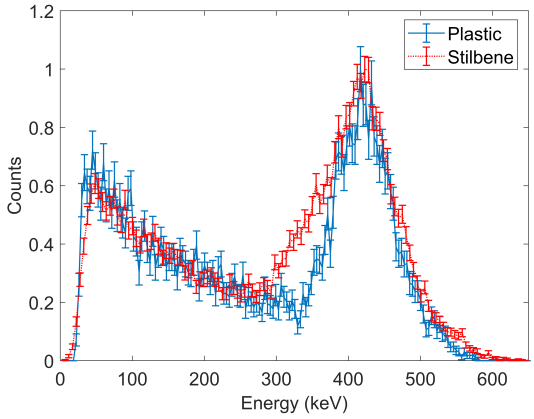

Figure 5.44: Beta spectrum projection of ^{137}Cs measurement in plastic (green) and stilbene (blue) cells, where the stilbene cell has a broader peak, suggesting different light output in the cell walls versus the endcap.

The first radioxenon sample measured was ^{135}Xe for approximately 6 hours. The measured coincidence spectra from the plastic and stilbene cells are shown in Figure 5.45, where both cells produce similar features for the ^{135}Xe ROI. Figure 5.46 shows the beta singles and coincidence spectra of the plastic and stilbene cells where the endpoint energies align. Additionally, the

coincidence counts in the stilbene cell are less than those in the plastic cell showing a decrease in gamma efficiency for the stilbene cell.

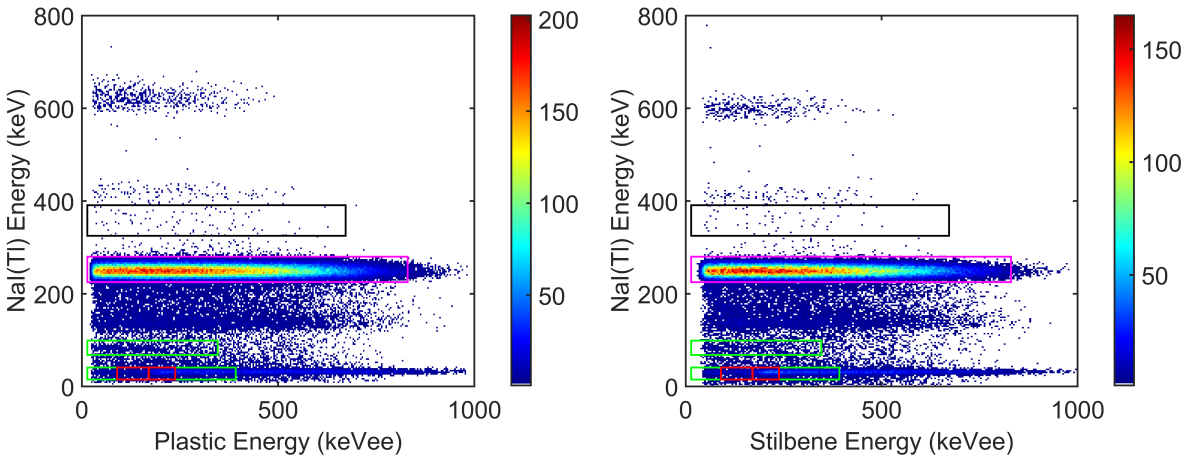

Figure 5.45: Coincidence spectra of ^{135}Xe measurement in (a) plastic and (b) stilbene cells, where the color bar denotes counts. The cells produce similar features with the stilbene cell detecting slightly less counts.

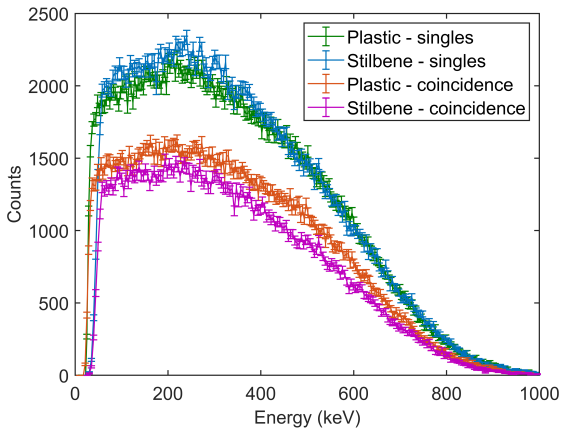

Figure 5.46: Beta singles and coincidence spectra of ^{135}Xe measurement in plastic and stilbene cells, showing a similar shape for the beta spectrum between the cells. The ratio of singles to coincidence counts is less for the stilbene cell suggesting a decrease in gamma efficiency due to the thickness of the stilbene cell and the decreased solid angle.

The next radioxenon sample measured was ^{133}Xe. This sample was measured for approximately 3 days and was used to analyze the memory effect of the samples. The measured coincidence

spectrum for the cells are shown in Figure 5.47 where both cells produce similar features for the ^{133}Xe ROIs. This measurement is a purer sample of ^{133}Xe in contrast to Figure 5.24 where ^{131m}Xe contamination was present.

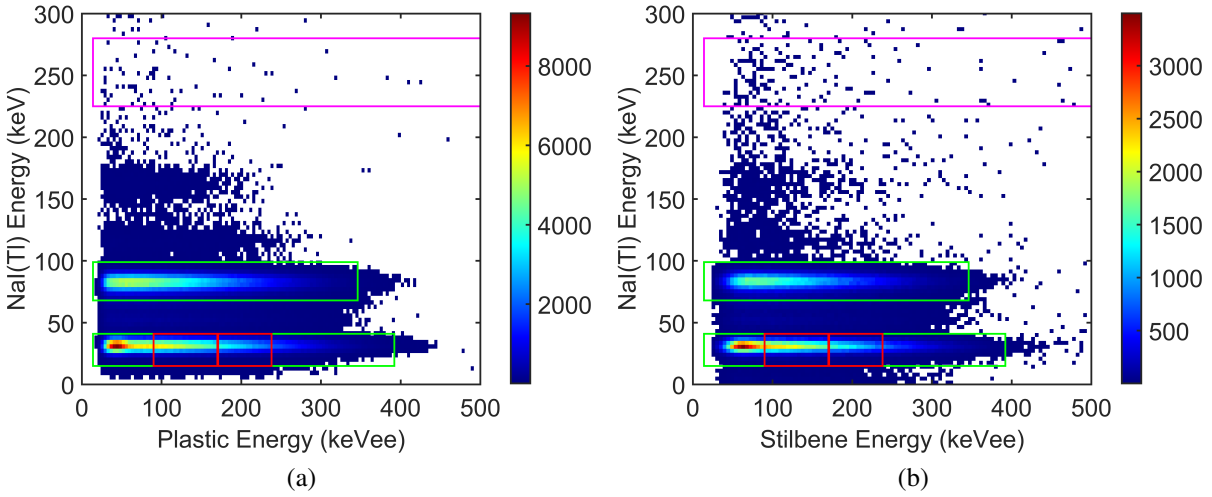

Figure 5.47: Coincidence spectra of ^{133}Xe measurements for (a) plastic and (b) stilbene detectors. The cells produce similar features apart from the 45-keV peak for the stilbene cell extending farther in the ROI than the plastic cell.

The next radioxenon sample measured was ^{133m}Xe, which contains the decay product ^{133}Xe. The coincidence spectra are shown in Figure 5.48, where both cells again produce similar features, containing concentrated counts in the ^{133m}Xe ROI in addition to the ^{133}Xe ROIs. The 30 keV gated beta coincidence spectra are shown in Figure 5.49, where the 45 keV peak is more prominent for the plastic cell. However, the 198-keV conversion electron peak is prominent for both cells. Figure 5.50 plots the count rate over time for the experiment. At the beginning of the measurement there is an exponential drop in counts for the stilbene cell and a growth in counts for the plastic cell, suggesting leakage from the stilbene cell into the cave. The average leak rate for the experiment of the plastic and stilbene cells are -0.022 counts per second and -0.080 counts per second, respectively. Leakage of the sample from the cells into the cave of the experiment results in extra gamma singles counts which impact the efficiency analysis. This loss in sample through leakage effects the beta detection efficiency; the stilbene cell has 4-times larger average sample loss than the plastic cell.

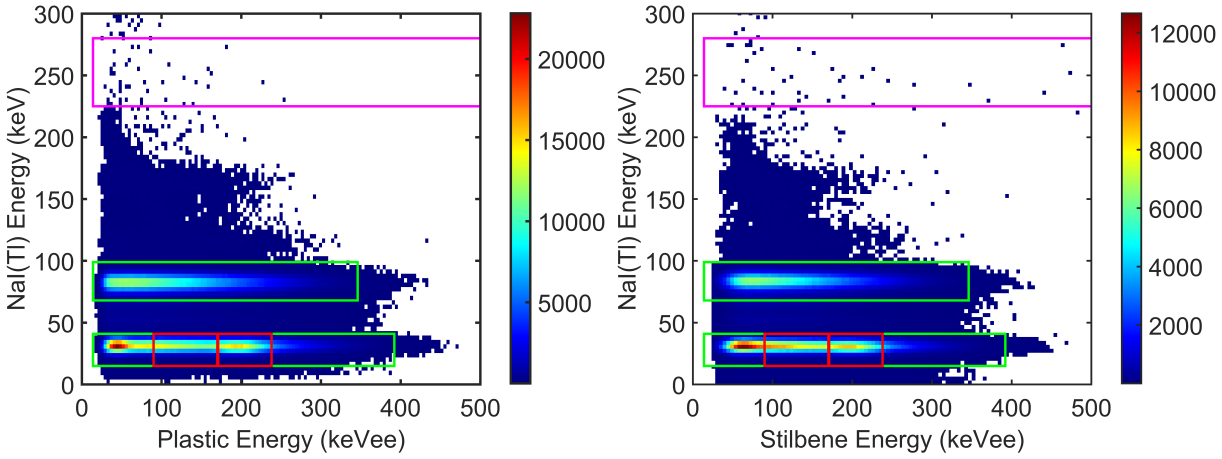

Figure 5.48: Coincidence spectra of ^{133m}Xe with ^{133}Xe measurements for (a) plastic and (b) stilbene detectors. Again, the 45-keV peak for the stilbene cell extends farther in the ROI than the plastic cell, suggesting peak broadening.

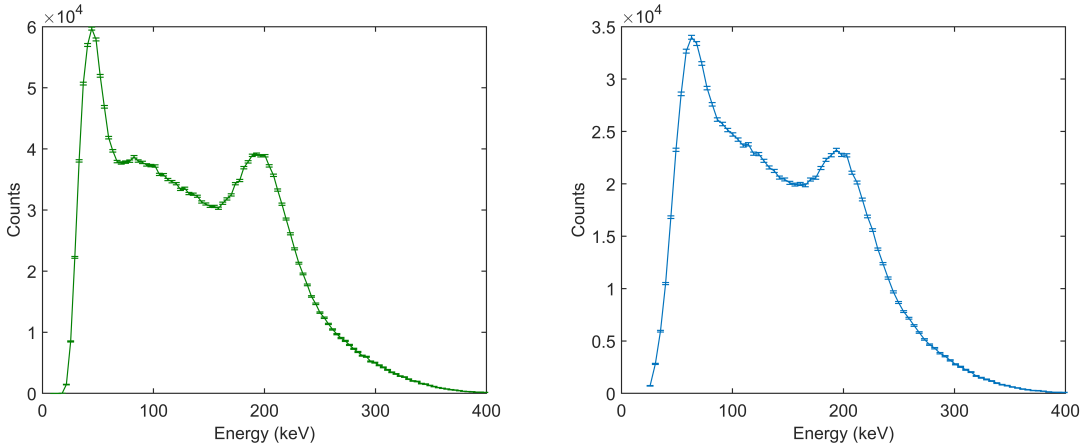

Figure 5.49: Gamma gated beta coincidence spectra of ^{133m}Xe and ^{133}Xe in (a) plastic and (b) stilbene cells. The resolution of the 45-keV peak for the stilbene cell is broadened compared to the plastic cell.

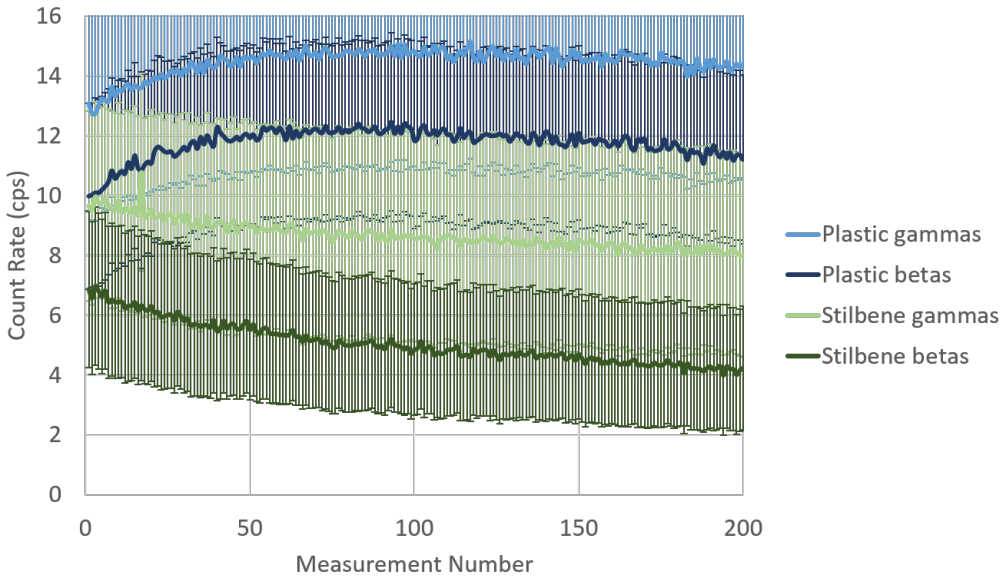

Figure 5.50: Count rate over time for ^{133}Xe measurement with list mode data acquisition. The stilbene cell has a lower count rate and lower rate of count decrease compared to plastic. The decrease in count rate at the beginning of the experiment for the stilbene cell suggests leakage into the cave.

The final radioxenon sample measured was ^{131m}Xe. This sample was measured approximately 20 days after ^{133m}Xe/^{133}Xe allowing for approximately four ^{133}Xe half-lives to occur. The measurement lasted approximately 4 days and the coincidence spectra results are shown in Figure 5.51, where the cells produce similar features for the ^{131m}Xe ROI, centered around 129-keV. However, the plastic cell exhibits memory effect from the previous ^{133m}Xe/^{133}Xe measurement, where the stilbene cell does not.

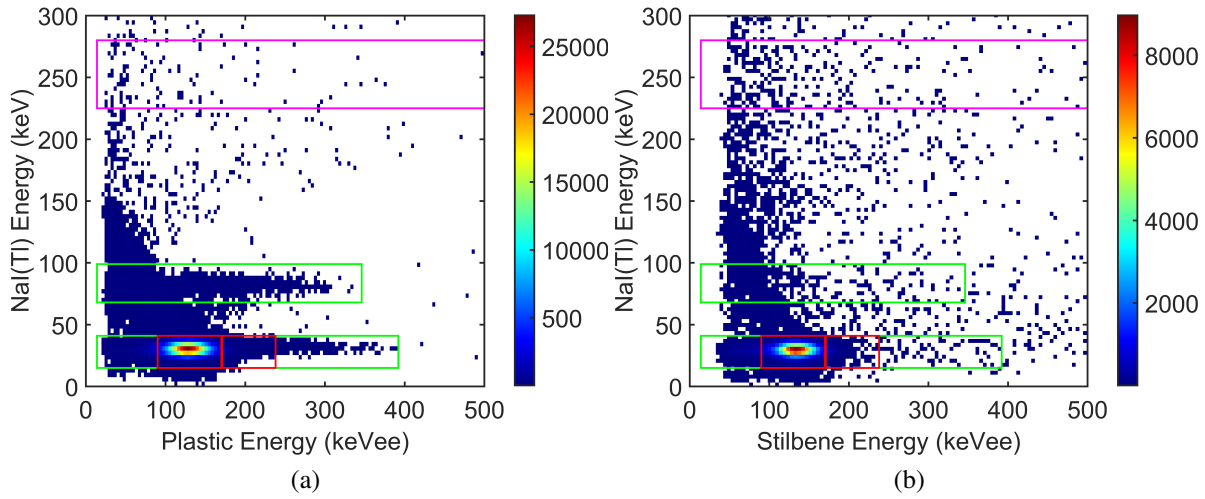

Figure 5.51: Coincidence spectra of ^{131m}Xe measurements for (a) plastic and (b) stilbene detectors. The ROIs bounds for the cells are similar with the plastic cell exhibiting memory effect.

5.5.4 Detector Characterization and Comparison

As shown in the previous sections, the stilbene and plastic cells produce similar ROI features for the various radioxenon samples. Focusing on the metastable isotopes, the ROI bounds on the x-axis suggest that the plastic and stilbene cells have similar energy resolutions. Figure 5.52 shows the ^{131m}Xe beta coincidence spectra for the two cells, where the full width at half maximum (FWHM) is slightly smaller for the stilbene cell (39.9 keV) compared to the plastic cell (42.1 keV). We expect the stilbene cell to have improved resolution over the plastic cell [133, 139], therefore these results suggest that improvements to the light collection are needed for the stilbene cell. The stilbene cell consists of a hollow cylinder with two flat, circular endcaps. The plastic cell is fabricated as a tube with a rounded end, a design which better directs the light towards the PMT. A similar geometric design for the stilbene cell would likely improve the resolution of the detector.

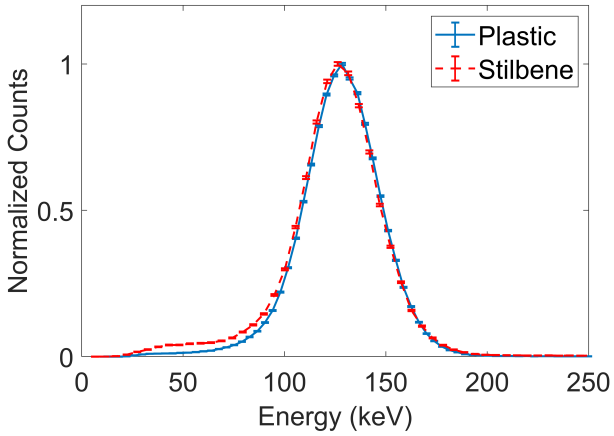

Figure 5.52: Beta coincidence spectrum comparison of plastic (green) and stilbene (blue) for ^{131m}Xe measurement, where the 129 keV conversion electron peak is used to quantify the detector resolution and is slightly better for the stilbene cell.

The ROI locations are based on the energy calibration and the bounds are based on the energy resolution. Once the ROIs have been established, the efficiency of the individual detectors and the coincidence system can be analyzed. Table 5.1 shows the coincidence efficiency values for each coincidence system, plastic versus stilbene used with NaI(Tl), calculated using the absolute efficiency calibration method discussed in Chapter 3. The average decrease in efficiency for the stilbene cell is 15%, compared to the plastic cell. This efficiency decrease can be attributed to loss in light collection, higher energy threshold, increased attenuation of low energy X-rays from the thicker stilbene cell walls, solid angle effects, and loss of sample due to leaking from the plastic tubing gas line for the stilbene cell. The stilbene cell is approximately 1 cm longer and 1 mm thicker than the plastic cell. Due to the increased length of the stilbene cell, the solid angle of the experiment is decreased. MCNPX-PoliMi simulations of the stilbene cell at various positions beyond the well of the NaI(Tl) detector were conducted to analyze the change in efficiency. For the estimated position of the experiment, the simulation results show an approximate 20% decrease in gamma efficiency, accounting for an average 8% of the stilbene coincidence efficiency decrease. Although the detection efficiency is lower than that of the plastic cell, it is reasonable when compared to a detector system using the PIPSBOX, where the efficiency ranges from 20-55% [9] compared to

38-43% with the stilbene and NaI(Tl) detectors used for this study.

Table 5.1: Regions of interest coincidence efficiencies

Region of Interest	Plastic	Stilbene
^{135}Xe	0.580 ± 0.020	0.420 ± 0.014
^{133}Xe (80 keV)	0.627 ± 0.019	0.429 ± 0.013
^{133}Xe (30 keV)	0.537 ± 0.025	0.436 ± 0.020
^{133m}Xe	0.546 ± 0.019	0.384 ± 0.028
^{131m}Xe	0.567 ± 0.002	0.425 ± 0.003

Using the background measurement, the MDC was estimated using Equation 3.6. A similar approach to that discussed in [140] was used to simplify the MDC calculation for both systems: 1) it is assumed that no interference from radon or other radioxenon isotopes occur simplifying Equation 3.7 to only background counts where the background counts are scaled for the acquisition time, 2) T_C, T_P , and $T_A$values were 8 hours, 5.45 hours, and 12 hours, similar to that of the ARSA detector [46], 3) the coincidence branching ratios used are from [38], and 4) the sample volume for the stilbene cell was scaled 20% to account for the increase in cell volume. Table 5.2 shows the results of this calculation for the plastic and stilbene cells. The MDC values for the stilbene cell are higher compared to the plastic mainly due to the decreased efficiency of the cell.

Table 5.2: Regions of interest minimum detectable concentrations based on background measurement.

Region of Interest	Plastic	Stilbene
^{135}Xe	0.376 ± 0.004	0.569 ± 0.005
^{133}Xe	0.137 ± 0.002	0.218 ± 0.002
^{133m}Xe	0.081 ± 0.002	0.144 ± 0.002
^{131m}Xe	0.089 ± 0.002	0.160 ± 0.002

5.5.5 Memory Effect Analysis

As discussed previously, memory effect is a major limiting factor in the use of plastic for radioxenon measurements because it increases subsequent measurement backgrounds, decreasing detection sensitivity. Therefore, to analyze the improvement in using stilbene, both cells were subjected to the same radioxenon samples and pump-and-flush cycles. As mentioned, the ^{133}Xe measurement

of campaign 2 was used to quantify the memory effect of the two cells. Figure 5.53 shows the coincidence spectrum of the gas background for the ^{133}Xe measurement. The memory effect was quantified by calculating the ratio of the activity of the sample and the gas background measurement at the start of the ^{133}Xe sample measurement. This analysis resulted in 4.5% activity remaining in the plastic cell compared to 0.043% activity remaining in the stilbene cell, improving the memory effect by a factor of 100. Therefore, the stilbene cell has significantly less memory effect than the plastic cell; the source of radioxenon in the stilbene cell is mainly attributed to the tygon tubing and/or the Macor endcap.

In the field, gas background measurements are taken after radioxenon measurements to account for memory effect. However, reducing the memory effect eliminates the need for gas background measurements. Therefore, IMS stations would have extended time to measure atmospheric samples, further increasing the sensitivity of the verification regime.

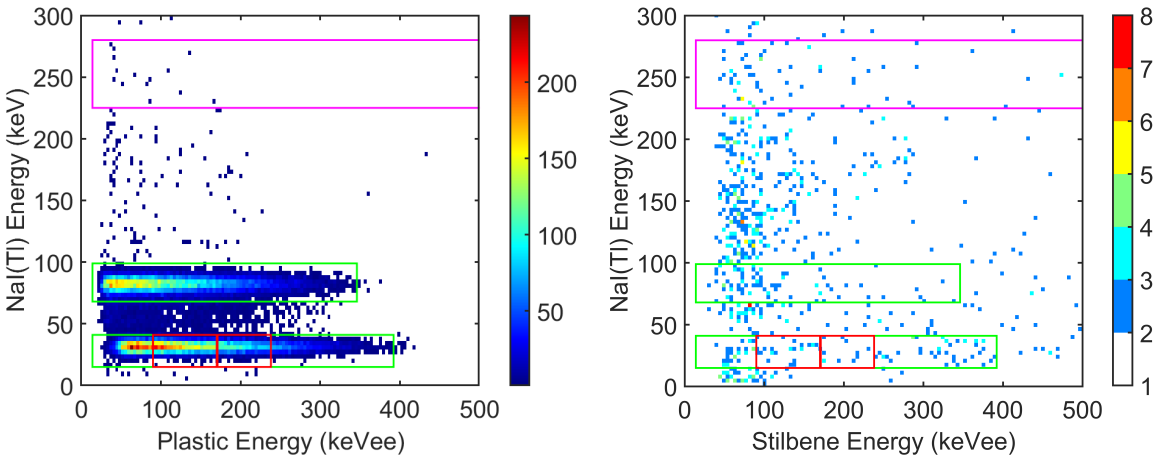

Figure 5.53: Coincidence spectra of ^{133}Xe gas background measurements for (a) plastic and (b) stilbene detectors.

5.5.6 Radon Mitigation

As shown previously, the stilbene cell is capable of discriminating between alphas and gamma/beta events. For the second measurement campaign, a longer radon measurement was taken to get better

statistics for the analysis. Figure 5.54a shows the tail-to-total ratio versus energy measured with a radon sample, where there is good separation between the beta and alpha particles. Also, the contributions from the different alpha energies are also present as concentrated circles in the plot. Figure 5.54b, again shows the beta singles spectrum of the stilbene cell and the separated alpha and beta/gamma components, where the alpha events account for 49% of the counts.

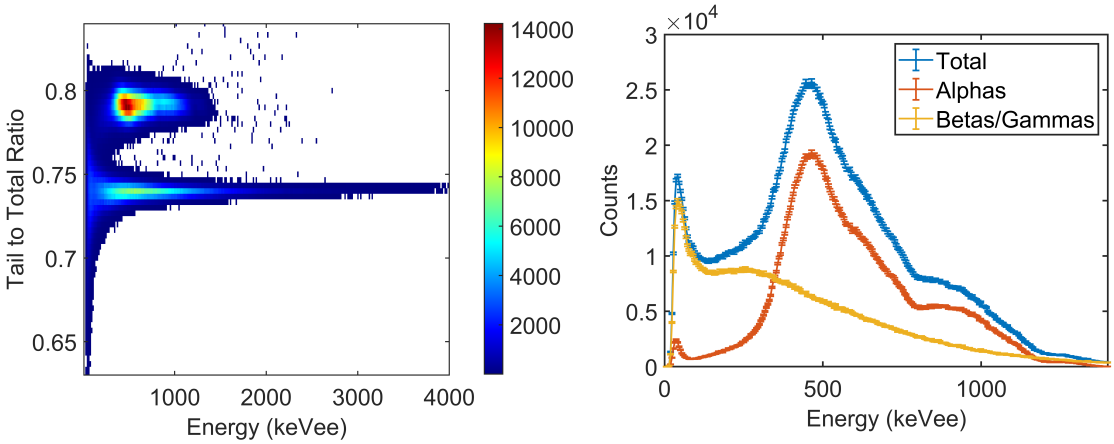

Figure 5.54: PSD plots for stilbene cell; (a) energy versus tail to total ratio of radon sample and (b) beta singles spectrum with alpha (orange) and beta (yellow) components separated using PSD.

The PSD-identified alpha events can be used to tag and reject related beta-gamma coincidence events based on the radon decay chain. The isotope of interest for this analysis was ^{214}Bi, whose daughter product, ^{214}Po , emits alphas with a half-life of 160 μs. Therefore, the timing window was optimized to 500 μs, to maximize ^{214}Bi rejection and account for detector electronics. Thus, events occurring within 500 μs before an alpha event are tagged and subtracted from the coincidence spectrum. Figure 5.55a shows the total coincidence spectrum of the radon measurement. Figure 5.55b shows the gamma projection of the coincidence and alpha subtracted spectra, where the rejected events represent 52% of the counts in the ^{214}Bi 609-keV peak and 13% of the counts in the ^{214}Pb 352-keV ROI. This method reduces the total coincidence counts by a relative 23%, removing scattering events as well as 609-keV events. Applying the method to a radon sample having a lower activity produced similar results, a relative 22% decrease in total coincidence counts. The 352-keV

ROI is used to quantify the radon interference in the sample. Applying this event rejection technique results in an estimated 1% decrease of the ^{135}Xe MDC for this coincidence system; ^{135}Xe is most affected by radon interference. Although, this improvement is small for radioxenon detection, this technique would be beneficial for single radiation detectors looking to discriminate between alphas and betas, such as nuclear facilities monitoring or dosimetry. Additionally, by identifying alpha emissions, this technique could be used to better quantify radon interference.

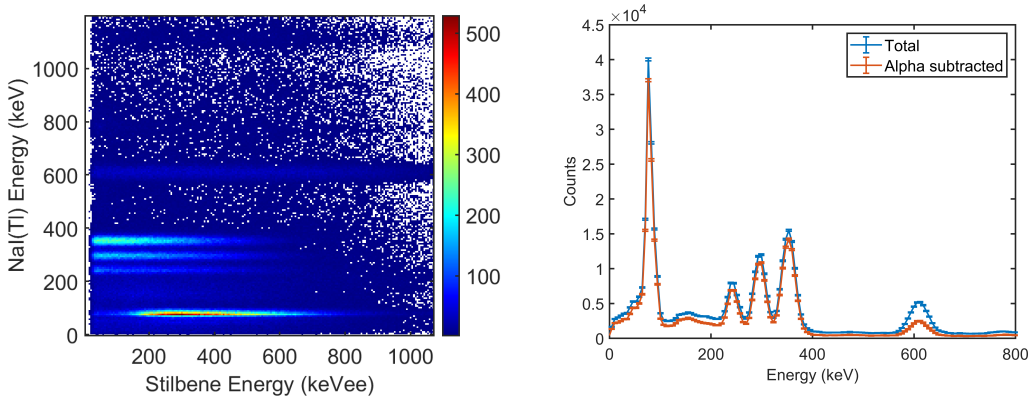

(a) (b)

Figure 5.55: Radon plots for stilbene cell; (a) radon coincidence measurement for stilbene cell and (b) Gamma coincidence events for all detected coincidences (blue) and alpha related events subtracted (orange). The tagging and rejection of alpha related events results in a relative 23% decrease in counts.

5.6 Conclusions

A stilbene cell has been designed, manufactured, and tested for radioxenon detection. A benefit of replacing plastic with stilbene is the insignificant memory effect of the stilbene cell. This minimal memory effect could improve the sensitivity of the monitoring regime by using the time currently used to count the memory effect to count the sample longer. The cell was calibrated alongside a plastic scintillator cell and shows slightly improved resolution, little-to-no memory effect, and PSD capabilities. The prototype used for these experiments maintained vacuum stability, while remaining intact. The efficiency of the stilbene cell was lower than expected, a result that we attribute to inefficient light collection, attenuation of low energy X-rays, solid angle effects, and loss of sample

due to the intermediary gas line. The loss in efficiency affects the MDC of the stilbene cell, causing it to be higher than the plastic scintillator cell, but within MDC limits for radioxenon detectors. Radon interference is slightly decreased using PSD, but this technique could be better applied to nuclear facility monitoring systems.

Chapter 6

Summary, Conclusions, and Future Work

6.1 Summary and Conclusions

This thesis focused on methods to better detect radioxenon for nuclear explosion monitoring. Radioxenon detection is important for the verification regime of the CTBT because, unlike particulate samples that can be trapped in underground explosions, radioxenon escape and travel through the atmosphere. The history of nuclear explosion monitoring and the CTBTO, is discussed in Chapter 1. Chapter 2 describes the decays of the four isotopes of interest and detector mechanisms, provides a literary review of radioxenon detectors, discusses other sources of radioxenon, and presents limitations of the current radioxenon detection systems. Thus, this work aims to help improve radioxenon detection by:

1. Developing and testing the anticoincidence method to improve metastable detection
2. Developing and validating an alternative simulation tool, MCNPX-PoliMi with the Single Decay Option, to help in the development of alternative radioxenon detection systems and production of training spectra, and
3. Developing, manufacturing, and testing a prototype stilbene cell as an alternative for the plastic cells currently used for radioxenon detection.

Chapter 3 gives an overview of the calibration process for radioxenon detectors and the traditional analysis method. A methodology for the anticoincidence method is presented allowing for opti-

mization for the anticoincidence region of interest. The two methods are first compared using a controlled experiment, where it is shown that the anticoincidence method is more sensitive to the metastable isotope, identifying it sooner than the traditional method and having a lower MDA. Next, the two methods are applied to simulation data having various ^{133}Xe interference levels. In this comparison, it is shown that the anticoincidence outperforms the traditional method when the activity of ^{133}Xe is above 150 mBq. The simulation also shows that the anticoincidence method is heavily impacted by the background count rate. Finally, the two methods are compared to radioxenon monitoring station data, where the anticoincidence method outperforms the traditional method by identifying more activity calculations above the MDA. This work shows that the anticoincidence method can help identify metastable isotopes when ^{133}Xe interference is present in a sample. The anticoincidence method is a technique that can be applied to any coincidence system taking both singles and coincidence data and can easily be applied to current radioxenon data sets.

Chapter 4 details the developments of updating MCNPX-PoliMi for use simulating radioxenon decay and detector response. In order to simulate correlated decays, the Single Decay Option of MCNPX-PoliMi is used. The implemented changes for each updated version are presented in this chapter. Validation with experimental data is shown for Versions 2.1.4 an 2.1.6. Major updates to the code, improving agreement between experiment and simulation, include the transport of conversion electrons and updating the branching ratios for each of the isotopes of interest. This simulation tool is advantageous for those that prefer MCNP to Geant4, although it is not possible to transport optical photons. Thus, in order to use this tool, the detector of interest needs to have a relatively good calibration. New detection systems and their spectra can be produced using the MCNPX-PoliMi tool, leading to improved radioxenon detection and analysis.

The major focus of this work was the development of a stilbene cell to replace the plastic cells currently used. Limitations of the plastic cell include energy resolution and memory effect. Chapter 5 presents the development and experimental results of stilbene prototype testing. Preliminary results using solid cylindrical detectors highlight the resolution benefits for replacing plastic with stilbene.

Next, a series of prototypes were manufactured and tested alongside a plastic beta cell detector. The first prototype exhibits different light outputs based on interaction location in the stilbene cell. The second prototype exhibits improved resolution due to the addition of a stilbene endcap; however, the prototype breaks during testing. The third prototype undergoes two measurement campaigns measuring the four radioxenon isotopes of interest as well as ^{127}Xe and radon. Compared to plastic cell, stilbene cell prototype 3 has similar resolution, a lower efficiency resulting in a higher MDC, and an improved memory effect by a factor of 100. The almost negligible memory effect of the stilbene cell can improve the overall sensitivity of the verification regime. A balance between light collection and ruggedness is needed for in-field use of the stilbene cell to obtain maximum performance.

6.2 Future Work

The anticoincidence analysis technique needs to be extended to ^{133m}Xe, which is a more complex analysis because of the daughter product, ^{133}Xe. Additionally, because it can be used with the current radioxenon coincidence detection systems, previous measurements containing medium to high levels of ^{133}Xe interference could be reanalyzed with this method.

Future work for the Single Decay Option includes the implementation of modified beta spectrum tails and low-energy X-ray emissions. These two changes along with careful accounting of variances in detector model and geometry could improve agreement between experiment and simulation, especially the efficiency.

Further improvements to the stilbene cell should include an optimized geometry to maximize light collection and a permanent gas line. Further testing on the polishing of the stilbene cell should be conducted to analyze its effects on energy resolution. Alternative assemblies of the stilbene cell, two versus three pieces, also should be examined to understand impact of light transport. This effect could also be analyzed using Geant4 simulations. In the future, field testing will need to be conducted to examine the long-term performance of the stilbene cell.

6.2.1 Preliminary Geant4 Results

As previously mentioned, optimization of the stilbene cell geometry is needed to maximize in-field performance. Preliminary Geant4 simulations were conducted to compare the prototype-2 and prototype-3 results. As discussed in [141] and [130], Geant4 was used to examine the light collection and detector response using optical photon transport. This simulation requires detector construction, appropriate physics models, source emission and tracking. To construct the detector, the dimensions discussed in Chapter 5 for prototypes 2 and 3 were used, where the epoxy between the surfaces was estimated to be 0.1 mm thick. Figure 6.1 shows the simulation geometries for the two prototypes, where prototype 2 has a ground surface and prototype 3 has a polished surface. To model the scintillation properties of stilbene, the scintillation yield was set to 14,000 photons per MeV, the refractive index was set to 1.64, and the density was set to 1.5 g/cm^3. A mono-energetic electron source, 129-keV, sampled uniformly throughout the volume of the cells was simulated. The optical photons were tracked in the detector material and collected by a simulated photocathode with an average efficiency of 30%. Figure 6.2 shows the fluorescence emission spectrum for stilbene plotted against the photocathode efficiency.

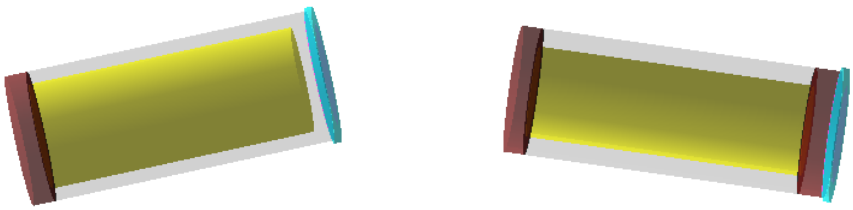

(a) (b)

Figure 6.1: Geant4 simulation geometries for prototypes (a) 2 and (b) 3.

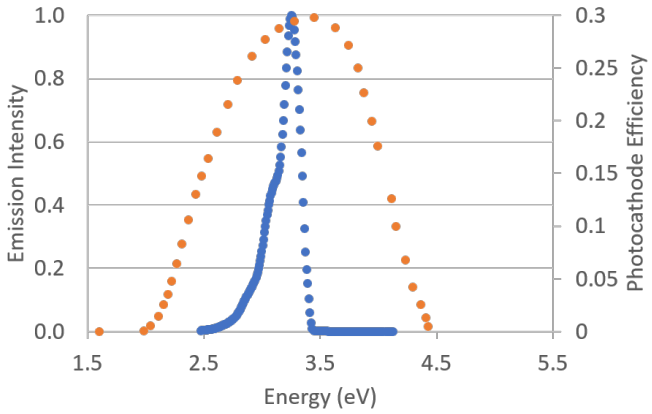

Figure 6.2: Stilbene emission spectrum (blue) and photocathode efficiency (orange), showing that the emission spectrum aligns with the maximum photocathode efficiency.

Figure 6.3 shows the results of the photons detected at the photocathode for prototypes 2 and 3. Prototype 2 has better light collection and prototype 3 has an improved FWHM. However, modifying the dimensions and surface of prototype 3 to match prototype 2, the response for the two prototypes is similar as shown in Figure 6.4.

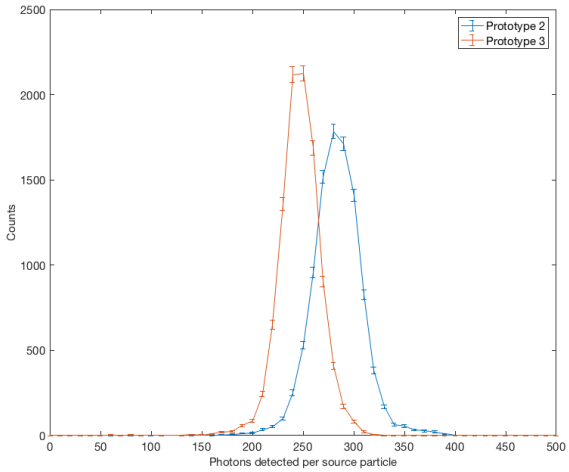

Figure 6.3: Optical photon comparison for prototype 2 (blue) and prototype 3 (orange) using original dimensions, with prototype 2 having a ground surface and prototype 3 having a polished surface. The FWHM is improved for prototype 3; however, the light collection is improved for prototype 2.

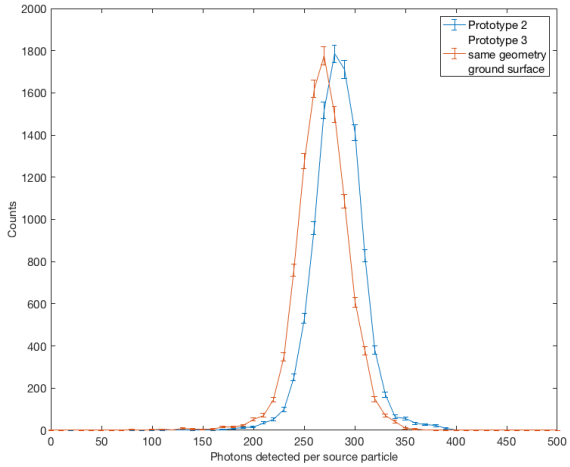

Figure 6.4: Optical photon comparison for prototype 2 (blue) and prototype 3 (orange) using original dimensions, with the prototypes having the same dimensions and ground surface, thus the only difference being one endcap (prototype 2) versus two endcaps (prototype 3). This result shows that the use of multiple endcaps is not the primary contributor to the loss of light collection.

These preliminary results suggest that future simulation work should focus on the surface finish, geometry, and thickness of the cell to optimize light collection. A hybrid geometry containing a solid hemispherical end mated to a hollow cylindrical body should be examined. This geometry is more likely to be manufactured for stilbene over the currently used rounded plastic cell. Additionally, the plastic cell should be simulated for a complete comparison.

Appendix A

Isotopic Ratio Analysis

A.1 Isotopic ratio plots

Previously produced Origen 2.2 data for 3 scenarios was used to create the isotopic ratio plots. The ratios are all with respect to ^{133}Xe. The three scenarios are:

- Boiling water reactor with an irradiation time of 90 days and constant ingrowth
- ^{235}U fission with a separation time of 24 hours
- Medical isotope production facility (MIPF) with an irradiation time of 1 day and constant ingrowth

where the activities were examined over a 30-day period.

Figure A.1 shows a 3-D plot of the ratios of ^{133}Xe with the other isotopes of interest. The ^{135}Xe ratio decreases quickly and the ^{235}U and MIPF ratios are similar.

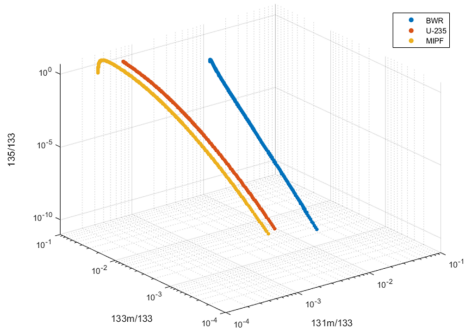

Figure A.1: 3-D ratio plot of ^{133}Xe ratio with the other three isotopes of interest, where the fission and MIPF has similar signatures.

Figure A.2 shows the 2-D plot and 3-D plot including time for the ^{135}Xe and ^{133m}Xe ratios. There is some overlap present for the ^{235}U and MIPF signatures. After approximately 5 days, the ratio is unable to be measured as shown in the 3-D plot.

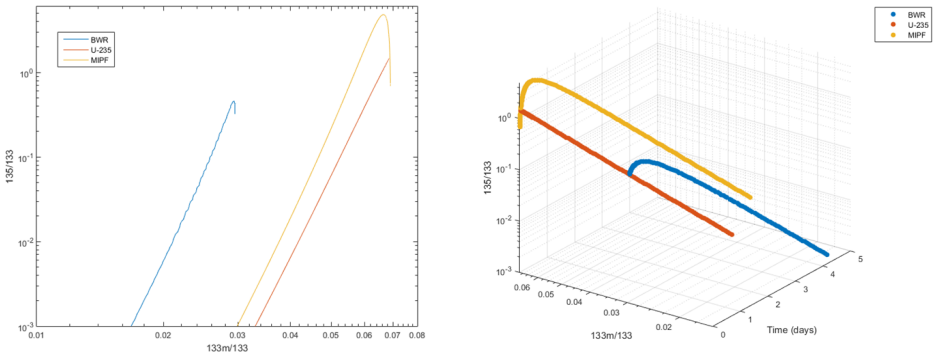

(a) (b)

Figure A.2: Ratio plots for ^{135}Xe and ^{133m}Xe where there is slight overlap for the ^{235}U and MIPF signatures.

Figure A.3 shows the 2-D and 3-D plot including time for the ^{135}Xe and ^{131m}Xe ratios. The signatures from ^{235}U and MIPF are similar but do not overlap. After approximately 7 days the ratio is unable to be measured as shown in the 3-D plot.

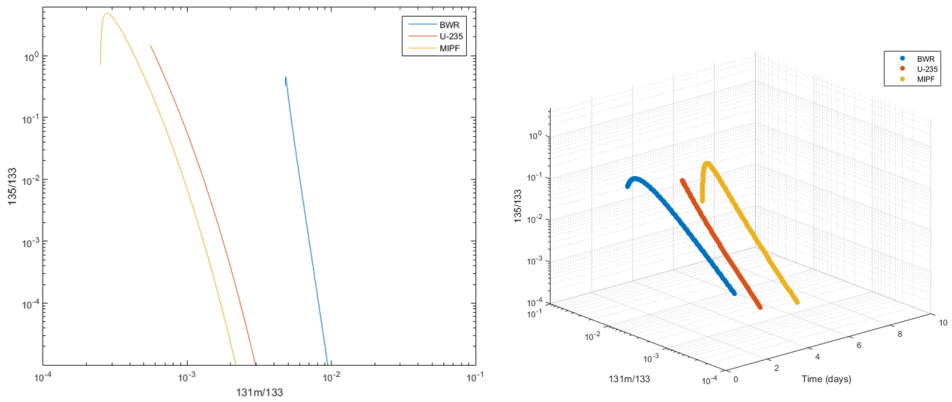

(a) (b)

Figure A.3: Ratio plots for ^{135}Xe and ^{131m}Xe where the ratio is unable to be measured after 7 days.

Figure A.4 shows the 2-D and 3-D plot including time for the ^{133m}Xe and ^{131m}Xe ratios. The three signatures are close to one another but do not overlap. However, this ratio can be difficult to measure if ^{133}Xe is present in the sample causing interference.

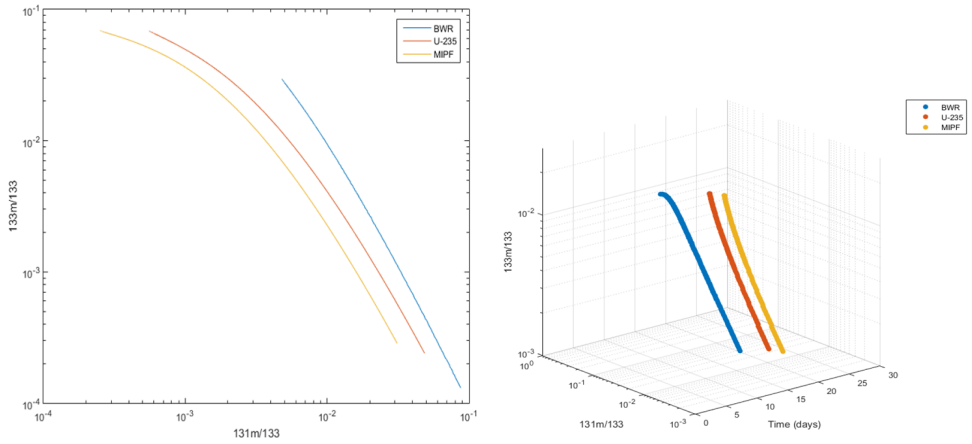

(a) (b)

Figure A.4: Ratio plots for ^{133m}Xe and ^{131m}Xe where there no overlap for the signatures, but due to ^{133}Xe can be difficult to measure experimentally.

Figure A.5 shows each isotope activity plotted against ^{133}Xe activity for the three scenarios. The ^{131m}Xe versus ^{133}Xe shows the best discrimination of ^{235}U from the civilian sources.

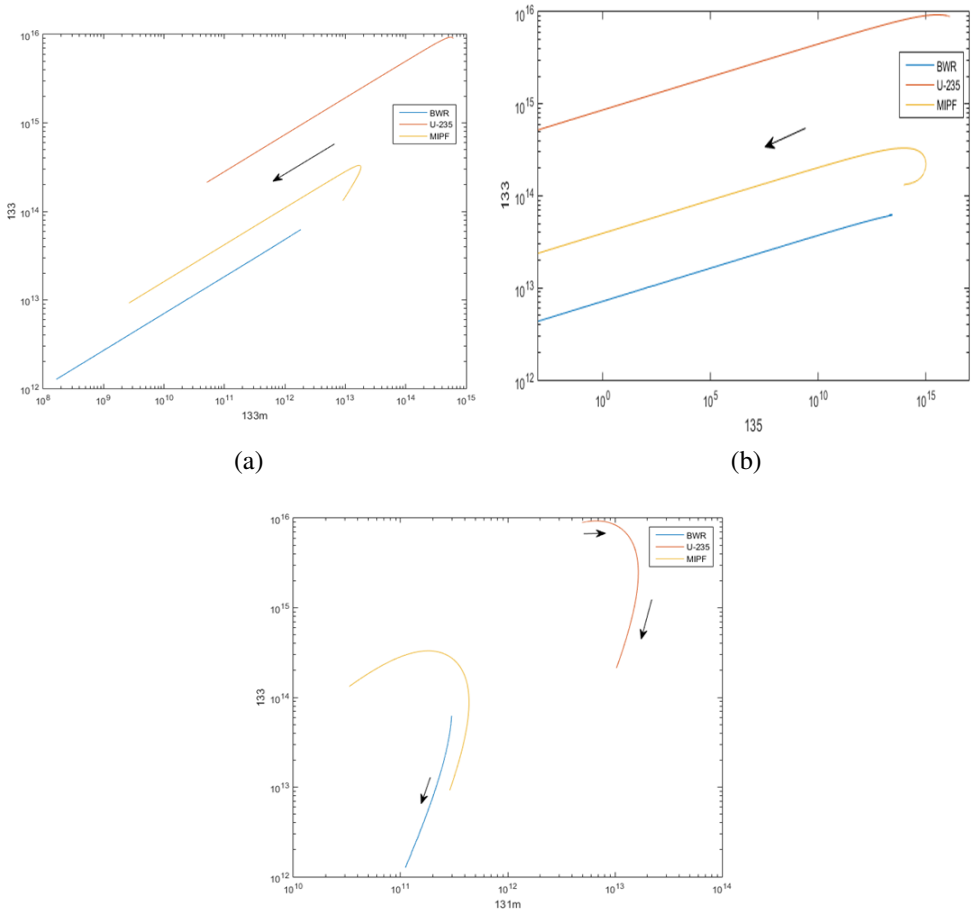

(a) (b)

(c)

Figure A.5: Single isotope activity plots versus ^{133}Xe for each of the isotopes of interest.

A.2 Simulated detector response

Xenon spectrum mixer and BGSim were used to simulate detector response and produce 2-D spectra, where the simulated detectors were calibrated with BGCal. ARAD and CalcMain were used to calculate concentrations. Figure A.6, A.7, and A.8 show the simulated 2-D spectra of the three scenarios after 1 week, 2 weeks, and 1 month of decay respectively. The activity is higher for the ^{235}U scenario with counts being obvious even after a month of decay. For each of the scenarios, ^{133}Xe is easily identified, however, the other isotopes need to be identified in order to use isotopic ratios effectively.

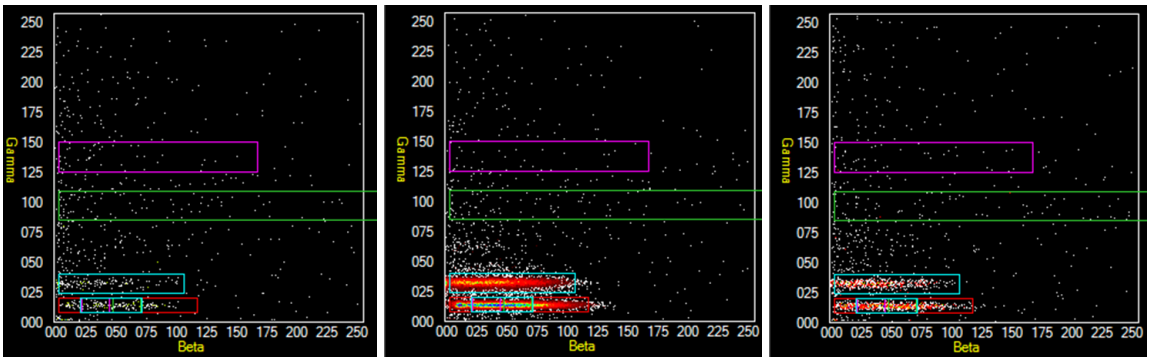

Figure A.6: Simulated 2-D spectra after one week of decay for BWR (left), ^{235}U (middle) and MIPF (right).

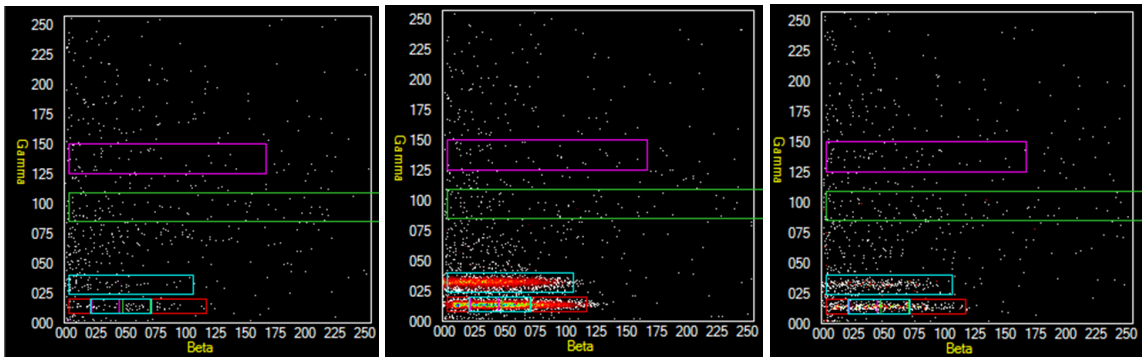

Figure A.7: Simulated 2-D spectra after two weeks of decay for BWR (left), ^{235}U (middle) and MIPF (right).

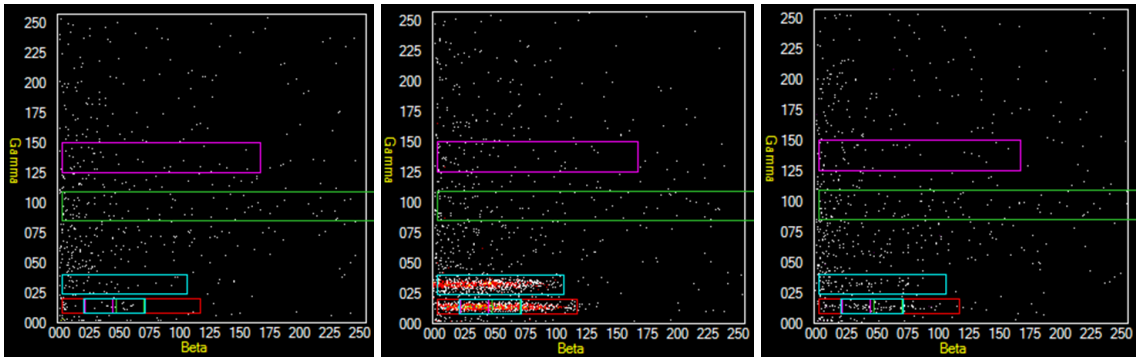

Figure A.8: Simulated 2-D spectra after 1 month of decay for BWR (left), ^{235}U (middle) and MIPF (right).

The calculated ratios using the previously discussed programs were used for the following plots. Since it was shown in the previous section that ^{131m}Xe is able to separate the civilian scenarios from

the fission device, it was the focus of the calculation. Figure A.9 shows the singles isotope plots for ^{131m}Xe versus ^{133}Xe. Comparing Figure A.9b with Figure A.5c we see a similar trend in the order, however there is some overlap in the scenarios which demonstrates the importance of accounting for detector effects. Plotting the ratios versus time, as shown in Figure A.9b, there is separation between the events. However, the MDC had to be used for ^{131m}Xe and thus again demonstrates the limitations of the detector, highlighting the need for improved detector sensitivity especially for the metastable isotopes.

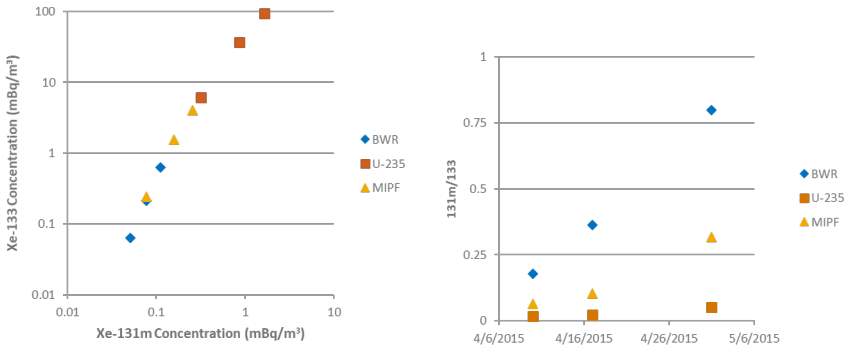

(a) (b)

Figure A.9: Simulated detector response single isotope activity plot of ^{131m}Xe versus ^{133}Xe for the three scenarios.

Appendix B

Data Acquisition and Analysis Scripts

B.1 DPP-PSD firmware coincidence shift register settings

Details about the shift registers can be found in the DPP-PSD manual. Below are the settings for the startup file used with DAFCA.

```
config
cd dig0
#
#mwrite 0x8000 0x4 0x4
##
mwrite 0x1080 0xC0000 0x40000
mwrite 0x1180 0xC0000 0x40000
##
mwrite 0x1070 0xFF 0x5A
mwrite 0x1170 0xFF 0x5A
##
mwrite 0x106C 0xFF 0x9
mwrite 0x116C 0xFF 0x9
##
mwrite 0x8180 0x103 0xFFFFFFFF
mwrite 0x8184 0x103 0xFFFFFFFF
##
mwrite 0x1084 0x60 0xFFFFFFFF
cd ..
acq
exit
```

B.2 PIXIE-4 list mode analysis script with waveforms

```
%read pixie from mode x100
clear all
%fileID = fopen('R:\bgtesting\Xe-133\20160408_133_131m_1dpo40-0005-0x0103.bin');
 datadir = ('F:\2018_FebMarch_pnnlcampaign\xia_data\20180228_cs137_mode100');
 lmfiles = dir([datadir filesep '*.bin']);
 numfiles = length(lmfiles);
E = cell(1e7,4); %cell to store singles energy
P = cell(1e7,4); %cell to store waveforms
```

```
j=1;
k=1;
% x = 0:65535;
% chanloc 1 2 3 4 = pixie ch 3 2 1 0

BUFHEADLEN = 6;
EVENTHEADLEN = 3;
CHANHEADLEN = 9;

 for i=1:numfiles-1
     fileID = fopen([datadir filesep lmfiles(i).name]);
%     E = cell(1e10,4);
%     j=1;
while ~feof(fileID)

BUF_NDATA = fread(fileID,1,'uint16','l');
if isempty(BUF_NDATA)
    break
end

buffer = fread(fileID,BUF_NDATA-1,'uint16','l');
buffer = [BUF_NDATA;buffer];

datastart = BUFHEADLEN+1;

while datastart < length(buffer)

EVT_PATTERN = dec2bin(buffer(datastart),16);
hit_pattern = EVT_PATTERN(end-3:end);

chanloc = strfind(hit_pattern,'1');

%store by number of channels triggered
if length(chanloc) == 1
    CHAN_NDATA = buffer(datastart+EVENTHEADLEN);
    N_WAVE_DATA = CHAN_NDATA - CHANHEADLEN;
    E(j,chanloc(1))= {buffer(datastart+EVENTHEADLEN+2)}; %store energy
    P(k,chanloc(1))= {buffer(datastart+EVENTHEADLEN+CHANHEADLEN:datastart+EVENTHEADLEN+CHANHEADLEN+N_WAVE_DATA-1)};%store waveform
    datastart = datastart+EVENTHEADLEN+CHAN_NDATA;
    j=j+1;
    k=k+1;
elseif length(chanloc) == 2
    CHAN_NDATA = buffer(datastart+EVENTHEADLEN);
    N_WAVE_DATA = CHAN_NDATA - CHANHEADLEN;
    E(j,chanloc(2))= {buffer(datastart+EVENTHEADLEN+2)}; %store energy
    P(k,chanloc(2))= {buffer(datastart+EVENTHEADLEN+CHANHEADLEN:datastart+EVENTHEADLEN+CHANHEADLEN+N_WAVE_DATA-1)};%store waveform
    datastart = datastart+EVENTHEADLEN+CHAN_NDATA;
    CHAN_NDATA = buffer(datastart);
    N_WAVE_DATA = CHAN_NDATA - CHANHEADLEN;
    E(j,chanloc(1))= {buffer(datastart+2)}; %store energy
    P(k,chanloc(1))= {buffer(datastart+CHANHEADLEN:datastart+CHANHEADLEN+N_WAVE_DATA-1)};%store waveform
    datastart = datastart+CHAN_NDATA;
    j=j+1;
    k=k+1;
elseif length(chanloc) == 3
    CHAN_NDATA = buffer(datastart+EVENTHEADLEN);
```

```
    N_WAVE_DATA = CHAN_NDATA - CHANHEADLEN;
    E(j,chanloc(3))= {buffer(datastart+EVENTHEADLEN+2)}; %store energy
    P(k,chanloc(3))= {buffer(datastart+EVENTHEADLEN+CHANHEADLEN:datastart+EVENTHEADLEN+CHANHEADLEN+N_WAVE_DATA-1)};%store waveform
    datastart = datastart+EVENTHEADLEN+CHAN_NDATA;
    CHAN_NDATA = buffer(datastart);
    N_WAVE_DATA = CHAN_NDATA - CHANHEADLEN;
    E(j,chanloc(2))= {buffer(datastart+2)}; %store energy
    P(k,chanloc(2))= {buffer(datastart+CHANHEADLEN:datastart+CHANHEADLEN+N_WAVE_DATA-1)};%store waveform
    datastart = datastart+CHAN_NDATA;
    N_WAVE_DATA = CHAN_NDATA - CHANHEADLEN;
    E(j,chanloc(1))= {buffer(datastart+2)}; %store energy
    P(k,chanloc(1))= {buffer(datastart+CHANHEADLEN:datastart+CHANHEADLEN+N_WAVE_DATA-1)};%store waveform
    datastart = datastart+CHAN_NDATA;
    j=j+1;
    k=k+1;
elseif length(chanloc) == 4
    CHAN_NDATA = buffer(datastart+EVENTHEADLEN);
    N_WAVE_DATA = CHAN_NDATA - CHANHEADLEN;
    E(j,chanloc(4))= {buffer(datastart+EVENTHEADLEN+2)}; %store energy
    P(k,chanloc(4))= {buffer(datastart+EVENTHEADLEN+CHANHEADLEN:datastart+EVENTHEADLEN+CHANHEADLEN+N_WAVE_DATA-1)};%store waveform
    datastart = datastart+EVENTHEADLEN+CHAN_NDATA;
    CHAN_NDATA = buffer(datastart);
    N_WAVE_DATA = CHAN_NDATA - CHANHEADLEN;
    E(j,chanloc(3))= {buffer(datastart+2)}; %store energy
    P(k,chanloc(3))= {buffer(datastart+CHANHEADLEN:datastart+CHANHEADLEN+N_WAVE_DATA-1)};%store waveform
    datastart = datastart+CHAN_NDATA;
    N_WAVE_DATA = CHAN_NDATA - CHANHEADLEN;
    E(j,chanloc(2))= {buffer(datastart+2)}; %store energy
    P(k,chanloc(2))= {buffer(datastart+CHANHEADLEN:datastart+CHANHEADLEN+N_WAVE_DATA-1)};%store waveform
    datastart = datastart+CHAN_NDATA;
    N_WAVE_DATA = CHAN_NDATA - CHANHEADLEN;
    E(j,chanloc(1))= {buffer(datastart+2)}; %store energy
    P(k,chanloc(1))= {buffer(datastart+CHANHEADLEN:datastart+CHANHEADLEN+N_WAVE_DATA-1)};%store waveform
    datastart = datastart+CHAN_NDATA;
    j=j+1;
    k=k+1;
end
end
end
 end
E(j:end,:)=[];
P(k:end,:)=[];
E0 = cell2mat(E(cellfun('isempty',E(:,4))~=1,4));
E1 = cell2mat(E(cellfun('isempty',E(:,3))~=1,3));
E2 = cell2mat(E(cellfun('isempty',E(:,2))~=1,2));
E3 = cell2mat(E(cellfun('isempty',E(:,1))~=1,1));

pcoin = cell2mat(E(cellfun('isempty',E(:,4))~=1&cellfun('isempty',E(:,3))~=1,3:4));
scoin = cell2mat(E(cellfun('isempty',E(:,2))~=1&cellfun('isempty',E(:,1))~=1,1:2));

% P0 = cell2mat(cellfun(@(x) cell2mat(x),{P(:,4)},'un',0));
% P0 = reshape(P0,[N_WAVE_DATA, length(P0)/N_WAVE_DATA]);
P1 = cell2mat(cellfun(@(x) cell2mat(x),{P(:,3)},'un',0));
P1 = reshape(P1,[N_WAVE_DATA, length(P1)/N_WAVE_DATA]);
P1_orig = P1;
P1 = P1 - mean(P1(1:5,:));
```

```
% P2 = cell2mat(cellfun(@(x) cell2mat(x),{P(:,2)},'un',0));
% P2 = reshape(P2,[N_WAVE_DATA, length(P2)/N_WAVE_DATA]);
P3 = cell2mat(cellfun(@(x) cell2mat(x),{P(:,1)},'un',0));
P3 = reshape(P3,[N_WAVE_DATA, length(P3)/N_WAVE_DATA]);
P3_orig = P3;
P3 = P3 - mean(P3(1:5,:));

fclose all;
```

Bibliography

1. CTBTO. [Online]. Available: http://ctbto.org/verification-regime/monitoring-technologies-how-they-work/radionuclide-monitoring/

2. D. Jacobson and C. Ziegler, *Spying without Spies: Origins of America's Secret Nuclear Surveillance System*. PRAEGER FREDERICK A, 1995. [Online]. Available: https://www.ebook.de/de/product/3630266/david_jacobson_charles_a_ziegler_spying_w_o_spies.html

3. A. W. Coven, "Evidence of Increased Radioactivity of the Atmosphere after the Atomic Bomb Test in New Mexico," *Physical Review*, vol. 68, p. 279, Dec. 1945.

4. Arms Control Association, "Nuclear testing and comprehensive test ban treaty (ctbt) timeline." [Online]. Available: https://www.armscontrol.org/factsheets/Nuclear-Testing-and-Comprehensive-Test-Ban-Treaty-CTBT-Timeline

5. Federation of American Scientists, "Comprehensive test ban treaty chronology." [Online]. Available: https://fas.org/nuke/control/ctbt/chron1.htm

6. "Nuclear test ban treaty." [Online]. Available: https://www.jfklibrary.org/JFK/JFK-in-History/Nuclear-Test-Ban-Treaty.aspx

7. History.com Staff, "Nuclear test-ban treaty," 2009. [Online]. Available: https://www.history.com/topics/cold-war/nuclear-test-ban-treaty

8. Limited test ban treaty. [Online]. Available: http://www.state.gov/t/isn/4797.htm

9. "Air force technical applications center." [Online]. Available: https://www.25af.af.mil/about-us/fact-sheets/display/article/333995/air-force-technical-applications-center/

10. "Limited test ban treaty," Federation of American Scientists. [Online]. Available: http://www.fas.org/nuke/control/ltbt/

11. "Treaty of the non-proliferation of nuclear weapons (npt)," Web. [Online]. Available: https://www.un.org/disarmament/wmd/nuclear/npt/

12. Arms Control Association, "Timeline of the nuclear nonproliferation treaty (npt)." [Online]. Available: https://www.armscontrol.org/factsheets/Timeline-of-the-Treaty-on-the-Non-Proliferation-of-Nuclear-Weapons-NPT

13. ——, "The nuclear suppliers group (nsg) at a glance." [Online]. Available: https://www.armscontrol.org/factsheets/NSG

14. "Threshold test ban treaty," Federation of American Scientists. [Online]. Available: http://www.fas.org/nuke/control/ttbt/

15. Federation of American Scientists, "Peaceful nuclear explosions treaty." [Online]. Available: https://fas.org/nuke/control/pnet/intro.htm

16. "Nuclear-weapon-free zones." [Online]. Available: https://www.un.org/disarmament/wmd/nuclear/nwfz/

17. M. B. Kalinowski, "Comprehensive nuclear-test-ban treaty verification," in *Verifying Treaty Compliance*, R. Avenhaus, N. Kyriakopoulos, M. Richard, and G. Stein, Eds. Berlin, Heidelberg: Springer Berlin Heidelberg, 2006, pp. 135–152.

18. Comprehensive nuclear-test-ban treaty. [Online]. Available: https://www.ctbto.org/the-treaty/treaty-text/

19. M. Zahringer, A. Becker, M. Nikkinen, P. Saey, and G. Wotawa, "Ctbt radioxenon monitoring for verification: today's challenges," *J. Radioanal. Nucl. Chem.*, vol. 282, no. 3, p. 737, 2009. [Online]. Available: http://dx.doi.org/10.1007/s10967-009-0207-3

20. S. R. Biegalski, T. Saller, J. Helfand, and K. M. F. Biegalski, "Sensitivity study on modeling radioxenon signals from radiopharmaceutical production facilities," *J. Radioanal. Nucl. Chem.*, vol. 284, no. 3, pp. 663–668, 2010. [Online]. Available: http://dx.doi.org/10.1007/s10967-010-0533-5

21. G. Le Petit, P. Armand, G. Brachet, T. Taffary, J. P. Fontaine, P. Achim, X. Blanchard, J. C. Piwowarczyk, and F. Pointurier, "Contribution to the development of atmospheric radioxenon monitoring," *J. Radioanal. Nucl. Chem.*, vol. 276, no. 2, pp. 391–398, 2008. [Online]. Available: http://dx.doi.org/10.1007/s10967-008-0517-x

22. T. Stocki, P. Armand, P. Heinrich, R. Ungar, R. D'Amours, E. Korpach, A. Bellivier, T. Taffary, A. Malo, M. Bean, I. Hoffman, and M. Jean, "Measurement and modelling of radioxenon plumes in the ottawa valley," *J. Environ. Radioact.*, vol. 99, no. 11, pp. 1775 – 1788, 2008. [Online]. Available: http://www.sciencedirect.com/science/article/pii/S0265931X08001197

23. M. Schoppner, W. Plastino, N. Hermanspahn, E. Hoffmann, M. Kalinowski, B. Orr, and R. Tinker, "Atmospheric transport modelling of time resolved 133xe emissions from the isotope production facility ansto, australia," *J. Environ. Radioact.*, vol. 126, pp. 1 – 7, 2013. [Online]. Available: http://www.sciencedirect.com/science/article/pii/S0265931X13001525

24. P. W. Eslinger, J. I. Friese, J. D. Lowrey, J. I. McIntyre, H. S. Miley, and B. T. Schrom, "Estimates of radioxenon released from southern hemisphere medical isotope production facilities using measured air concentrations and atmospheric transport modeling," *J. Environ. Radioact.*, vol. 135, pp. 94 – 99, 2014. [Online]. Available: http://www.sciencedirect.com/science/article/pii/S0265931X1400112X

25. P. Eslinger, S. Biegalski, T. Bowyer, M. Cooper, D. Haas, J. Hayes, I. Hoffman, E. Korpach, J. Yi, H. Miley, J. Rishel, K. Ungar, B. White, and V. Woods, "Source term estimation of radioxenon released from the fukushima dai-ichi nuclear reactors using measured air concentrations and atmospheric transport modeling," *J. Environ. Radioact.*, vol. 127, pp. 127 – 132, 2014. [Online]. Available: http://www.sciencedirect.com/science/article/pii/S0265931X13002282

26. C. Johnson, J. Lowrey, S. Biegalski, and D. Haas, "Regional transport of radioxenon released from the chalk river laboratories medical isotope facility," *J. Radioanal. Nucl. Chem.*, vol. 305, no. 1, pp. 207–212, 2015. [Online]. Available: http://dx.doi.org/10.1007/s10967-015-4077-6

27. P. W. Eslinger, T. W. Bowyer, I. M. Cameron, J. C. Hayes, and H. S. Miley, "Atmospheric plume progression as a function of time and distance from the release point for radioactive isotopes," *J. Environ. Radioact.*, vol. 148, pp. 123 – 129, 2015. [Online]. Available: http://www.sciencedirect.com/science/article/pii/S0265931X15300357

28. C. Johnson, J. Lowrey, S. Biegalski, and D. Haas, "Examination of local atmospheric transport of radioxenon in the ottawa river valley," *J. Radioanal. Nucl. Chem.*, vol. 307, no. 3, pp. 2155–2159, 2016. [Online]. Available: http://dx.doi.org/10.1007/s10967-015-4488-4

29. P. D. Meutter, J. Camps, A. Delcloo, B. Deconninck, and P. Termonia, "On the capability to model the background and its uncertainty of ctbt-relevant radioxenon isotopes in europe by using ensemble dispersion modeling," *J. Environ. Radioact.*, vol. 164, pp. 280 – 290, 2016. [Online]. Available: http://www.sciencedirect.com/science/article/pii/S0265931X16302715

30. R. Neog, "Ctbt at 20: Why india won't sign the treaty," South Asian Voices, Sep. 2016. [Online]. Available: https://southasianvoices.org/ctbt-at-20-why-india-wont-sign-the-treaty/

31. B. Altaf, "Ctbt at 20: Where india and pakistan stand," South Asian Voices, Sep. 2016. [Online]. Available: https://southasianvoices.org/ctbt-at-20-where-india-and-pakistan-stand/

32. J. Pollac, "North korea, the ctbt, and (maybe?) the end of the nuclear-testing era." [Online]. Available: https://www.armscontrolwonk.com/archive/1205255/north-korea-the-ctbt-and-maybe-the-end-of-the-nuclear-testing-era/

33. P. R. Saey, *Xenon: Radionuclides*. American Cancer Society, 2010. [Online]. Available: https://onlinelibrary.wiley.com/doi/abs/10.1002/0470862106.ia725

34. "Joint evaluated fission and fusion file, incident-neutron data," Oct. 2006. [Online]. Available: http://www-nds.iaea.org/exfor/endf00.htm

35. G. F. Knoll, *Radiation detection and measurement; 4th ed.* New York, NY: Wiley, 2010. [Online]. Available: https://cds.cern.ch/record/1300754

36. W. R. Leo, *Techniques for Nuclear and Particle Physics Experiments*. Springer Berlin Heidelberg, 1994.

37. J. I. McIntyre, B. T. Schrom, M. W. Cooper, A. M. Prinke, T. J. Suckow, A. Ringbom, and G. A. Warren, "A program to generate simulated radioxenon beta–gamma data for concentration verification and validation and training exercises," *J. Radioanal. Nucl. Chem.*, vol. 307, no. 3, pp. 2381–2387, 2016. [Online]. Available: http://dx.doi.org/10.1007/s10967-015-4620-5

38. M. Auer, T. Kumberg, H. Sartorius, B. Wernsperger, and C. Schlosser, "Ten years of development of equipment for measurement of atmospheric radioactive xenon for the verification of the ctbt," *Pure Appl. Geophys.*, vol. 167, no. 4, pp. 471–486, 2010. [Online]. Available: http://dx.doi.org/10.1007/s00024-009-0027-y

39. M. Auer, A. Axelsson, X. Blanchard, T. Bowyer, G. Brachet, I. Bulowski, Y. Dubasov, K. Elmgren, J. Fontaine, W. Harms, J. Hayes, T. Heimbigner, J. McIntyre, M. Panisko, Y. Popov, A. Ringbom, H. Sartorius, S. Schmid, J. Schulze, C. Schlosser, T. Taffary, W. Weiss, and B. Wernsperger, "Intercomparison experiments of systems for the measurement of xenon radionuclides in the atmosphere," *Appl. Radiat. Isot.*, vol. 60, no. 6, pp. 863 – 877, 2004. [Online]. Available: http://www.sciencedirect.com/science/article/pii/S0969804304000417

40. J.-P. Fontaine, F. Pointurier, X. Blanchard, and T. Taffary, "Atmospheric xenon radioactive isotope monitoring," *J Environ Radioact*, vol. 72, no. 1-2, pp. 129 – 135, 2004. [Online]. Available: http://www.sciencedirect.com/science/article/pii/S0265931X03001942

41. T. J. Stocki, M. Bean, R. K. Ungar, H. Toivonen, W. Zhang, J. Whyte, and D. Meyerhof, "Low level noble gas measurements in the field and laboratory in support of the comprehensive nuclear-test-ban treaty," *Appl. Radiat. Isot.*, vol. 61, no. 2-3, pp. 231 – 235, 2004, low Level Radionuclide Measurement Techniques - {ICRM}. [Online]. Available: http://www.sciencedirect.com/science/article/pii/S0969804304001113

42. W. Zhang, K. Ungar, and M. Bean, "Improved radioxenon gamma-spectrometry counting system and its efficiency calibration: Monte carlo simulation and experimental results at enriched xenon counting environment," *J. Radioanal. Nucl. Chem.*, vol. 279, no. 1, pp. 83–91, 2009. [Online]. Available: http://dx.doi.org/10.1007/s10967-007-7299-z

43. F. Xie, X. He, W. Jiang, X. Zhang, Q. Shi, S. Wu, L. Liu, C. Zhang, and L. Chen, "Development of a radioxenon measurement system and its application in monitoring fukushima nuclear accident," *Radiat. Phys. Chem.*, vol. 97, pp. 85 – 89, 2014. [Online]. Available: http://www.sciencedirect.com/science/article/pii/S0969806X13005914

44. R. J. Lagomarsino and N. Latner, "Measurement of low levels of radioactivity with a large well germanium detector," *J. Radioanal. Nucl. Chem.*, vol. 274, no. 1, pp. 39–43, 2007. [Online]. Available: http://dx.doi.org/10.1007/s10967-006-6891-3

45. P. L. Reeder, T. W. Bowyer, and R. W. Perkins, "Beta-gamma counting system for xe fission products," *J. Radioanal. Nucl. Chem.*, vol. 235, no. 1, pp. 89–94, 1998. [Online]. Available: http://dx.doi.org/10.1007/BF02385943

46. J. I. McIntyre, K. H. Abel, T. W. Bowyer, J. C. Hayes, T. R. Heimbigner, M. E. Panisko, P. L. Reeder, and R. C. Thompson, "Measurements of ambient radioxenon levels using the

automated radioxenon sampler/analyzer (arsa)," *J. Radioanal. Nucl. Chem.*, vol. 248, no. 3, pp. 629–635, 2001. [Online]. Available: http://dx.doi.org/10.1023/A:1010672107749

47. A. Ringbom, T. Larson, A. Axelsson, K. Elmgren, and C. Johansson, "Sauna–a system for automatic sampling, processing, and analysis of radioactive xenon," *Nucl. Instrum. Methods Phys. Res., Sect. A*, vol. 508, no. 3, pp. 542 – 553, 2003. [Online]. Available: http://www.sciencedirect.com/science/article/pii/S0168900203016577

48. Y. S. Popov, N. M. Kazarinov, V. Y. Popov, Y. M. Rykov, and N. V. Skirda, "Measuring low activities of fission-product xenon isotopes using the β-γ coincidence method," *Instruments and Experimental Techniques*, vol. 48, no. 3, pp. 380–386, 2005. [Online]. Available: http://dx.doi.org/10.1007/s10786-005-0066-2

49. V. V. Prelovskii, N. M. Kazarinov, A. Y. Donets, V. Y. Popov, I. Y. Popov, and N. V. Skirda, "The arix-03f mobile semiautomatic facility for measuring low concentrations of radioactive xenon isotopes in air and subsoil gas," *Instruments and Experimental Techniques*, vol. 50, no. 3, pp. 393–397, 2007. [Online]. Available: http://dx.doi.org/10.1134/S0020441207030165

50. L. Blackberg, T. Fritioff, L. Martensson, F. Nielsen, A. Ringbom, H. Sjostrand, and M. Klintenberg, "Memory effect, resolution, and efficiency measurements of an al2o3 coated plastic scintillator used for radioxenon detection," *Nucl. Instrum. Methods Phys. Res., Sect. A*, vol. 714, pp. 128 – 135, 2013. [Online]. Available: http://www.sciencedirect.com/science/article/pii/S0168900213002362

51. J. I. McIntyre, A. J. Carman, C. E. Aalseth, J. C. Hayes, T. Heimbigner, T. W. Hossbach, C. W. Hubbard, K. E. Litke, H. S. Miley, S. Morris, M. Ripplinger, and R. Suarez, "Enhanced beta-gamma coincidence counting gas cell," in *Nuclear Science Symposium Conference Record, 2004 IEEE*, vol. 2, Oct 2004, pp. 884–888 Vol. 2.

52. M. W. Cooper, J. I. McIntyre, T. W. Bowyer, A. J. Carman, J. C. Hayes, T. R. Heimbigner, C. W. Hubbard, L. Lidey, K. E. Litke, S. J. Morris, M. D. Ripplinger, R. Suarez, and R. Thompson, "Redesigned β-γ radioxenon detector," *Nucl. Instrum. Methods Phys. Res.*, vol. 579, pp. 426–430, 2007.

53. M. E. Keillor, M. W. Cooper, J. C. Hayes, and J. I. McIntyre, "Degradation of 81Â kev 133xe gamma-rays into the 31Â kev x-ray peak in csi scintillators," *J. Radioanal. Nucl. Chem.*, vol. 282, no. 3, pp. 699–702, 2009. [Online]. Available: http://dx.doi.org/10.1007/s10967-009-0244-y

54. V. Doost-Mohammadi, H. Afarideh, G. Etaati, M. Safari, and H. Rouhi, "Ingas: Iranian noble gas analyzing system for radioxenon measurement," *Radiat. Phys. Chem.*, vol. 120, pp. 26 – 32, 2016. [Online]. Available: http://www.sciencedirect.com/science/article/pii/S0969806X15300827

55. W. Hennig, C. E. Cox, S. J. Asztalos, H. Tan, P. J. Franz, P. M. Grudberg, W. K. Warburton, and A. Huber, "Study of silicon detectors for high resolution radioxenon measurements," *J. Radioanal. Nucl. Chem.*, vol. 296, no. 2, pp. 675–681, May 2013. [Online]. Available: https://doi.org/10.1007/s10967-012-2053-y

56. T. Schroettner, I. Schraick, T. Furch, and P. Kindl, "A high-resolution, multi-parameter, beta-gamma coincidence, mu-gamma anticoincidence system for radioxenon measurement," *Nucl. Instrum. Methods Phys. Res., Sect. A*, vol. 621, no. 1-3, pp. 478 – 488, 2010. [Online]. Available: http://www.sciencedirect.com/science/article/pii/S0168900210014178

57. C. E. Cox, W. Hennig, A. C. Huber, W. K. Warburton, P. M. Grudberg, S. J. Asztalos, H. Tan, and S. Biegalski, "A 24-element silicon pin diode detector for high resolution radioxenon measurements using simultaneous x-ray and electron spectroscopy," in *2013 IEEE Nuclear Science Symposium and Medical Imaging Conference (2013 NSS/MIC)*, Oct 2013, pp. 1–7.

58. G. Le Petit, A. Cagniant, M. Morelle, P. Gross, P. Achim, G. Douysset, T. Taffary, and C. Moulin, "Innovative concept for a major breakthrough in atmospheric radioactive xenon detection for nuclear explosion monitoring," *J. Radioanal. Nucl. Chem.*, vol. 298, no. 2, pp. 1159–1169, Nov 2013. [Online]. Available: https://doi.org/10.1007/s10967-013-2525-8

59. A. Cagniant, G. L. Petit, P. Gross, G. Douysset, H. Richard-Bressand, and J.-P. Fontaine, "Improvements of low-level radioxenon detection sensitivity by a state-of-the art coincidence setup," *Appl. Radiat. Isot.*, vol. 87, pp. 48 – 52, 2014, proceedings of the 19th International Conference on Radionuclide Metrology and its Applications 17-21 June 2013, Antwerp, Belgium. [Online]. Available: http://www.sciencedirect.com/science/article/pii/S0969804313005277

60. G. Le Petit, A. Cagniant, P. Gross, G. Douysset, S. Topin, J. Fontaine, T. Taffary, and C. Moulin, "Spalax new generation: A sensitive and selective noble gas system for nuclear explosion monitoring," *Appl. Radiat. Isot.*, vol. 103, pp. 102 – 114, 2015. [Online]. Available: http://www.sciencedirect.com/science/article/pii/S0969804315300385

61. W. Schell, J. Vives-Batlle, S. Yoon, and M. Tobin, "High-pressure plastic scintillation detector for measuring radiogenic gases in flow systems," *Nucl. Instrum. Methods Phys. Res., Sect. A*, vol. 421, no. 3, pp. 591 – 600, 1999. [Online]. Available: http://www.sciencedirect.com/science/article/pii/S0168900298012170

62. J. Lopes, R. Morgado, and C. Conde, "A metastable xenon isotope detector for treaty verification," *Nucl. Instrum. Methods Phys. Res., Sect. A*, vol. 501, no. 2-3, pp. 623 – 629, 2003. [Online]. Available: http://www.sciencedirect.com/science/article/pii/S0168900203006211

63. J. I. McIntyre, C. E. Aalseth, T. W. Bowyer, J. C. Hayes, T. R. Heimbigner, S. Morris, and P. L. Reeder, "Triple coincidence radioxenon detector," *26th Seismic Research Review - Trends in Nuclear Explosion Monitoring*, vol. LA-UR-04-5801, pp. 581–587, 2004.

64. L. Ranjbar, A. T. Farsoni, and E. M. Becker, "A czt-based radioxenon detection system in support of the comprehensive nuclear-test-ban treaty," *J. Radioanal. Nucl. Chem.*, vol. 310, no. 3, pp. 969–978, Dec 2016. [Online]. Available: https://doi.org/10.1007/s10967-016-4872-8

65. S. A. Czyz and A. T. Farsoni, "A radioxenon detection system using cdznte, an array of sipms, and a plastic scintillator," *J. Radioanal. Nucl. Chem.*, vol. 313, no. 1, pp. 131–140, Jul 2017. [Online]. Available: https://doi.org/10.1007/s10967-017-5287-x

66. J. H. Ely, C. E. Aalseth, and J. I. McIntyre, "Novel beta-gamma coincidence measurements using phoswich detectors," *J. Radioanal. Nucl. Chem.*, vol. 263, no. 1, pp. 245–250, 2005. [Online]. Available: http://dx.doi.org/10.1007/s10967-005-0044-y

67. J. I. McIntyre, B. Schrom, C. E. Aalseth, M. Cooper, J. C. Hayes, T. R. Heimbigner, T. Hossbach, C. Hubbard, K. E. Litke, M. Ripplinger, C. E. Seifert, and R. Suarez, "Beta-gamma coincidence counting using an yttrium aluminum perovskit and bismuth germanate phoswich scintillator," in *IEEE Nuclear Science Symposium Conference Record, 2005*, vol. 3, Oct 2005, pp. 1301–1304.

68. W. Hennig, H. Tan, W. K. Warburton, and J. I. McIntyre, "Single channel beta-gamma coincidence of radioactive xenon using digital pulse shape analysis of phoswich detector signals," in *IEEE Nuclear Science Symposium Conference Record, 2005*, vol. 1, Oct 2005, pp. 510–514.

69. W. Hennig, W. K. Warburton, A. Fallu-Labruyere, K. Sabourov, M. W. Cooper, J. I. McIntyre, A. Gleyzer, M. Bean, E. P. Korpach, K. Ungar, W. Zhang, and P. Mekarski, "Development of a phoswich detector system for radioxenon monitoring," *J. Radioanal. Nucl. Chem.*, vol. 282, no. 3, p. 681, 2009. [Online]. Available: http://dx.doi.org/10.1007/s10967-009-0181-9

70. W. Hennig, W. K. Warburton, A. Fallu-Labruyere, K. Sabourov, M. W. Cooper, J. I. McIntyre, A. Gleyzer, M. Bean, E. P. Korpach, K. Ungar, W. Zhang, P. Mekarski, R. M. Ward, S. R. Biegalski, and D. A. Hass, "Radioxenon measurements with the phoswatch detector system," *Proceedings of the 31st Monitoring Research Review (MRR 2009): Ground-Based Nuclear Explosion Monitorinng Technologies*, vol. LA-UR-09-05276, no. 1, pp. 641–652, Sep. 2009.

71. W. Hennig, S. J. Asztalos, W. K. Warburton, A. Fallu-Labruyere, A. Samie, and P. Mekarski, "Development of a phoswich detector for radioxenon field measurements," vol. 61, no. 5, pp. 2778–2785, Oct 2014.

72. W. Hennig, S. J. Asztalos, W. K. Warburton, and B. D. McNally. (2015) Development of a phoswich detector for radioxenon field measurements. [Online]. Available: https://www.ctbto.org/fileadmin/user_upload/SnT2015/SnT2015_Posters/T3.1-P7.pdf

73. B. de Celis, R. de la Fuente, A. Williart, and B. de Celis Alonso, "Coincidence measurements in alpha beta gamma spectrometry with phoswich detectors using digital pulse shape discrimination analysis," *Nucl. Instrum. Methods Phys. Res., Sect. A*, vol. 580, no. 1, pp. 206 – 209, 2007, proceedings of the 10 th International Symposium on Radiation PhysicsISRP 10. [Online]. Available: http://www.sciencedirect.com/science/article/pii/S0168900207009187

74. A. Farsoni and D. Hamby, "A system for simultaneous beta and gamma spectroscopy," *Nucl. Instrum. Methods Phys. Res., Sect. A*, vol. 578, no. 3, pp. 528 – 536, 2007. [Online]. Available: http://www.sciencedirect.com/science/article/pii/S0168900207012600

75. A. T. Farsoni, B. Alemayehu, A. Alhawsawi, and E. M. Becker, "A phoswich detector with compton suppression capability for radioxenon measurements," vol. 60, no. 1, pp. 456–464, Feb 2013.

76. A. Farsoni, B. Alemayehu, A. Alhawsawi, and E. Becker, "Real-time pulse-shape discrimination and beta-gamma coincidence detection in field-programmable gate array," *Nucl. Instrum. Methods Phys. Res., Sect. A*, vol. 712, pp. 75 – 82, 2013. [Online]. Available: http://www.sciencedirect.com/science/article/pii/S0168900213001733

77. B. Alemayehu, A. T. Farsoni, L. Ranjbar, and E. M. Becker, "A well-type phoswich detector for nuclear explosion monitoring," *J. Radioanal. Nucl. Chem.*, vol. 301, no. 2, pp. 323–332, 2014. [Online]. Available: http://dx.doi.org/10.1007/s10967-014-3182-2

78. T. W. Bowyer, R. Kephart, P. W. Eslinger, J. I. Friese, H. S. Miley, and P. R. Saey, "Maximum reasonable radioxenon releases from medical isotope production facilities and their effect on monitoring nuclear explosions," *J. Environ. Radioact.*, vol. 115, pp. 192 – 200, 2013. [Online]. Available: http://www.sciencedirect.com/science/article/pii/S0265931X12001993

79. T. Bowyer, K. Abel, W. Hensley, M. Panisko, and R. Perkins, "Ambient 133xe levels in the northeast us," *J. Environ. Radioact.*, vol. 37, no. 2, pp. 143 – 153, 1997. [Online]. Available: http://www.sciencedirect.com/science/article/pii/S0265931X97000052

80. T. W. Bowyer, K. H. Abel, C. W. Hubbard, M. E. Panisko, P. L. Reeder, R. C. Thompson, and R. A. Warner, "Field testing of collection and measurement of radioxenon for the comprehensive test ban treaty," *J. Radioanal. Nucl. Chem.*, vol. 240, no. 1, pp. 109–122, 1999. [Online]. Available: http://dx.doi.org/10.1007/BF02349143

81. J. Schulze, M. Auer, and R. Werzi, "Low level radioactivity measurement in support of the CTBTO," *Appl. Radiat. Isot.*, vol. 53, no. 1-2, pp. 23 – 30, 2000. [Online]. Available: http://www.sciencedirect.com/science/article/pii/S0969804300001822

82. M. B. Kalinowski and M. P. Tuma, "Global radioxenon emission inventory based on nuclear power reactor reports," *J. Environ. Radioact.*, vol. 100, no. 1, pp. 58 – 70, 2009. [Online]. Available: http://www.sciencedirect.com/science/article/pii/S0265931X0800180X

83. G. Wotawa, A. Becker, M. Kalinowski, P. Saey, M. Tuma, and M. Zahringer, "Computation and analysis of the global distribution of the radioxenon isotope 133xe based on emissions from nuclear power plants and radioisotope production facilities and its relevance for the verification of the nuclear-test-ban treaty," *Pure Appl. Geophys.*, vol. 167, no. 4, pp. 541–557, 2010. [Online]. Available: http://dx.doi.org/10.1007/s00024-009-0033-0

84. P. R. J. Saey, C. Schlosser, P. Achim, M. Auer, A. Axelsson, A. Becker, X. Blanchard, G. Brachet, L. Cella, L.-E. De Geer, M. B. Kalinowski, G. Le Petit, J. Peterson, V. Popov, Y. Popov, A. Ringbom, H. Sartorius, T. Taffary, and M. Zähringer, "Environmental radioxenon levels in europe: a comprehensive overview," *Pure Appl. Geophys.*, vol. 167, no. 4, pp. 499–515, May 2010. [Online]. Available: http://dx.doi.org/10.1007/s00024-009-0034-z

85. G. Steinhauser, M. Lechermann, A. Axelsson, H. Böck, A. Ringbom, P. R. J. Saey, C. Schlosser, and M. Villa, "Research reactors as sources of atmospheric radioxenon," *J. Radioanal. Nucl. Chem.*, vol. 296, no. 1, pp. 169–174, 2013. [Online]. Available: http://dx.doi.org/10.1007/s10967-012-1949-x

86. P. Tayyebi, F. A. Davani, M. Tabasi, M. Ebrahimkhani, and H. Afarideh, "Computational investigation of isotopic signature of radioxenon released from tehran research reactor," *J. Radioanal. Nucl. Chem.*, vol. 311, no. 1, pp. 571–576, 2017. [Online]. Available: http://dx.doi.org/10.1007/s10967-016-5024-x

87. L. R. Mason, J. D. Bohner, and D. L. Williams, "Airborne anthropogenic radioactivity measurements from an international radionuclide monitoring system," *J. Radioanal. Nucl. Chem.*, vol. 235, no. 1, pp. 71–75, 1998. [Online]. Available: http://dx.doi.org/10.1007/BF02385940

88. T. Bowyer, S. Biegalski, M. Cooper, P. Eslinger, D. Haas, J. Hayes, H. Miley, D. Strom, and V. Woods, "Elevated radioxenon detected remotely following the fukushima nuclear accident," *J. Environ. Radioact.*, vol. 102, no. 7, pp. 681 – 687, 2011. [Online]. Available: http://www.sciencedirect.com/science/article/pii/S0265931X11000816

89. L. Sinclair, H. Seywerd, R. Fortin, J. Carson, P. Saull, M. Coyle, R. V. Brabant, J. Buckle, S. Desjardins, and R. Hall, "Aerial measurement of radioxenon concentration off the west coast of vancouver island following the fukushima reactor accident," *J. Environ. Radioact.*, vol. 102, no. 11, pp. 1018 – 1023, 2011. [Online]. Available: http://www.sciencedirect.com/science/article/pii/S0265931X11001391

90. A. Stohl, P. Seibert, G. Wotawa, D. Arnold, J. F. Burkhart, S. Eckhardt, C. Tapia, A. Vargas, and T. J. Yasunari, "Xenon-133 and caesium-137 releases into the atmosphere from the Fukushima Dai-ichi nuclear power plant: determination of the source term, atmospheric dispersion, and deposition," *Atmos. Chem. Phys.*, vol. 12, no. 5, pp. 2313–2343, 2012. [Online]. Available: http://www.atmos-chem-phys.net/12/2313/2012/

91. A. Stohl, P. Seibert, and G. Wotawa, "The total release of xenon-133 from the fukushima dai-ichi nuclear power plant accident," *J. Environ. Radioact.*, vol. 112, pp. 155 – 159, 2012. [Online]. Available: http://www.sciencedirect.com/science/article/pii/S0265931X12001531

92. I. Hoffman, K. Ungar, M. Bean, J. Yi, R. Servranckx, C. Zaganescu, N. Ek, X. Blanchard, G. Le Petit, G. Brachet, P. Achim, and T. Taffary, "Changes in radioxenon observations in canada and europe during medical isotope production facility shut down in 2008," *J. Radioanal. Nucl. Chem.*, vol. 282, no. 3, p. 767, 2009. [Online]. Available: http://dx.doi.org/10.1007/s10967-009-0235-z

93. P. Saey and L.-E. D. Geer, "Notes on radioxenon measurements for CTBT verification purposes," *Appl. Radiat. Isot.*, vol. 63, no. 5-6, pp. 765 – 773, 2005, 8th International Conference on Applications of Nuclear Techniques8th International Conference on Applications of Nuclear Techniques. [Online]. Available: http://www.sciencedirect.com/science/article/pii/S0969804305001624

94. P. W. Eslinger, I. M. Cameron, J. R. Dumais, Y. Imardjoko, P. Marsoem, J. I. McIntyre, H. S. Miley, U. Stoehlker, S. Widodo, and V. T. Woods, "Source term estimates of radioxenon released from the batek medical isotope production facility using external measured air concentrations," *J. Environ. Radioact.*, vol. 148, pp. 10 – 15, 2015. [Online]. Available: http://www.sciencedirect.com/science/article/pii/S0265931X15300102

95. J. I. McIntyre, A. Agusbudiman, I. M. Cameron, J. R. Dumais, P. W. Eslinger, A. Gheddou, K. Khrustalev, P. Marsoem, H. S. Miley, M. Nikkinen, A. M. Prinke, M. D. Ripplinger, B. T. Schrom, W. A. Sliger, U. Stoehlker, G. Suhariyono, G. A. Warren, S. Widodo, and V. T. Woods, "Real-time stack monitoring at the batek medical isotope production facility," *J. Radioanal. Nucl. Chem.*, vol. 308, no. 1, pp. 311–316, 2016. [Online]. Available: http://dx.doi.org/10.1007/s10967-015-4348-2

96. P. R. Saey, "The influence of radiopharmaceutical isotope production on the global radioxenon background," *J. Environ. Radioact.*, vol. 100, no. 5, pp. 396 – 406, 2009. [Online]. Available: http://www.sciencedirect.com/science/article/pii/S0265931X09000150

97. P. R. Saey, T. W. Bowyer, and A. Ringbom, "Isotopic noble gas signatures released from medical isotope production facilities–simulations and measurements," *Appl. Radiat. Isot.*, vol. 68, no. 9, pp. 1846 – 1854, 2010. [Online]. Available: http://www.sciencedirect.com/science/article/pii/S0969804310001570

98. P. R. Saey, M. Auer, A. Becker, E. Hoffmann, M. Nikkinen, A. Ringbom, R. Tinker, C. Schlosser, and M. Sonck, "The influence on the radioxenon background during the temporary suspension of operations of three major medical isotope production facilities in the northern hemisphere and during the start-up of another facility in the southern hemisphere," *J. Environ. Radioact.*, vol. 101, no. 9, pp. 730 – 738, 2010. [Online]. Available: http://www.sciencedirect.com/science/article/pii/S0265931X10001050

99. T. Bowyer, P. Eslinger, I. Cameron, J. Friese, J. Hayes, L. Metz, and H. Miley, "Potential impact of releases from a new molybdenum-99 production facility on regional measurements of airborne xenon isotopes," *J. Environ. Radioact.*, vol. 129, pp. 43 – 47, 2014. [Online]. Available: http://www.sciencedirect.com/science/article/pii/S0265931X13002828

100. C. G. Doll, C. M. Sorensen, T. W. Bowyer, J. I. Friese, J. C. Hayes, E. Hoffmann, and R. Kephart, "Abatement of xenon and iodine emissions from medical isotope production facilities," *J. Environ. Radioact.*, vol. 130, pp. 33 – 43, 2014. [Online]. Available: http://www.sciencedirect.com/science/article/pii/S0265931X13002890

101. P. W. Eslinger, T. W. Bowyer, P. Achim, T. Chai, B. Deconninck, K. Freeman, S. Generoso, P. Hayes, V. Heidmann, I. Hoffman, Y. Kijima, M. Krysta, A. Malo, C. Maurer, F. Ngan, P. Robins, J. O. Ross, O. Saunier, C. Schlosser, M. Schoeppner, B. T. Schrom, P. Seibert, A. F. Stein, K. Ungar, and J. Yi, "International challenge to predict the impact of radioxenon releases from medical isotope production on a comprehensive nuclear test ban treaty sampling station," *J. Environ. Radioact.*, vol. 157, pp. 41 – 51, 2016. [Online]. Available: http://www.sciencedirect.com/science/article/pii/S0265931X16300510

102. C. Johnson, S. Biegalski, D. Haas, J. Lowrey, T. Bowyer, J. Hayes, R. Suarez, and M. Ripplinger, "Detection in subsurface air of radioxenon released from medical isotope production," *J. Environ. Radioact.*, vol. 167, pp. 160 – 165, 2017. [Online]. Available: http://www.sciencedirect.com/science/article/pii/S0265931X16303204

103. P. R. J. Saey, M. Bean, A. Becker, J. Coyne, R. d'Amours, L.-E. De Geer, R. Hogue, T. J. Stocki, R. K. Ungar, and G. Wotawa, "A long distance measurement of radioxenon in

yellowknife, canada, in late october 2006," *Geophys. Res. Lett.*, vol. 34, no. 20, pp. n/a–n/a, 2007, l20802. [Online]. Available: http://dx.doi.org/10.1029/2007GL030611

104. A. Ringbom, K. Elmgren, K. Lindh, J. Peterson, T. W. Bowyer, J. C. Hayes, J. I. McIntyre, M. Panisko, and R. Williams, "Measurements of radioxenon in ground level air in south korea following the claimed nuclear test in north korea on october 9, 2006," *J. Radioanal. Nucl. Chem.*, vol. 282, no. 3, p. 773, 2009. [Online]. Available: http://dx.doi.org/10.1007/s10967-009-0271-8

105. A. Ringbom, A. Axelsson, M. Aldener, M. Auer, T. Bowyer, T. Fritioff, I. Hoffman, K. Khrustalev, M. Nikkinen, V. Popov, Y. Popov, K. Ungar, and G. Wotawa, "Radioxenon detections in the CTBT international monitoring system likely related to the announced nuclear test in north korea on february 12, 2013," *J. Environ. Radioact.*, vol. 128, pp. 47 – 63, 2014. [Online]. Available: http://www.sciencedirect.com/science/article/pii/S0265931X13002427

106. M. B. Kalinowski, A. Axelsson, M. Bean, X. Blanchard, T. W. Bowyer, G. Brachet, S. Hebel, J. I. McIntyre, J. Peters, C. Pistner, M. Raith, A. Ringbom, P. R. J. Saey, C. Schlosser, T. J. Stocki, T. Taffary, and R. Kurt Ungar, "Discrimination of nuclear explosions against civilian sources based on atmospheric xenon isotopic activity ratios," *Pure Appl. Geophys.*, vol. 167, no. 4, pp. 517–539, May 2010. [Online]. Available: http://dx.doi.org/10.1007/s00024-009-0032-1

107. L. Blackberg, A. Fay, I. Jogi, S. Biegalski, M. Boman, K. Elmgren, T. Fritioff, A. Johansson, L. Martensson, F. Nielsen, A. Ringbom, M. Rooth, H. Sjostrand, and M. Klintenberg, "Investigations of surface coatings to reduce memory effect in plastic scintillator detectors used for radioxenon detection," *Nuclear Instruments & Methods in Physics Research Section A: Accelerators, Spectrometers, Detectors and Associated Equipment*, vol. 656, no. 1, pp. 84 – 91, 2011. [Online]. Available: http://www.sciencedirect.com/science/article/pii/S0168900211014884

108. C. Seifert, J. I. McIntyre, K. C. Antolick, A. J. Carman, M. W. Cooper, J. C. Hayes, T. R. Heimbigner, C. W. Hubbard, K. E. Litke, M. D. Ripplinger, and R. Suarez, "Mitigation of memory effects in beta scintillation cells for radioactive gas detection," *27th Seismic Research Review: Ground-Based Nuclear Explosion Monitoring Technologies*, 2005.

109. K. Khrustalev, J. Wieslander, M. Auer, and A. Gheddou, "Calibration of low-level beta-gamma coincidence detector systems for xenon isotope detection," *Appl. Radiat. Isot.*, vol. 109, pp. 418 – 424, 2016, proceedings of the 20th International Conference on Radionuclide Metrology and its Applications 8-11 June 2015, Vienna, Austria. [Online]. Available: http://www.sciencedirect.com/science/article/pii/S0969804315302608

110. V. E. Guiseppe, S. R. Elliott, A. Hime, K. Rielage, and S. Westerdale, "A radon progeny deposition model." AIP, 2011.

111. P. De Meutter, J. Camps, A. Delcloo, and P. Termonia, "Assessment of the announced north korean nuclear test using long-range atmospheric transport and dispersion modelling," *Scientific Reports*, vol. 7, no. 1, p. 8762, Aug. 2017. [Online]. Available: https://doi.org/10.1038/s41598-017-07113-y

112. M. W. Cooper, J. H. Ely, D. A. Haas, J. C. Hayes, J. I. McIntyre, L. S. Lidey, and B. T. Schrom, "Absolute efficiency calibration of a beta-gamma detector," *IEEE Transactions on Nuclear Science*, vol. 60, no. 2, pp. 676–680, April 2013.

113. J. I. McIntyre, M. Cooper, J. Ely, D. Haas, B. Schrom, and G. Warren, "Further developments of a robust absolute calibration method utilizing beta/gamma coincidence techniques," *J. Radioanal. Nucl. Chem.*, vol. 296, no. 2, pp. 693–698, 2013. [Online]. Available: http://dx.doi.org/10.1007/s10967-012-2112-4

114. A. Axelsson and A. Ringbom, "Xenon air activity concentration analysis from coincidence data," FOI Swedish Defense Research Agency, Tech. Rep. FOI-R–0913–SE, September 2003.

115. J. I. McIntyre, T. W. Bowyer, and P. L. Reeder, "Calculation of minimum detectable concentration levels of radioxenon isotopes using the pnnl arsa system," Pacific Northwest National Laboratory, Tech. Rep. 13102, Mar. 2006. [Online]. Available: http://www.osti.gov/scitech/servlets/purl/888707

116. A. Axelsson, L. Martensson, A. Mortsell, and A. Ringbom, "Improvement of the sauna noble gas system calibration," FOI Swedish Defence Research Agency, Tech. Rep. FOI-R–3451–SE, July 2010.

117. J. Bryant, "Anticoincidence counting method for standardizing radioactive materials," *The International Journal of Applied Radiation and Isotopes*, vol. 13, no. 6, pp. 273 – 276, 1962. [Online]. Available: http://www.sciencedirect.com/science/article/pii/0020708X62901047

118. C. da Silva, E. Rezende, R. Poledna, L. Tauhata, A. Iwahara, and R. Lopes, "Standardization of 106ru/rh by live-timed anticoincidence counting and gamma emission determination," *Appl. Radiat. Isot.*, vol. 122, pp. 37 – 40, 2017. [Online]. Available: http://www.sciencedirect.com/science/article/pii/S0969804317300301

119. R. B. Firestone, C. M. Baglin, and S. Chu, *Table of isotopes*. Wiley, 1999, no. v. 4. [Online]. Available: https://books.google.com/books?id=W4JUAAAAMAAJ

120. L. A. Currie, "Limits for qualitative detection and quantitative determination. Application to radiochemistry," *Anal. Chem.*, vol. 40, no. 3, pp. 586–593, 1968. [Online]. Available: http://dx.doi.org/10.1021/ac60259a007

121. N. Deshmukh, A. Prinke, B. Miller, and J. McIntyre, "Comparison of new and existing algorithms for the analysis of 2d radioxenon beta gamma spectra," *J. Radioanal. Nucl. Chem.*, vol. 311, no. 3, pp. 1849–1857, Mar 2017. [Online]. Available: https://doi.org/10.1007/s10967-017-5174-5

122. D. A. Haas, S. R. Biegalski, and K. M. Foltz Biegalski, "Modeling β-γ coincidence spectra of 131mxe, 133xe, 133mxe, and 135xe," *J. Radioanal. Nucl. Chem.*, vol. 277, no. 3, p. 561, 2008. [Online]. Available: http://dx.doi.org/10.1007/s10967-007-7178-z

123. W. Zhang, P. Mekarski, J. Lam, and K. Ungar, "A geant4 monte carlo method for synthesizing radioxenon beta-gamma coincidence spectra," *J. Radioanal. Nucl. Chem.*, vol. 286, no. 1, pp. 235–240, 2010. [Online]. Available: http://dx.doi.org/10.1007/s10967-010-0645-y

124. V. Doost-Mohammadi, H. Afarideh, and G. R. Etaati, "Simulation of beta–gamma coincidence spectra of radioxenon detector using gate 7.0 and comparison with experimental results," *J. Radioanal. Nucl. Chem.*, vol. 309, no. 3, pp. 1105–1112, 2016. [Online]. Available: http://dx.doi.org/10.1007/s10967-016-4720-x

125. S. A. Pozzi, E. Padovani, and M. Marseguerra, "Mcnp-polimi: a monte-carlo code for correlation measurements," *Nucl. Instrum. Methods Phys. Res., Sect. A*, vol. 513, no. 3, pp. 550 – 558, 2003. [Online]. Available: http://www.sciencedirect.com/science/article/pii/S0168900203023027

126. W. K. Warburton and W. Hennig, "Stilbene research to support a portable b/g scintillation detector with improved radioxenon mdcs," Poster, 2014.

127. S. J. Asztalos, W. Hennig, and W. K. Warburton, "General purpose pulse shape analysis for fast scintillators implemented in digital readout electronics," *Nucl. Instrum. Methods Phys. Res., Sect. A*, vol. 806, pp. 132 – 138, 2016. [Online]. Available: http://www.sciencedirect.com/science/article/pii/S0168900215009572

128. "Inrad optics." [Online]. Available: http://www.inradoptics.com/

129. P. Reeder, T. Bowyer, J. McIntyre, W. Pitts, A. Ringbom, and C. Johansson, "Gain calibration of a beta/gamma coincidence spectrometer for automated radioxenon analysis," *Nucl. Instrum. Methods Phys. Res., Sect. A*, vol. 521, no. 2-3, pp. 586 – 599, 2004. [Online]. Available: http://www.sciencedirect.com/science/article/pii/S0168900203031176

130. C. Sosa, S. Thompson, D. Chichester, S. Clarke, A. D. Fulvio, and S. Pozzi, "Energy resolution experiments of conical organic scintillators and a comparison with geant4 simulations," *Nuclear Instruments and Methods in Physics Research Section A: Accelerators, Spectrometers, Detectors and Associated Equipment*, vol. 898, pp. 77 – 84, 2018. [Online]. Available: http://www.sciencedirect.com/science/article/pii/S0168900218305758

131. A. Cagniant, G. L. Petit, B. Nadalut, P. Gross, H. Richard-Bressand, J.-P. Fontaine, and G. Douysset, "On the use of 127xe standards for the quality control of ctbto noble gas stations and support laboratories," *Appl. Radiat. Isot.*, vol. 89, pp. 176 – 185, 2014. [Online]. Available: http://www.sciencedirect.com/science/article/pii/S0969804314000487

132. F. J. Klingberg, S. R. Biegalski, D. Haas, and A. Prinke, "127xe coincidence decay analysis in support of ctbt verification," *J. Radioanal. Nucl. Chem.*, vol. 305, no. 1, pp. 225–232, Jul 2015. [Online]. Available: https://doi.org/10.1007/s10967-014-3871-x

133. N. Zaitseva, A. Glenn, L. Carman, H. P. Martinez, R. Hatarik, H. Klapper, and S. Payne, "Scintillation properties of solution-grown trans-stilbene single crystals," *Nuclear Instruments and Methods in Physics Research Section A: Accelerators, Spectrometers, Detectors and Associated Equipment*, vol. 789, pp. 8 – 15, 2015. [Online]. Available: http://www.sciencedirect.com/science/article/pii/S0168900215004635

134. M. L. Ruch, M. Flaska, and S. A. Pozzi, "Pulse shape discrimination performance of stilbene coupled to low-noise silicon photomultipliers," *Nuclear Instruments and*

Methods in Physics Research Section A: Accelerators, Spectrometers, Detectors and Associated Equipment, vol. 793, pp. 1 – 5, 2015. [Online]. Available: http://www.sciencedirect.com/science/article/pii/S0168900215005562

135. K. K. Mitev, "Measurement of 222rn by absorption in plastic scintillators and alpha/beta pulse shape discrimination," *Applied Radiation and Isotopes*, vol. 110, pp. 236 – 243, 2016. [Online]. Available: http://www.sciencedirect.com/science/article/pii/S0969804316300240

136. M. Roush, M. Wilson, and W. Hornyak, "Pulse shape discrimination," *Nuclear Instruments and Methods*, vol. 31, no. 1, pp. 112 – 124, 1964. [Online]. Available: http://www.sciencedirect.com/science/article/pii/0029554X64903337

137. S. Pozzi, M. Bourne, and S. Clarke, "Pulse shape discrimination in the plastic scintillator ej-299-33," *Nuclear Instruments and Methods in Physics Research Section A: Accelerators, Spectrometers, Detectors and Associated Equipment*, vol. 723, pp. 19 – 23, 2013. [Online]. Available: http://www.sciencedirect.com/science/article/pii/S016890021300524X

138. E. Pagano, M. Chatterjee, E. De Filippo, P. Russotto, L. Auditore, G. Cardella, E. Geraci, B. Gnoffo, C. Guazzoni, G. Lanzalone, S. De Luca, C. Maiolino, N. Martorana, A. Pagano, M. Papa, T. Parsani, S. Pirrone, G. Politi, F. Porto, L. Quattrocchi, F. Rizzo, A. Trifirò, and M. Trimarchi, "Pulse shape discrimination of plastic scintillator ej 299-33 with radioactive sources," *Nuclear Instruments and Methods in Physics Research Section A: Accelerators, Spectrometers, Detectors and Associated Equipment*, vol. 889, pp. 83 – 88, 2018. [Online]. Available: http://www.sciencedirect.com/science/article/pii/S0168900218301608

139. N. Z. Galunov, O. A. Tarasenko, and V. A. Tarasov, "Determination of the light yield of organic scintillators," *Functional Materials*, vol. 20, no. 3, pp. 304 – 309, 2013.

140. L. Ranjbar, A. T. Farsoni, and E. M. Becker, "135xe measurements with a two-element czt-based radioxenon detector for nuclear explosion monitoring," *J. Environ. Radioact.*, vol. 169-170, pp. 221 – 228, 2017. [Online]. Available: http://www.sciencedirect.com/science/article/pii/S0265931X16302880

141. C. Sosa, "The importance of light collection efficiency in radiation detection systems that use organic scintillators," Ph.D. dissertation, University of Michigan, 2018. [Online]. Available: http://hdl.handle.net/2027.42/145915